Journal of Asia-Pacific Biodiversity 14 (2021) 613–621

Contents lists available at ScienceDirect

Journal of Asia-Pacific Biodiversity

journal homepage: http://www.elsevier.com/locate/japb

Original Article

Little known *Curculigo brevifolia* deserves a species rank: evidences from morphological, cytological and molecular data

Avinash R. Gholave [a,*,†], Asif S. Tamboli [b,†], Rohit N. Mane [c], Ramchandra D. Gore [d], Jae-Hong Pak [b], Sayajirao P. Gaikwad [d]

[a] Department of Botany, K. V. N. Naik Arts, Commerce and Science College, Canada Corner, Nashik, 422002, India
[b] Research Institute for Dok-do and Ulleung-do Island, Department of Biology, School of Life Sciences, Kyungpook National University, 80 Daehak-ro, Buk-gu, Daegu, 41566, Republic of Korea
[c] Department of Botany, Shivaji University, Kolhapur, 416 004, Maharashtra, India
[d] Life Science Research Laboratory, Walchand College of Arts and Science, Solapur, 413 006 Maharashtra, India

ARTICLE INFO

Article history:
Received 11 May 2021
Received in revised form
28 June 2021
Accepted 2 August 2021
Available online 3 September 2021

Keywords:
Cytology
Phylogeny
*rbc*L
Taxonomy
*trn*L-F

ABSTRACT

The *Curculigo brevifolia* resurrected here based on morphological, cytological, and molecular phylogenetic analyses. *Curculigo brevifolia* morphologically resembles *C. orchioides* but differs in having bulbils at the tip of leaves for vegetative reproduction, leaves elongated falcately shaped, beaked fruits. Cytological parameters, karyotype formula, total haploid genome length (THL), values of CV_{CL}, M_{CA} also supported the distinctness of *C. brevifolia* and *C. orchioides*. Phylogenetic analysis based on cpDNA data resulted in the recognition of three clades and strongly supported the revised systematics of Hypoxidaceae. The resurrected species nests within the *Curculigo* clade of Hypoxidaceae and display a close phylogenetic affinity with newly added *Curculigo* species and *C. orchioides*.

Introduction

The family Hypoxidaceae occurs mostly in the Southern Hemisphere and only a few species in the Northern Hemisphere (Kocyan et al. 2011); it contains about 200 species from 11 genera (Kocyan et al. 2011; Liu et al. 2012). Kocyan et al. (2011) reconstructed the phylogenetic relationships of the family using four plastid DNA regions and identified three well-supported major clades: (1) *Curculigo* clade consisting of species of *Curculigo*, *Molineria,* and *Hypoxidia*; (2) *Pauridia* + *Empodium* clade containing species of *Empodium*, *Hypoxis*, *Spiloxene*, *Pauridia,* and *Saniella*; (3) *Hypoxis* clade, including *Hypoxis* and *Rhodohypoxis*. Generic limits in Hypoxidaceae have always been problematic. For example, the genera *Curculigo* and *Molineria* are morphologically very close to each other and difficult to distinguish. Kocyan et al. (2011) reported some diagnostic characters for *Curculigo*, such as the beaked seeds, in which the funicle has an expanded end, and the seed surface ornamentation usually striate. In contrast, the seeds of *Molineria* are not beaked, generally smaller than *Curculigo* seeds, and the surface is striate or not with a subtle tessellate ornamentation.

The genus *Curculigo* includes 19 species and four varieties (Gore and Gaikwad 2018; Govaerts 2016). The first detailed taxonomic treatment of Indian *Curculigo* was published by Baker (1878), who recorded seven species and three varieties from British India. Hooker (1892) recognized five species from British India and grouped them into two sections, namely *Curculigo* sect. *Curculigo* and *C.* sect. *Molineria* (Colla 1826). Karthikeyan et al. (1989) listed seven species of *Curculigo* from India; among those four species is now a member of genus *Molineria*. Further, *Curculigo maharashtrensis* M.R.Almeida & S.Yadav (Almeida and Yadav 2009), *C. savantwadiensis* M.R.Almeida and S.Yadav (Almeida and Yadav 2009), *C. janarthanamii* Gore and S.P.Gaikwad (Gore and Gaikwad 2018) and *C. sabui* S.P.Gaikwad and Gore (Gaikwad et al. 2019) have been recently described from Maharashtra, India. Therefore, the total number of Indian species of *Curculigo* is now six;

The *Curculigo brevifolia* was described by Aiton (1811) based on characters lanceolate leaves and longer flowers. Wight (1853) published *Curculigo malabarica.* Wight (*l.c.*) and treated both

* Corresponding author.
E-mail address: agholave@gmail.com (A.R. Gholave).
Peer review under responsibility of National Science Museum of Korea (NSMK) and Korea National Arboretum (KNA).
† Both authors are equally contributed.

https://doi.org/10.1016/j.japb.2021.08.002
pISSN2287-884X eISSN2287-9544/

Table 1. Species used in molecular analyses with voucher information and Gen Bank accession numbers for all the sequences used in this study.

Species	DNA source/Voucher	*rbc*L/*trn*L-F
Curculigo erecta Lauterb.	cult. BG Leiden 932789	HM459539/HM459485
Curculigo finlaysoniana (Baker) Wall. ex Hook.f.	C.D.K. Cook, E.M. Rix & R.J. Schneller No. 23 (Z/ZT)	HM459540/HM459486
Curculigo orchioides Gaertn.	coll. M.K. Janarthanam, s.n., Goa University Campus (CAL)	HM459541/HM459487
Curculigo orchioides Gaertn.	Avinash & Rohit 610 (SUK)	MK105742[a]/MK105745[a]
Curculigo pilosa ssp. major (Baker) Wiland	R. Ehrich, No. 266 (B)	HM459542/HM459488
Curculigo racemosa Ridl.	cult. BG Leiden 970647	HM459543/HM459489
Curculigo scorzonerifolia (Lam.) Baker	A.R.A. Görts et al. nr. 449 (L ex U)	HM459544/HM459490
Neofriedmannia seychellensis (Bojer ex Baker) Kocyan & Wiland	leg. C. Küffer, s.n., 28. 11. 2002 (BONN)	HM459545/HM459491
Curculigo sinensis S.C.Chen	cult. Kunming Botanical Garden, s.n.	HM459547/HM459493
Curculigo janarthanamii R.D. Gore & S.P. Gaikwad	R.D. Gore & S.P. Gaikwad 13093 (CAL)	MK105741[a]/MK105744[a]
Curculigo sabui S.P.Gaikwad & Gore	R.D. Gore-13097	MW544873[a]/MW544875[a]
Curculigo sp.	RNM-450	MW544874[a]/MW544876[a]
Curculigo brevifolia W.T. Aiton	Avinash & Rohit 600 (SUK)	MK105743[a]/MK105746[a]
Empodium elongatum (Nel) B.L.Burtt	Snijman 1908 (NBG)	HM459553/HM459495
Empodium flexile (Nel) M.F.Thomps. ex Snijman	Snijman 1706 (NBG)	HM459554/HM459494
Empodium plicatum (Thunb.) Garside	cult. BG Munich, s.n. (M)	HM459555/HM459496
Empodium veratrifolium (Willd.) M.F.Thomps	Kocyan AK990309/1/03 (Z/ZT)	HM459556/HM459497
Empodium sp.	Desmet 2979 (NBG)	HM459557/HM459498
Hypoxidia maheensis F. Friedmann	leg. C. Küffer, s.n., 26. 11. 2002	HM459558/HM459499
Hypoxidia rhizophylla (Baker) F. Friedmann	leg. C. Küffer, s.n., 26. 11. 2002	HM459559/HM459500
Hypoxis angustifolia Lam.	cult. Kew Gardens 1973–2957	HM459560/HM459501
Hypoxis aurea Lour.	Kocyan AK426 (M)	HM459562/HM459503
Hypoxis curtissii Rose	Abbott 20321 (FLAS)/MW Chase 108 (NCU)	KJ773578/HM459504
Hypoxis decumbens L.	cult. Kew Gardens 1976–6038	HM459563/HM459505
Hypoxis filiformis Baker	cult. BG Basel; Kocyan AK438 (Z/ZT)	HM459561/HM459502
Pauridia glabella (R.Br.) Snijman & Kocyan	MW Chase 2235 (K)	Y14989/HM459506
Hypoxis hemerocallidea Fisch., C.A.Mey. & Avé-Lall.	cult. BG Berlin, 635807 (B)	HM459564/HM459507
Hypoxis hirsuta (L.) Coville	J.K. Wipf 2209 (M)	HM459565/HM459508
Hypoxis hygrometrica Labill	cult. BG Berlin, 43336 (B)	HM459566/HM459509
Hypoxis juncea Sm.	Whitten s.n. (K)	HM459567/HM459510
Pauridia occidentalis (Benth.) Snijman & Kocyan	s.n. (UWA); Kew DNA number 2234B	HM459568/HM459511
Hypoxis parvula Baker	Singh 556 (NH)	HM639281/HM570029
Hypoxis setosa Baker	29,156 (ZSS)	HM459569/HM459512
Hypoxis villosa L.f.	cult. Kew Gardens 1972–3947	HM459570/HM459513
Hypoxis sp.	cult. BG Bonn; T. Leyens & W. Lobin 126 (BONN)	HM459571/HM459514
Molineria capitulata (Lour.) Herb.	CPG14957/Kocyan AK981228/1/01 (Z)	KX527184/HM459515
Molineria crassifolia Baker	cult. Kunming Botanical Garden, s.n	HM459548/HM459516
Molineria latifolia (Dryand. Ex W.T.Aiton) Herb. ex Kurz	Kocyan AK981023/1/03 (Z/ZT)	HM459550/HM459517
Molineria latifolia (Dryand. ex W.T.Aiton) Herb. ex Kurz	Kocyan AK981019/1/01 (Z/ZT)	HM459549/HM459518
Pauridia longituba M.F.Thomps.	Kocyan AK980624/1/01 (Z/ZT)	HM459572/HM459521
Pauridia minuta (L.f.) T.Durand & Schinz	Snijman 1812 (NBG)	HM639282/HM570030
Rhodohypoxis baurii (Baker) Nel	cult. BG Basel, A. Kocyan AK990522/1/02 (Z/ZT)	HM459573/HM459523
Sinocurculigo taishanic Z.J.Liu,L.J. Chen & Ke Wei Liu	Z. J. Liu 5829 (NOCC)	JQ315819/JQ315820
Pauridia alticola Snijman & Kocyan	Snijman 2059 (NBG)	HM639284/HM639301
Pauridia verna (Hilliard & B.L.Burtt) Snijman & Kocyan	cult. BG Edinburgh 1997–3202	HM459574/HM459524
Pauridia alba (Thunb.) Snijman & Kocyan	Snijman 2106 (NBG)	HM459575/HM459525
Pauridia aquatica (L.f.) Snijman & Kocyan	Snijman 2113 (NBG)	HM639285/HM639302
Pauridia capensis (L.) Snijman & Kocyan	UCI Arb. 728	HM459576/HM459526
Pauridia flaccida (Nel) Snijman & Kocyan	Goldblatt & Manning 9585 (MO, NBG)	HM459577/HM459527
Pauridia gracilipes (Schltr.) Snijman & Kocyan	Snijman 1753 (NBG)	HM639286/HM570032
Pauridia linearis (Andrews) Snijman & Kocyan	Snijman 1754 (NBG	HM639287/HM639303
Pauridia pygmaea Snijman & Kocyan	E. Parker 452 (NBG)	HM639288/HM570033
Pauridia monophylla (Schltr. ex Baker) Snijman & Kocyan	J.C. Paterson-Jones 913 (NBG)	HM459578/HM459528
Pauridia nana (Snijman) Snijman & Kocyan	Snijman 1865a (NBG)	HM639289/HM570034
Pauridia pusilla (Snijman) Snijman & Kocyan	Snijman 1860 (NBG)	HM639290/-
Pauridia affinis (Schult. & Schult.f.) Snijman & Kocyan	E. Parker 469 (NBG)	HM639291/-
Pauridia scullyi (Baker) Snijman & Kocyan	Harrower 3271 (NBG)	HM459579/HM459529
Pauridia trifurcillata (Nel) Snijman & Kocyan	McMaster s.n. (NBG 208,084)	HM570028/HM639304
Outgroup		
Astelia alpina R.Br.	A. Kocyan AK981010/1/01 (Z)	HM459580/HM459530
Astelia banksii A.Cunn.	MW Chase 1072 (K)	Y14983/HM459531
Milligania stylosa (F.Muell. ex Hook.f.) F.Muell. ex Benth.	A. Kocyan 981011/3/01 (Z)	Z73693/HM459533
Blandfordia nobilis Sm.	MW Chase 2835 (K)	Y14984/HM459534
Blandfordia punicea Sweet	AK981013/1/01 (Z/ZT)	Z73694/HM459535
Lanaria lanata (L.) T. Durand & Schinz	E.R. Orchard 342 (M)	HM459581/HM459536

[a] Sequences generated in this study.

species as distinct. Gamble and Fischer (1956) subsumed *C. brevifolia* and *C.malabarica* under the *C. orchioides.* We studied the specimens of *C. orchioides* and *C. brevifolia* from various localities of Maharashtra. It is evident from our studies that the status of *Curculigo brevifolia* needs to be evaluated by using morphological, cytological, and molecular evidences. The cytological and molecular evidence plays an important role in making taxonomic decisions (Stace 2000). Recently with support of molecular evidences,

Chandore et al. (2021) described a new species *Pogostemon jaitapurensis*. We have analyzed the phylogenetic placement of the *Curculigo brevifolia* within Hypoxidaceae based on chloroplast DNA data. Evidences from morphology and karyology have also been gathered. In addition to this, we have shown the phylogenetic placement of recently described new species of *Curculigo*, namely *C. janarthanamii* and *C. sabui*. This study also provides the taxonomic key for Indian *Curculigo* species and distribution map.

Material and methods

Morphological study

Specimens of *Curculigo* were collected during a field tour in the Kolhapur district of Maharashtra state in July 2018, and ten specimens of *C. brevifolia* and *C. orchioides* were grown in pots for further detailed morphological studies. The voucher specimens (A.R. Gholave, R. N. Mane, and S.P. Gaikwad 600) are deposited in SUK. Herbarium specimens of the *Curculigo* from important Indian herbaria like BLAT, CAL, BSI and foreign virtual herbaria, BM, BR, and K (acronyms following Thiers 2020) were examined critically. We consulted the relevant literature (Almeida and Yadav 2009; Baker 1878; Gamble and Fischer 1956; Gore and Gaikwad 2018; Hooker 1892; Karthikeyan et al. 1989) and analyzed the protologues and types.

Cytological study

Plants were kept in fresh water for up to 4–5 days, and root tips from young roots sprouting from the rhizomes were used. Root tips 6–10 mm long were obtained from ten individuals and pretreated with a saturated solution of paradichlorobenzene at 8–10°C for 3–4 h. The root tips were quashed in 2% propionic orcein. Ten well-spread somatic chromosome plates of five different individuals were used for karyotypic analysis. Chromosomes were later photographed with a Carl Zeiss Axio Imager. Types of chromosomes were assigned by using centromeric index following Levan et al. (1964), and karyotype formula was determined using the classes of Stebbins (1971); arms' length for each chromosome, the mean chromosome length (MCL), and the total haploid length (THL) of each karyotype were measured; karyotype asymmetry was evaluated using CVCL and MCA indices (Peruzzi and Eroglu 2013).

DNA extraction, PCR amplification, and Sequencing

Total genomic DNA was extracted from young and fresh leaves of *C. brevifolia,* as well as *C. janarthanamii*, *C. orchioides, C. sabui*, and *Curculigo* species using a modified CTAB method (Paterson et al. 1993) with some modifications described in Tamboli et al. (2021).

The chloroplast DNA regions (*rbc*L and *trn*L-F) were amplified and sequenced. Primers used for amplification and sequencing of *rbc*L were *rbc*La-F (Levin et al. 2003; modified from Soltis et al. 1992) and *rbc*La-R (Kress 2009; modified from Fofana et al. 1997), and those of *trn*L-F were *trn*L-c and *trn*F-f (Taberlet et al. 1991). The polymerase chain reaction (PCR) for these two markers were performed in 25 μL volume containing 12.5 μL AmpliTaq Gold® 360 Master mix (Applied Biosystem, USA), 8.5 μL Nuclease free water, 0.5 μL GC enhancer (Applied Biosystem, USA), 0.5 μL each forward and reverse primer (15 μM/μL). PCR protocol was set to amplify *rbc*L and *trn*L-F marker as: 94°C for 4 min, 35 cycles (94°C for 30 s, 55°C for 1 min and 72°C for 1 min), and final extension was carried out at 72°C for 10 min. PCR reactions were carried out in a Thermal cycler (BIO-RAD, USA). PCR products were checked on 1% agarose gel to confirm the amplification. Amplified PCR products were purified using the GenElute™ PCR Clean-up kit (SIGMA-ALDRICH, USA). Purified PCR products were sequenced bidirectionally using BigDye® Terminator v 3.1 cycle sequencing kit (Applied Biosystems®) on 3500 Genetic Analyzer (Applied Biosystems, USA). Sequences generated in this study were submitted to the GenBank NCBI database. Accession numbers of sequences generated in this study and retrieved from the NCBI GenBank database were provided in Table 1. DNA sequences from 64 taxa describing all genera included in family Hypoxidaceae and outgroup species were used for phylogenetic analyses.

Data analysis and phylogeny

DNA Sequences were checked and edited by using Sequencher v 5.1 (Gene Codes Corporation 2012). Multiple sequence alignment was carried out using MUSCLE (Edgar 2004) implemented in MEGA 7 (Kumar et al. 2016). Alignments of each region were then further refined using GBlocks v. 0.91b (Talavera and Castresana 2007). The *rbc*L and *trn*L-F sequence datasets were concatenated into a single matrix (Supplementary material 1) using BioEdit v. 7.2.6 (Hall 1999). The possible incongruence between *rbc*L and *trn*L-F datasets was tested by using incongruence length test (ILD) (Farris et al. 1994) in PAUP 4.0a152 (Swofford 2002) with 100 homogeneity replicates, random taxon addition (holding 10 trees at each step), tree-bisection-swapping (TBR) searches, MulTrees option in effect with MaxTree set to 100.

Phylogenetic analyses were carried out using two methods: Maximum Likelihood (ML), and Bayesian Inference (BI) to reconstruct the phylogeny of Hypoxidaceae and to determine the phylogenetic positions of the sampled *Curculigo* species. Maximum likelihood analysis (ML) was performed using RaxML-HPC v.8.0 on XSEDE (Stamatakis 2014) via CIPRES portal (Miller et al. 2010) with GTR+G model. Bootstrap support values were obtained with the rapid bootstrap algorithm with 1000 bootstrap replicates. Bayesian inference implementing Markov Chain Monte Carlo (MCMC) was conducted using MrBayes v.3.2.7a on XSEDE (Ronquist et al. 2012). For Bayesian phylogenetic analysis, the best fitting model of nucleotide substitution for *rbc*L + *trn*L-F dataset was selected under the Akaike Information Criterion (AIC) using jModelTest 2 (Darriba et al. 2012) on XSEDE on the CIPRES science gateway (Miller et al. 2010). The best nucleotide substitution found was TIM1+I+G, which is not implemented in the MrBayes program, so we used the first best AIC fitting model available in MrBayes, which was GTR+I+G. Each MCMC analysis was run for 10,000,000 generations, sampling every 1000 generations. The convergence occurred when the standard deviation (SD) of split frequencies fell below 0.01. The first 25% of MCMC generations were discarded as burn-in. Posterior probability values were used to estimate branch support.

Results

Resurrection of C. brevifolia

The specimens collected as *Curculigo orchioides* were not matching with the present circumscription of the *C. orchioides*.

Table 2. Diagnostic features and comparative morphology of *Curculigo orchioides* and *C. brevifolia*.

Characters	*C. orchioides*	*C. brevifolia*
Rhizome	8–9 cm × 5–6 mm thick	5–6 cm ×3–4 mm
Leaves	short and elliptic; 9 × 2.5–3 cm	elongated, falcate, 25 ×1–2 cm
Bulbils	Absent	Present at the tip of leaves
Tepals	Ovate-lanceolate	Linear-lanceolate
Fruits	Without beaked	Beaked
Seeds	Subglobose with short knob	Ovate with long knob

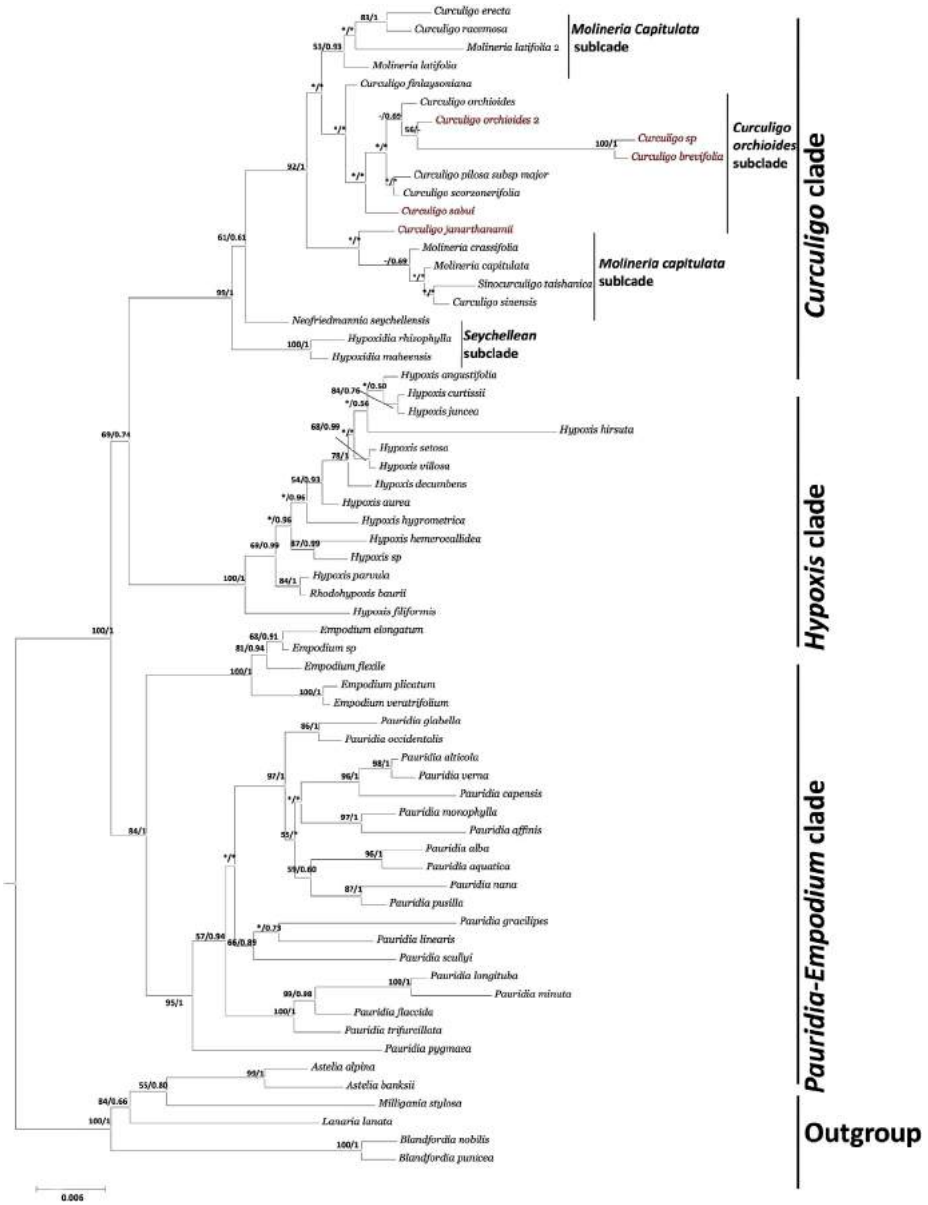

Figure 1. Bayesian phylogenetic tree based on the combined *rbc*L+*trn*L-F dataset. Maximum likelihood bootstrap values and Bayesian posterior probability values (ML/PP) are provided above branches. Asterisk (*) indicates ML BS values < 50% and BPP values < 0.5. The species sampled in this study are highlighted in red color. Names of subclades within *Curculigo* clade were given as mentioned in Kocyan and Wiland-Szymańska (2016).

Bulbils were found to be developed at the tip of leaves. Therefore, it was supposed to be a new species. However, after thorough literature survey, we found that similar species *viz*. *Curculigo brevifolia* was already described by Aiton (1811). However, Gamble and Fischer (1956) merged this species under the *C. orchioides*. After Gamble (*l.c.*), the species was always treated conspecific to *C. orchioides* by several workers viz., Cooke (1908), Matthew (1982) and Nayar et al. (2014). The morphological differences were studied and given in Table 2. These differences show that *C. brevifolia* differs from *C. orchioides* in several aspects and needs to be resurrected.

Phylogenetic analysis

The alignment of *rbc*L + *trn*L-F dataset of 64 taxa was 1821 bp long. Conserved sites, variable sites, and parsimony-informative sites for the combined data set were 1502, 319, and 182, respectively. The incongruence length difference test (ILD) did not reveal a significant heterogeneity between the two regions (*P*-value >0.05), so that all subsequent analyses were performed on the combined dataset. The tree with the highest log-likelihood value of −5905.0493 is shown in Figure S2 (Supplementary material 2). Bayesian phylogenetic analysis is presented in Figure 1 and returned three well supported clades: (1) *Curculigo* clade with ML BS = 99 and PP = 1, which included *Curculigo*, *Molineria*, *Sinocurculigo*, *Neofriedmannia*, and *Hypoxidia*; (2) *Hypoxis* clade with ML BS = 100 and PP = 1, which included *Hypoxis* and *Rhodohypoxis*; (3) *Pauridia-Empodium* clade with ML BS = 84 and PP = 1, which included *Pauridia* and *Empodium*. *Curculigo* clade further divided into three weakly supported subclades (ML BS < 50% and PP < 0.5, respectively), namely, *Molineria capitulata* subclade, *Curculigo orchioides* subclade, and *Seychellean* subclade. The resurrected

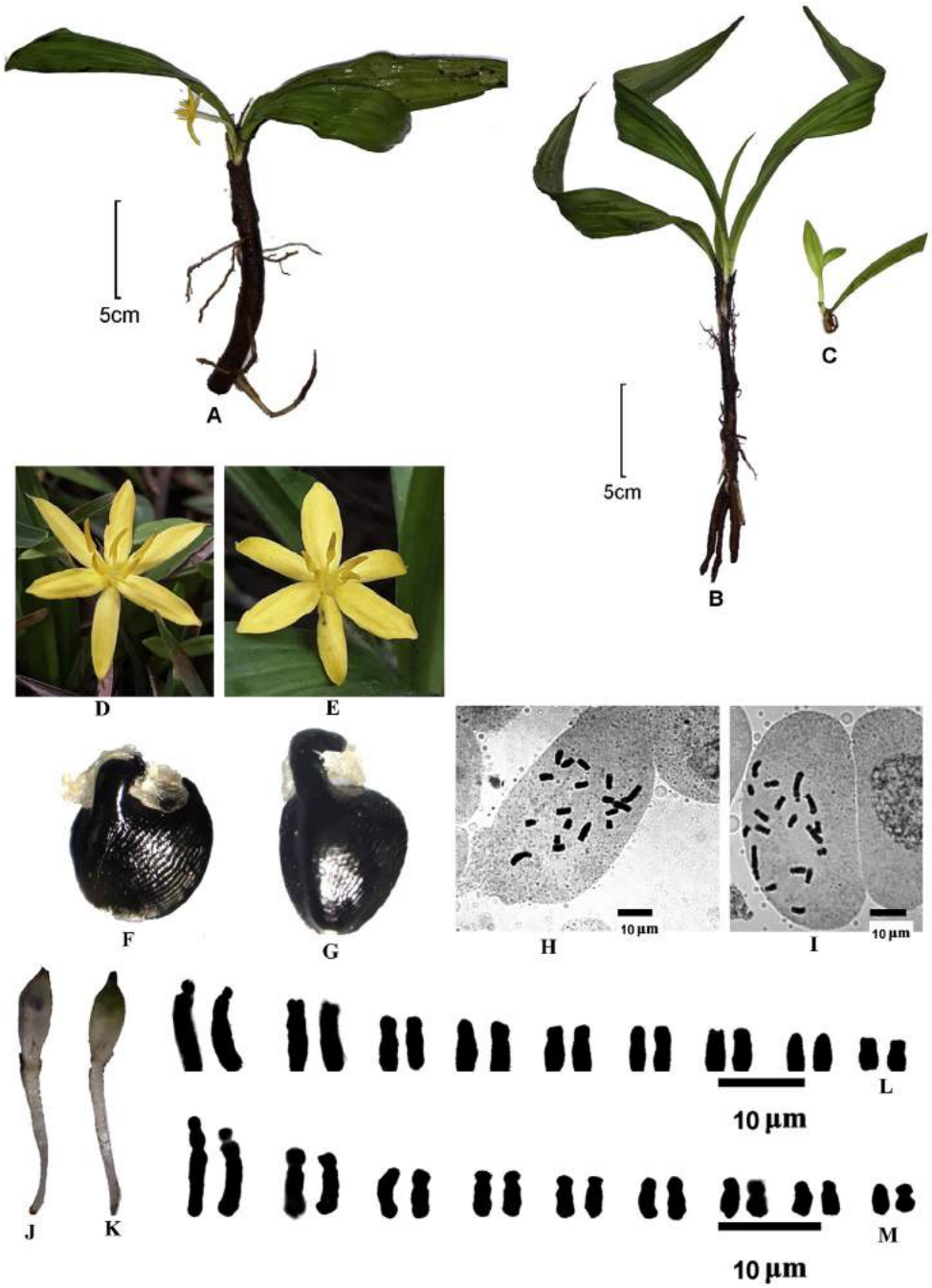

Figure 2. Comparative account of *Curculigo orchioides* and *C. brevifolia*: A, Habit of *C. orchioides*; B, Habit of *C. brevifolia*; C, Vegetative bulbils of *C. brevifolia*; D, Male Flower of *C. orchioides*; E, Male flower of *C. brevifolia*; F, Seed of *C. orchioides*; G, Seed of *C. brevifolia*; H, Metaphase of *C. orchioides*; I, Metaphase of *C. brevifolia*; J, Capsule of *C. orchioides*; K, Capsule of *C. brevifolia*; L, Karyogram of *C. orchioides*; M, Karyogram of *C. brevifolia*.

species *C. brevifolia* was nested in *Curculigo orchioides* subclade and grouped with newly added *Curculigo* species with ML BS = 100 and PP = 1 (Figure 1).

Cytological analysis

Curculigo brevifolia showed a chromosome number of $2n = 18$ (Figure 2I). The shortest chromosome pair measured to be 1.27 µm, and the longest pair was 7.69 µm. Total haploid genome length (THL) was 51.26 µm while mean chromosome length (MCL) was 5.70 µm. The karyotype formula was observed $2n = 18 = 1st + 8sm$ chromosome pairs, which are categorized into 2B asymmetric category of Stebbins. *Curculigo orchioides* showed a chromosome number of $2n = 18$ (Figure 2H). The shortest chromosome pair measured 1.17 µm, and the longest pair was 7.14 µm. Total haploid

Table 3. Comparative karyotype asymmetry features of *Curculigo orchioides* and *C. brevifolia.*

Taxon	*2n*	THL	CV_{CL}	M_{CA}	Karyotype formula
C. orchioides	18	48.90	35.32	33.30	9sm
C. brevifolia	18	51.26	35.91	36.86	1st + 8sm

genome length (THL) was 48.90 μm while mean chromosome length (MCL) was 5.43 μm. The karyotype formula was observed $2n = 18 = 9$ sm chromosomes pairs and fell into the 2B asymmetric category of Stebbins. The asymmetric indices CV_{CL} and $M_{CA}$are reported in Table 3.

Taxonomic accounts

Curculigo brevifolia W.T. Aiton (1811: 253) (Figures 2 and 3)

The resurrected species *Curculigo brevifolia* morphologically resembles *Curculigo orchioides*, but differs by having 5–6 cm × 3–4 mm rhizomes (vs. 8–9 cm × 5–6 mm in *C. orchioides*); elongated and falcate leaves (vs. leaves short and elliptic), 25 × 1–2 cm (vs. 9 × 2.5–3 cm leaves), bulbils present at the tip of the leaves (vs. bulbils absent); ovate-lanceolate tepals (vs. linear-lanceolate tepals); beaked fruits (vs. nonbeaked fruits), ovate seeds with long knob (vs. subglobose seeds with short knob).

Material examined. India, Maharashtra, Kolhapur district: Kolhapur – Ratnagiri road, Warul, 16°94'82"N; 73°87'55"E, ± 597m, 29 vii 2018, A. R. Gholave, R. N. Mane and S. P. Gaikwad 600.

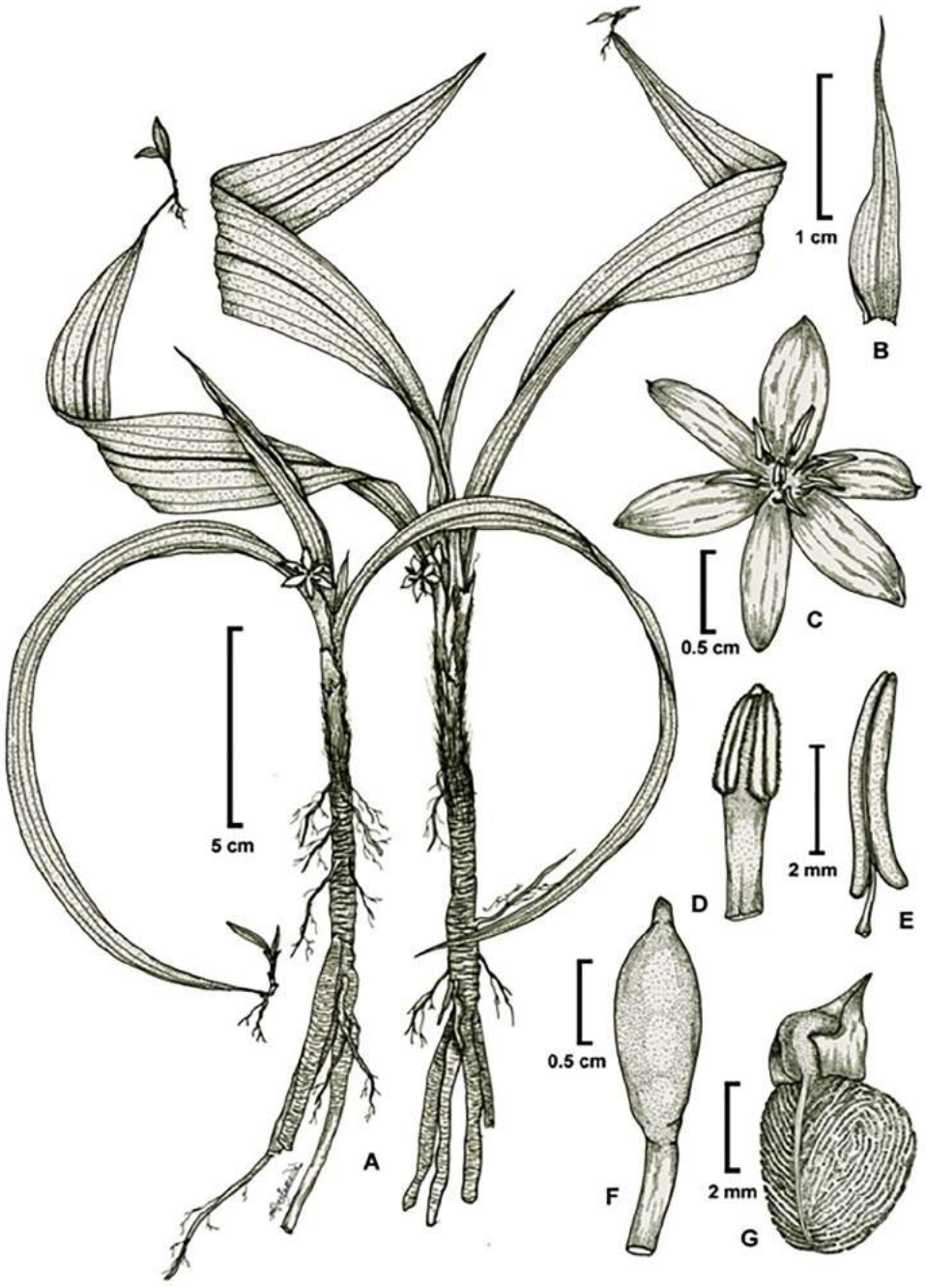

Figure 3. *Curculigo brevifolia*: A, Habit; B, Bract; C, Bisexual flower; D, Stigma; E, Stamen; F, Capsule with perigone tube; G, Seed.

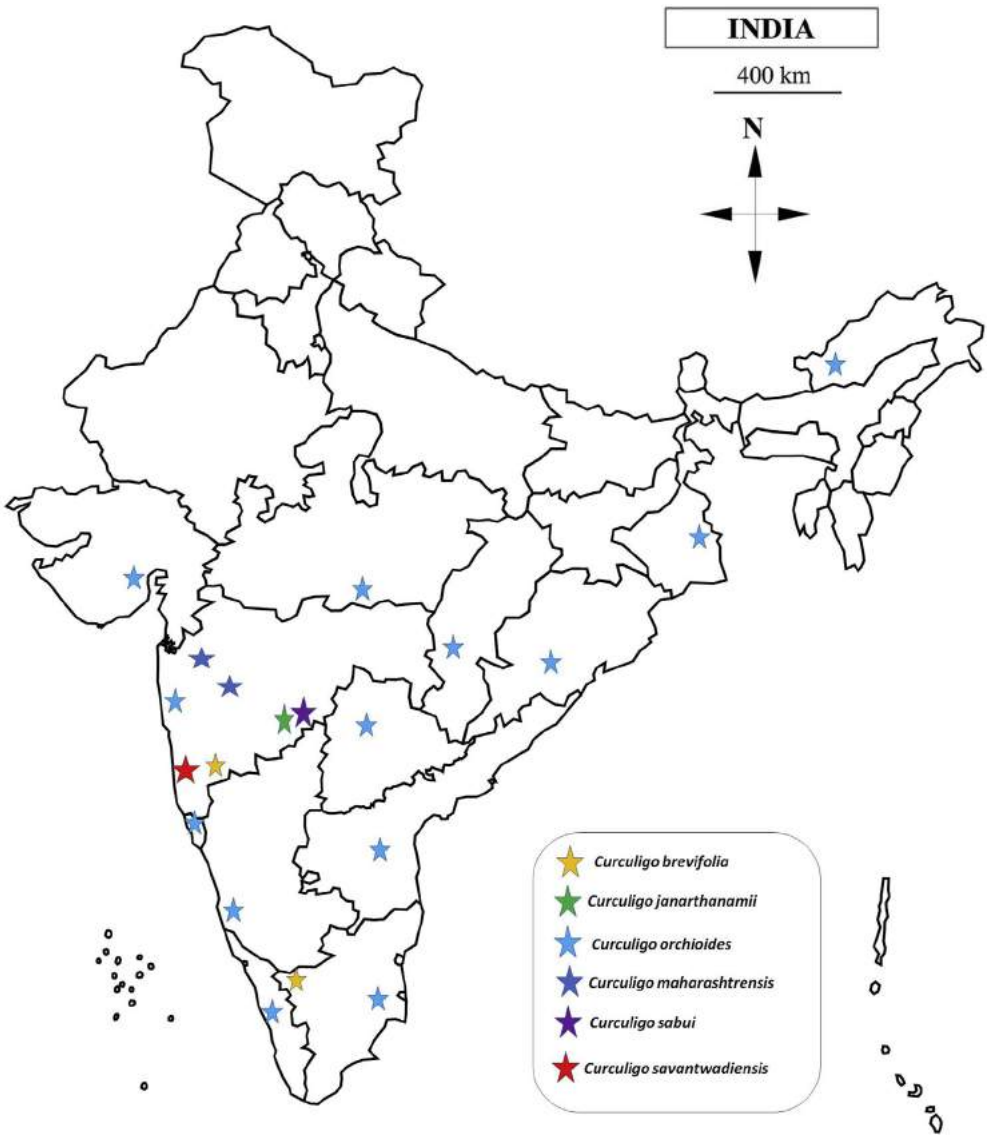

Figure 4. Distribution map of Indian *Curculigo* species; *Curculigo brevifolia, C. janarthanamii*, *C. orchioides, C. maharashtrensis*, *C. sabui*, and *C. savantwadiensis.*

Perennial, acaulescent, polygamous, geophytic herbs, 30–40 cm tall; rhizome vertical, thin, short, 5–6 ×0.3–0.4 cm; young roots fibrous, fleshy, contractile, fasciculate. Leaves pseudopetiolate; lamina linear-lanceolate, 9.5–25.0 × 1–2 cm, bent toward the soil, prominently nerved, margins entire, membranous, mostly glabrous, but sometimes white silky hairs present; leaf tip produces a single bulbil. Inflorescence racemes 3–4 cm long or sometimes less, 3–4 flowered, subtended by single membranous bracts, upper flowers staminate and lower ones bisexual; spathe 3.5 cm × 0.4 cm. Peduncles 1.5–2.4 cm long, whitish, fleshy. Male and bisexual flowers bracteate, bracts green, persistent, broadly ovate-lanceolate, acuminate, 2.8–3.2 × 0.5–0.7 cm, keeled, covered with silky hairs, scarious when dry. Perigone fused into an elongated narrow tube, perigone tube slender, 2.0–2.4 cm long. Tepals 6, yellow, subequal, ovate-lanceolate, 7–10 × 1–2 mm, entire, apex cucullate, glabrous above, dull-white beneath, covered by 1–2 mm long white silky hairs. Staminate flowers with perigone tube 2.5–3.0 cm long bearing perigone segments and anthers (ovary, style, and stigma absent); stamens 6, uniseriate, opposite to perigone lobes, sagittate, basifixed; filaments 1.2–2 mm long arising from the base of perigone lobes, glabrous; anthers yellow, 4.5–5.0 × 0.6–0.7 mm, anther lobes slightly unequal, opening by longitudinal slits along margins. Bisexual flowers with perigone tube 3–4 cm long; stamens 6, uniseriate, opposite to perigone lobe, basifixed, base sagittate; filaments arising from the base of the perigone lobes, 1.2–2.0 mm long, glabrous; anthers yellow 4.5–5.0 × 0.6–0.7 mm, lobes unequal, opening by longitudinal slits. Ovary inferior, 3-locular, villous; ovules 1–2 per locule; style yellowish 2–3 mm long (above perigone tube), glabrous, fleshy; stigma erect with three rows of papillate ridges along with the style. Capsule indehiscent, 11–12 × 3–4 mm, enclosed within old leaf sheath, sparsely hairy; beak 1.5–2 mm long. Seeds 2, ellipsoid, 3–4 mm long, globose, black, glossy, rough (with wavy lines), beak knob-like, curved inside.

Phenology. Flowering and fruiting from July to August.

Distribution. This species is known from the margins of semi-evergreen forests in the Western Ghats: Maharashtra and Tamil Nadu.

*Habitat and ecology***.** This species grows along the margins of semi-evergreen forest in humus-rich soil associated with *Adiantum*

philippense L., *Commelina benghalensis* L., *Dioscorea bulbifera* L., *Strobilanthes callosa* Nees, and *Terminalia paniculata* Roth. We found intermixed populations of *C. orchioides* and *C. brevifolia*, but the latter species can be easily recognized in the field by its bulbils at the tips of leaves.

Discussion

Our reconstructed phylogenetic analyses resulted in the three clades observed by Kocyan et al. (2011), namely *Curculigo* clade, *Hypoxis* clade, and *Pauridia-Empodium* clade. This study placed *Curculigo janarthanamii* in the *Molineria capitulata* subclade and *Curculigo sabui* in *Curculigo orchioides* subclade within the *Curculigo* clade (Figure 1).

The resurrected species *C. brevifolia* is also phylogenetically placed in *Curculigo orchioides* subclade and shows a close phylogenetic relationship with the newly added *Curculigo* species from Maharashtra (ML BS = 100 and PP = 1) and with *C. orchioides* (Figure 1) as well. In addition, this phylogeny supports the recent taxonomic revisions made in the Hypoxidaceae family (Gore and Gaikwad 2018; Kocyan and Wiland-Szymańska 2016; Liu et al. 2012; Snijman and Kocyan 2013).

Cytological attributes like the small size of the chromosomes and low chromatin content support Hypoxidaceae as a separate family (Lakshmi 1980). Therefore, cytology can be used as an additional tool for the delimitation of species. Karyological data such as chromosome number and karyotype asymmetry are useful in inferring evolutionary relationships within plants (e.g. Gosavi et al. 2011), while in *C. orchioides*, vegetative bulbils are absent, and the karyotype is constituted by only submetacentric chromosomes. Asymmetric indices also supported the derivative nature of *C. brevifolia* where both CV_{CL} and M_{CA} are higher than in *C. orchioides*. Different chromosome numbers, i.e. $2n$=18, 36, and ca. 50, were reported in *C. orchioides* (Raghavan 1957; Sato 1942; Sharma and Battacharyya 1960; Sharma and Ghosh 1954). The detailed karyotype formula for *C. orchioides*$2n$=18 (2L+2M+14S) was given by Sheriff (1946). Eksomtramage et al. (2013) studied the karyotype of some Thailand Hypoxidaceae species and reported karyotypes of *C. ensifolia*, *C. latifolia*, *C. megacarpa*, and *C. villosa*. Karyotype formula of Thailand *Curculigo* species with an asymmetric karyotype, including metacentric, submetacentric, and subtelocentric chromosomes i.e. *C. ensifolia* (4m+8sm+6st), *C. latifolia* (2m+14sm+2st), *C. megacarpa* (2m+12sm+4st), and *C. villosa* (4m+10sm+4st). Gholave et al. (2019) reported the karyotype formula of *C. janarthanamii* (2m+14sm+2st). The karyotype formula of *C.brevifolia* is (2st +16sm) and indicates an affinity to *C. orchioides* closer than to other species.

In conclusion, the present study provides morphological, cytological, and molecular evidence for the resurrection of *Curculigo brevifolia,* as well as shows the phylogenetic placement of *C. janarthanamii* and *C. sabui*. This study also provides the taxonomic key for the identification of Indian *Curculigo* species and shows their distribution within India (Figure 4).

Identification key for Indian species of Curculigo

1. Fruit a berry 2
– Fruit a capsule 5
2. Plants having bulbils at the tip of leaves for vegetative reproduction..... *C. brevifolia*
– Plants without bulbils at the tip of leaves for vegetative reproduction..... 3
3. Flowers arise in a bunch of five to six together before..... *C. savantwadiensis*
– Flowers arise with leaves or after leaves 4
4. Flower one or two from the center of leaves..... *C. maharashtrensis*
– Flowers in raceme, lowest bisexual and upper male arise from leaf axils..... *C. orchioides*
5. Capsule dehisces by three-loculicidal valves or irregularly; seeds 8 to 20, seed coat smooth without striations ..... *C. janarthanamii*
– Capsule dehisces by longitudinal slit; seeds 3 to 12, seed coat with irregular striations..... *C. sabui*

Declaration of competing interest

The authors declare that they have no known competing financial interests or personal relationships that could have appeared to influence the work reported in this paper.

Acknowledgments

We are grateful to the Principals of K.V.N. Naik Arts, Commerce and Science College, Canada Corner, Nashik, and Walchand College of Arts and Science, Solapur, for providing research facilities. Thanks to Dr. Sharad Kambale for correcting the initial draft of the manuscript. Rohit Mane is thankful to the Rajiv Gandhi Science and Technology Commission (RGSTC) Government of Maharashtra. This research was supported by Basic Science Research Program through the National Research Foundation of Korea (NRF) funded by the Ministry of Education (NRF-2016R1A6A1A05011910).

Appendix A. Supplementary data

Supplementary data to this article can be found online at https://doi.org/10.1016/j.japb.2021.08.002.

References

Aiton WT. 1811. *Hortus Kewensis; or, a Catalogue of the Plants Cultivated in the Royal Botanic Garden at Kew. London*. ed. 2.. p. 253.
Almeida M, Yadav S. 2009. Hypoxidaceae. In: Almeida MR, editor. *Flora of Maharashtra 5b*. Mumbai: Blatter Herbarium. pp. 401–402.
Baker JG. 1878. A synopsis of Hypoxidaceae. *Journal of the Linnean Society Botany* 17: 93–126.
Chandore AN, Tamboli AS, Borude DB, et al. 2021. *Pogostemon jaitapurensis* (Lamiaceae), a new species from India based on morphological and molecular evidence. *Phytotaxa* 502:28–50.
Colla A. 1826. Illustrationes et Icones Rariorum Stirpium quae in ejus Horto Ripulis florebant Anno 1825, addita ad Hortum Ripulensem, Appendice II. *Memorie delle Reale Accademia Scienza di Torino* 31:317–358.
Cooke T. 1908. *Flora of the Presidency of Bombay*, vol. 2. London: Taylor & Francis. pp. 747–748.
Darriba D, Taboada GL, Doallo R, et al. 2012. jModelTest 2: more models, new heuristics and parallel computing. *Nature Methods* 9:772–775.
Edgar RC. 2004. MUSCLE: a multiple sequence alignment method with reduced time and space complexity. *BMC Bioinformatics* 5:113–131.
Eksomtramage L, Kwandarm M, Purintavaragul C. 2013. Karyotype of some Thai Hypoxidaceae species. *Songklanakarin Journal of Science and Technology* 35: 379–382.
Farris JD, Kallersjo M, Kluge AG, et al. 1994. Testing significance of incongruence. *Cladistics* 10:315–319.
Fofana B, Harvengt L, Jardin P, et al. 1997. New primers for the polymerase chain amplification of cpDNA intergenic spacers in *Phaseolus* phylogeny. *Belgian Journal of Botany* 129:118–122.
Gaikwad SP, Gore RD, Garad KU, et al. 2019. *Curculigo sabui* sp. nov. (Hypoxidaceae), a new species from Balaghat Ranges of Maharashtra, India. *Nordiac Journal of Botany*:e02340.
Gamble JS, Fischer CES. 1956. *Flora of the Presidency of Madras*, vol. III. Calcutta: Botanical Survey of India. Ulmaceae to Gramineae, Addenda, and Index.
Gene Codes Corporation. 2012. *Sequencher 5.1*. Ann Arbor, Michigan: Gene Codes Corporation [EB], http://genecodes.com/.
Gholave AR, Mane RN, Gore RD, et al. 2019. Karyomorphology of *Curculigo janarthanamii* (Hypoxidaceae): An Important Medicinal Plant from Maharashtra, India. *Cytologia* 84:1–3.
Gore RD, Gaikwad SP. 2018. *Curculigo janarthanamii* (Hypoxidaceae), a new species from Maharashtra, India. *Phytotaxa* 357:72–76.

Gosavi KVC, Lekhak MM, Chandore AN, et al. 2011. Karyology of *Barleria grandiflora* Dalzell (Acanthaceae), a potential ornamental endemic to Northern-Western Ghats of India. *Nucleus* 54:133–136.
Govaerts R. 2016. *World checklist of Hypoxidaceae*. Facilitated by the Royal Botanic Gardens, Kew. Available at: http://apps.kew.org/wcsp/. (Accessed 20 March 2016).
Hall TA. 1999. BioEdit: a user-friendly biological sequence alignment editor and analysis program for Windows 95/98/NT. *Nucleic Acids Symposium Series* 41: 95–98.
Hooker JD. 1892. *Flora of British India 6*. London: L. Reeve & Co. p. 793.
Karthikeyan S, Jain SK, Nayar MP, et al. 1989. *Florae Indicae Enumeratio: Monocotyledonae*. Kolkata: Botanical Survey of India. p. 435.
Kocyan A, Snijman DA, Forest F, et al. 2011. Molecular phylogenetics of Hypoxidaceae – Evidence from plastid DNA data and inferences on morphology and biogeography. *Molecular Phylogetics and Evolution* 60:122–136.
Kocyan A, Wiland-Szymańska J. 2016. *Friedmannia*: a new genus from the *Seychelles* and the beginning of a generic realignment of *Curculigo* (Hypoxidaceae). *Phytotaxa* 283:54–64.
Kress WJ, Erickson DL, Jones FA, et al. 2009. Plant DNA barcodes and a community phylogeny of a tropical forest dynamics plot in Panama. *Proceedings of the National Academy of Sciences of the United States of America* 106:18621–18626.
Kumar S, Stecher G, Tamura K. 2016. MEGA7: Molecular Evolutionary Genetics Analysis version 7.0 for bigger datasets. *Molecular Biology and Evolution* 33: 1870–1874.
Lakshmi N. 1980. Cytotaxonomical studies in eight genera of Amaryllidaceae. *Cytologia* 45:663–673.
Levan A, Fredga K, Sandberg AA. 1964. Nomenclature for centromeric position on chromosomes. *Hereditas* 52:201–220.
Levin RA, Wagner WL, Hoch PC, et al. 2003. Family-level relationships of Onagraceae based on chloroplast *rbc*L and *ndh*F data. *American Journal of Botany* 90: 107–115.
Liu KW, Xie GC, Chen LJ, et al. 2012. *Sinocurculigo*, a new genus of Hypoxidaceae from China based on molecular and morphological Evidence. *PloS One* 7:e38880.
Matthew KM. 1982. *The flora of the Tamilnadu Carnatic*, vol. 3. St. Joseph's College: Rapinat Herbarium. pp. 1627–1628.
Miller MA, Pfeiffer W, Schwartz T. 2010. Creating the CIPRES Science Gateway for inference of large phylogenetic trees. In: *Proceedings of the Gateway Computing Environments Workshop (GCE), New Orleans, LA, pp 1–8*.
Nayar TS, Sibi M, Beegam AR. 2014. *Flowering plants of the Western Ghats, India*. Palode: Jawaharlal Nehru Tropical Botanic Garden and Research Institute. p. 1053.
Paterson A, Brubaker C, Wendel J. 1993. A rapid method for extraction of cotton (*Gossypium* spp.) genomic DNA suitable for RFLP or PCR analysis. *Plant Molecular Biology Report* 11:122–127.
Peruzzi L, Eroğlu HE. 2013. Karyotype asymmetry: again, how to measure and what to measure? *Comparative Cytogenetics* 7:1–9.
Raghavan RS. 1957. Chromosome numbers in Indian medicinal plants. *Proceedings of the National Academy of Sciences, India, Section B: Biological Sciences* 45:294–298.
Ronquist F, Teslenko M, Van der Mark P, et al. 2012. MrBayes 3.2: efficient Bayesian phylogenetic inference and model choice across a large model space. *Systematic Biology* 61:539–542.
Sato D. 1942. Karyotype alteration and phylogeny in Liliaceae and allied families. *Journal of Japanese Botany* 12:57–132.
Sharma AK, Bhattacharyya NK. 1960. An investigation on the scope of a number of pretreatment chemicals for chromosome studies in different groups of plants. *Journal of Japanese Botany* 17:152–162.
Sharma AK, Ghosh C. 1954. Further investigation on the cytology of the family Amaryllidaceae and its bearing on the interpretation of phylogeny. *Genetica Iberica* 6:91–100.
Sheriff A. 1946. The karyotype of Curculigo orchioides Gaertn. and its relation to the karyotypes in other Amaryllidaceae. *Current Science* 15:354.
Snijman DA, Kocyan A. 2013. The genus *Pauridia* (Hypoxidaceae) amplified to include *Hypoxis* sect. *Ianthe, Saniella* and *Spiloxene*, with revised nomenclature and typification. *Phytotaxa* 116:19–33.
Soltis PS, Soltis DE, Smiley CJ. 1992. An *rbc*L sequence from a Miocene Taxodium (bald cypress). *Proceedings of the National Academy of Sciences of the United States of America* 89:449–451.
Stace CA. 2000. Cytology and cytogenetics as a fundamental taxonomic resource for the 20th and 21st centuries. *Taxon* 49:451–477.
Stamatakis A. 2014. RAxML version 8: a tool for phylogenetic analysis and post-analysis of large phylogenies. *Bioinformatics* 30:1312–1313.
Stebbins GL. 1971. *Chromosomal evolution in higher plants*. London: Edward Arnold. pp. 1–116.
Swofford DL. 2002. *PAUP*. Phylogenetic Analysis Using Parsimony (*and Other Methods)*. Sunderland, Massachusetts: Sinauer Associates. Version 4. .
Taberlet P, Gielly L, Pauto G, et al. 1991. Universal primers for amplification of three non-coding regions of chloroplast DNA. *Plant Molecular Biology* 17:1105–1109.
Talavera G, Castresana J. 2007. Improvement of phylogenies after removing divergent and ambiguously aligned blocks from protein sequence alignments. *Systematic Biology* 56:564–577.
Tamboli AS, Dalavi JV, Kadam SK, et al. 2021. New molecular phylogenetic evidence for Indian endemic species of the tribe Merremiae, Convolvulaceae. *Plant Biosystems* (in press).
Thiers B. 2020. *Index herbariorum: A global directory of public herbaria and associated staf*. New York: New York Botanical Garden's Virtual Herbarium. Available at: http://sweetgum.nybg.org/science/ih/ [Date accessed- multiple times in 2020].
Wight R. 1853. *Icones plantarum Indiae Orientalis:or figures of Indian plants*. Available at: https://www.biodiversitylibrary.org/page/781559 [Date accessed- multiple times in 2020].

24×7 Water Supply System for Mandrup Town, Tal-South Solapur, Dist-Solapur, Maharashtra.

K C Mujawar^1, P D Mali^2, Unale P L ^3 Prajakta. et.al.^4,

1. Associate Professor, Department of Civil Engineering, N.B. Navale Sinhgad College of Engineering, Kegaon, Solapur
2. HOD , Geology department, Walchand college of Arts and Science Solapur
3. Assistant Professor,SES, PAH Solapur university,solapur.
4. BE students, Department of Civil Engineering, N.B. Navale Sinhgad College of Engineering, Kegaon, Solapur

Abstract

Water is a precious natural resource and plays a significant role in our lives. Over the past few years, there has been an increase of water shortages in several parts of the world. It is vital that ideal measures are put in place to help to reduce the high rate of water loss.

The term continuous water supply – refer to the supply of potable water to end users through a system of pipes-covering interlinked bulk transmission or distribution system which are continuously full and under positive pressure throughout their whole length, such that the end user may draw off water at any time of the day or night, 24x7 throughout the year. This is by itself an important aim for any water supply system. Continuous supply has two main advantages. One is that people can draw water when they need. The second advantage is not holding contamination. When pipes are empty most of time, contamination can seep in through cracks and gaps. A pipe carrying 24 hours a day, on the other hand, will not allow this as the water pressure is acting centrifugally. In India, according to the Ministry of Urban Development (MoUD); continuous potable water supply to every households are directly related with the Service Level Benchmark (SLB) of the city. This study is applied research and it designs and builds a detail project report for 24x7 water supply system at Mandrup town of south solapur taluka ,District Solapur. In the study area the performance of the water distribution system under current demand is inefficient. Our study includes feasibility study, software based hydraulic design, operation and maintenance strategy and economic feasibility for the project by studies of research paper, case study, census data, need and demand of the future.

Keywords: 24x7 water supply system**,** Economic feasibility**,** water meter**,** AutoCAD software, strategy plan, census data

I.Introduction

Water is a precious natural resource and plays a significant role in our lives. Over the past few years, there has been an increase of water shortages in several parts of the world. It is vital that ideal measures are put in place to help to reduce the high rate of water loss. It is vital that ideal measures are put in place to help to reduce the high rate of water loss. With the change in climate patterns, people need to be aware of the alarming water shortage that we face currently and the imminent danger of severe shortage in the future. Various methods can be implemented to address the water problem in the most area.

The supply of water in various corporation and cities may last for just two or three hours once in a week or every other day; it could be even less in certain places. The water that is supplied not good quality water, which leads to water born diseases and infections .The term continuous water supply – refer to the supply of potable water to end users through a system of pipes-covering interlinked bulk transmission or distribution system which are continuously full and under positive pressure throughout their whole length, such that the end user may draw off water at any time of the day or night, 24x7 throughout the year. This is by itself an important aim for any water supply system. Continuous supply has two main advantages. One is that people can draw water when they need. The second advantage is not holding contamination. When pipes are empty most of time, contamination can seep in through cracks and gaps. A pipe carrying 24 hours a day, on the other hand, will not allow this as the water pressure is acting centrifugally.

On one hand the poor availability of drinking water implies huge loss in terms of time, efforts and resources. On the other hand, the consumption of contaminated water has adverse implication on human health and productivity.Departments and agencies like CGWB and CPCB monitor water quality.The study is towards 24x7 water supply and assessments and remediation. Safe and sufficient good quality water is one of the most crucial ingredients of sustainable development. Implementation of 24x7 water supply is a basic need which is a norm in the developed world. 24x7 water supply actually reduces water usage as people don't store and waste water.

II.Aims & Objectives

- To provide 24x7 water supply to people of mandrup town
- To provide good health to the people through good quality potable water
- People can pay as they use
- People can pay at higher rate when using higher per capita water
- To conserve water
- To reduce water loss using a pipe carrying water 24 hours a day

III.Study area

Mandrup town is situated along Vijaypur –Mohol bypass SH-149,3 km from NH-65 on the boundary of karnataka in south solapur taluka , District Solapur of Maharashtra state. Mandrup is fast growing town because now declared as co- tahsil of south Solapur taluka Also mandrup has centre place of 21 villages of South Solapur taluka and Educational Institutes, co-op societies etc. Hence people prefer to settle at Mandrup nowadays.

Scheme Details

Water supply scheme for Mandrup was executed in year 2008, for projected population of 6000 by directly from Bhima River as perennial source without treating the water. The rate of water supply was 40 LPCD.

Key Plan

The above mentioned existing water supply scheme was found insufficient to cater the increased water supply need. Hence as per the increasing population of Mandrup Grampanchayat, We decided to plan and execute 24x7 Water Supply Scheme by adopting Bhima River as perennial source and accordingly the proposal was framed for a projected population of 28680 for year 2035.

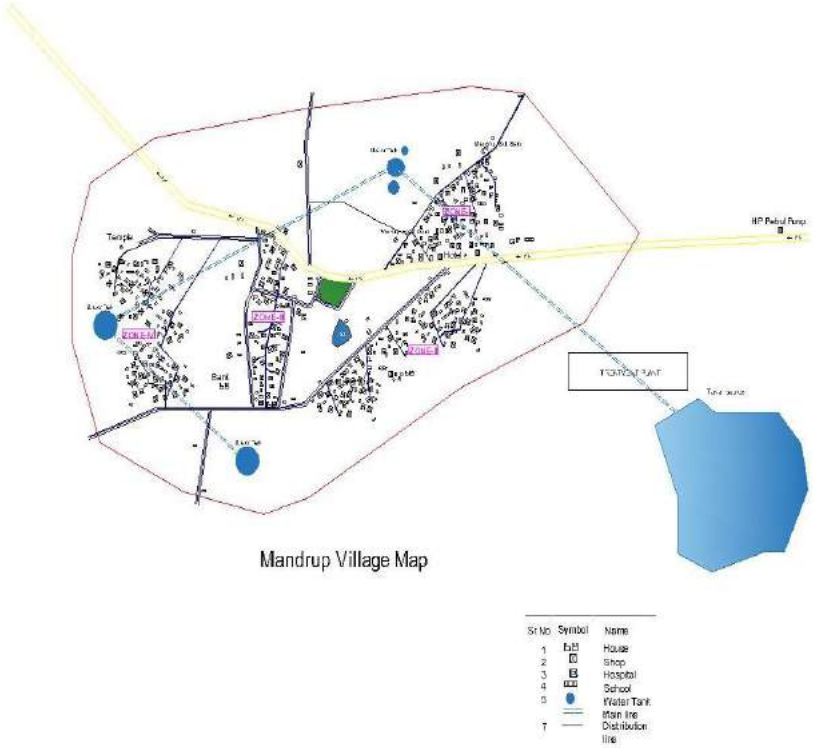

Figure no.1: Illustrates map of mandrup

IV.Methodology

Data collection and design

Data used for study include the population data of the town, general layout map of the area under study, and elevations of nodal junctions in the water distribution system from actual survey and water demand at each node in the distribution network. Data collection has been done from census data and from local water supply department of Mandrup town and projected for 2035 is 28680 using a growth rate of 3.2%. Population demand, fire demand, minor losses, were used to estimate nodal demands. Population demand was obtained by multiplying the population with the percapita demand. The per capita demand, daily peak and hourly peak factors used are 70 lpd (State Water Supply Policy). According to Adeniran &Oyelowo a provision of 10% of the population demand is added as fire demand in the case of fire outbreak. To account for minor losses where there are bends, valves, and fittings, 5% of the total demand was used. From the design, it was found that to convert intermittent to 24x7 water supply system, 85% of the existing network has to be replaced. A property survey was carried out to determine the total number of houses and total number of people residing n the mandrup town. There are technically some possibilities for implementation of 24x7 water supply system, which are different in material and construction technology and the area of Mandrup town is divided into four zones and designed new distribution system ,water treatment plant . Wasteful use of water is remarkably reduced and the reduction is to the extent of 30%. The demand management by making the people aware of the system and the telescopic tariff made this possible.

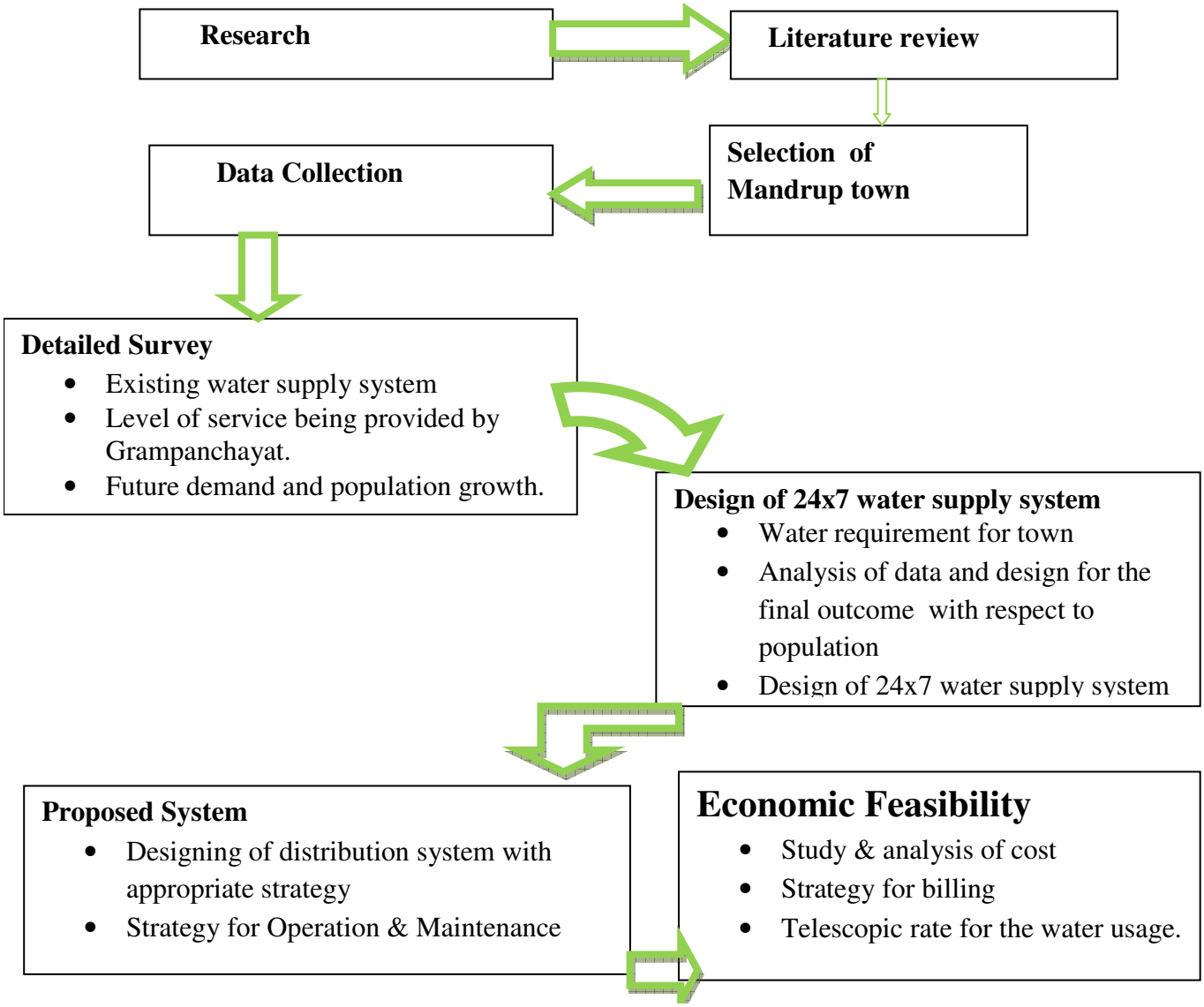

Water Budgeting

Present status of mandrup town water supply and water budgeting

- Population:- 16106
- Rate of water supply:- 70lpcd
- Pumping hours:-16hr's
- Rate of pumping:- 1,31,250 lit/hr
  For 16 hours = 1,31,250 * 16 =21,00,000 lit/day
- Requirement of water :-16106 * 70= 11,27,420 lit/day
- Others sources:-
  1. No of wells: 8No's
     1 Well= 1000 lit

8 well=8000 lit

2. No of Borewells: 74No's
   1 Well= 2000lit
   74 Borewell=1,48,000 lit
3. Live stocks:- 3575No's
   Requirement of water:- 3575 * 60=2,14,500 lit

- **Total Availability of water** = 2100000 +8000+148000=22,56,000 lit=2.25MLD
- **Requirement of water** =13,41,920 lit=1.34MLD
- **Excess water** =2256000 – 1341920=9,14,080 lit=0.91MLD

24X7 water supply scheme to mandrup town

- Population:- 16106
- Rate of water supply:- 70lpcd
- Pumping hours:-11hr's
- Rate of pumping:- 1,31,250 lit/hr
  For 16 hours = 1,31,250 * 11 =14,43,750 lit/day
- Requirement of water :-16106 * 70= 11,27,420 lit/day
- Others sources:-
  4. No of wells: 8No's
     1 Well= 1000 lit
     8 well=8000 lit
  5. No of Borewells: 74No's
     1 Well= 2000lit
     74 Borewell=1,48,000 lit
  6. Live stocks:- 3575No's
     Requirement of water:- 3575 * 60=2,14,500 lit
- Total Availability of water = 1443750 +8000+148000=15,99,750 lit=1.60MLD
- Requirement of water =13,41,920 lit=1.35MLD
- Excess water =1599750 – 1341920= 2,57,830 lit=0.25MLD

Water supply system and budgeting for the year- 2035

- Population:- 28680
- Rate of water supply :- 70lpcd
- Pumping hours :- 16 hours
- Rate of pumping :-131250 lit/hr
  For 16 hours =131250*16=2100000 lit/day
- Requirement of water :- 28680*70=2007600 lit/day
- Other sources :-
  1. No of wells :- 8 no's
     1 well = 1000 lit

8well = 8000 lit

No of Borewells:-74 no's

1Borewell=2000 lit
74 Borewell=148000 lit

2. Live stocks :- 3575 No's
   Requirement of water:- 3575*60 =214500 lit

- Total availability of water =2100000+8000+148000 =2256000 lit=2.25MLD

Requirement of water =2222100 lit=2.22MLD
Excess water = 33900 lit.=0.03MLD

V.Water Distribution system

Present status of water distribution system

The principal source of water supply is Bhima river from the source water supplies without treatment in six zone .The total water drawn from all the sources to mandrup town is approximately 2.25MLD with once in a week supply. However, the untreated water affects on health of people various diseases and infections like gastroenteritis and dengue epidemics. Hence, in the said context the present investigation has emerge as 24x7 water supply to mandrup town

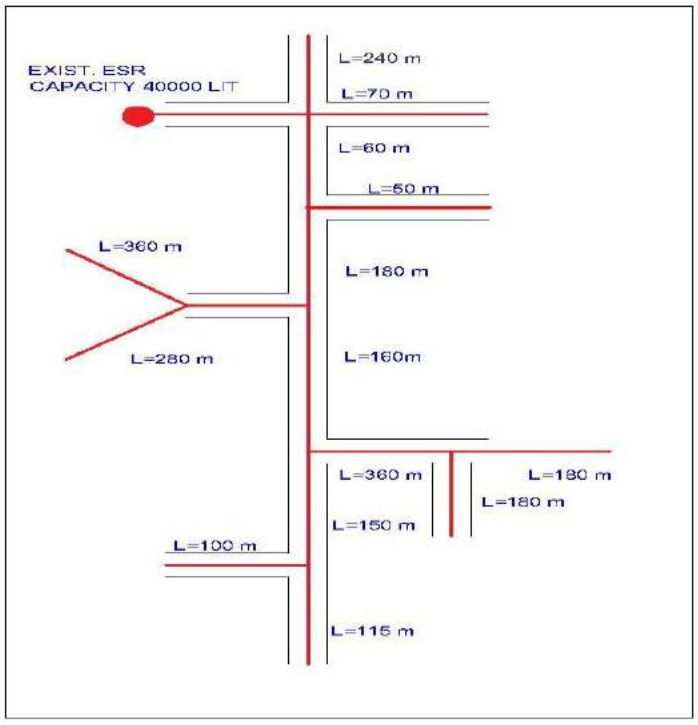

Figure no.2: Illustrates existing water supply distribution system

VI.KEY plan

The system is designed to provide 70 LPCD water for population of 16106 souls. The water distribution system consisted pumping of water from river Bhima to water treatment plant at the rate of 131250 lit/hr through pipeline. The electric motor is of 40 HP. The W.T.P. having conventional alum dosing, flocculation, coagulation, sedimentation, filtration and disinfection by chlorine is adopted. The treated water is pumped to the water distribution tank. The treated and disinfected water from this tank is transferred to the four zones of mandrup town. The projected demand of mandrup town for year 2035 for population 28670 was calculated@70 LPCD and the scheme is framed and designed

Figure no.3: Illustrates base map of Mandrup town

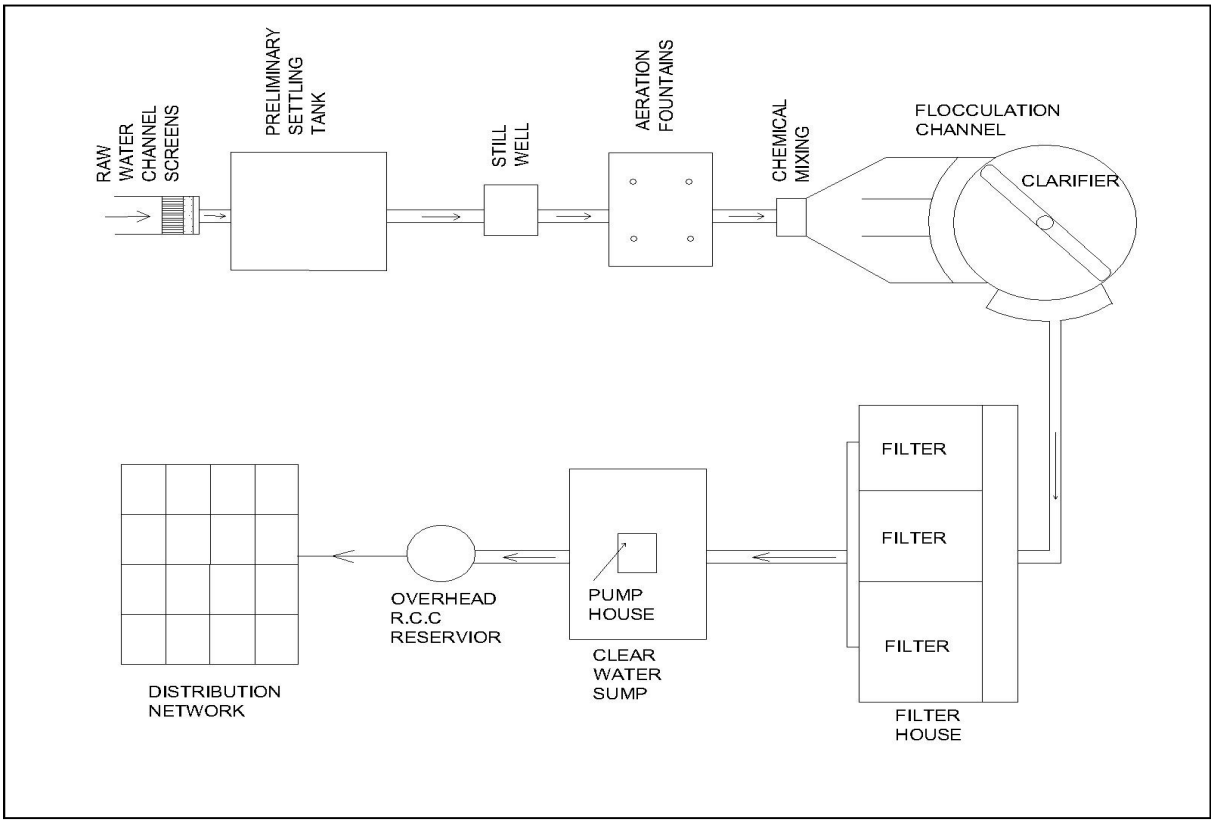

Figure no. 4: Illustrates water treatment Plant (Flow Chart)

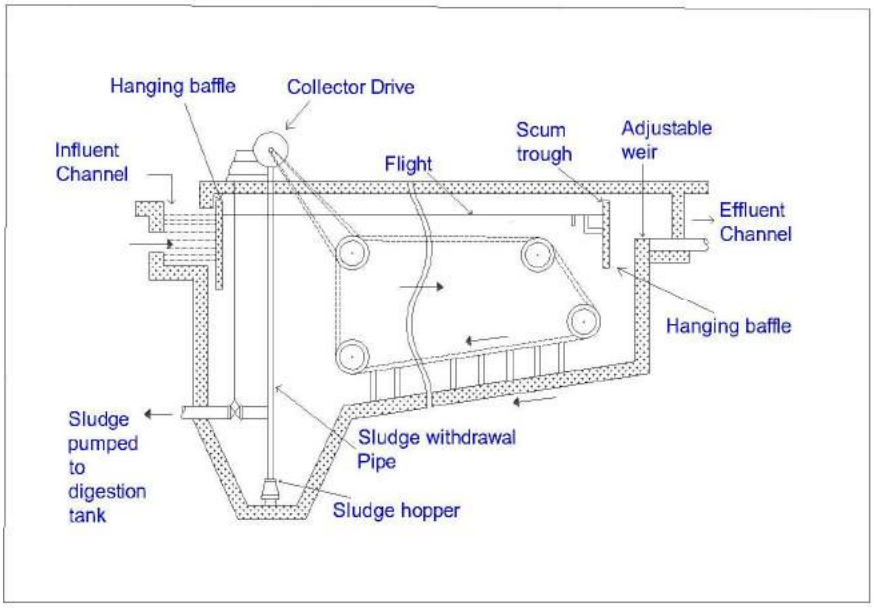

Figure no.5: Illustrates sedimentation tank

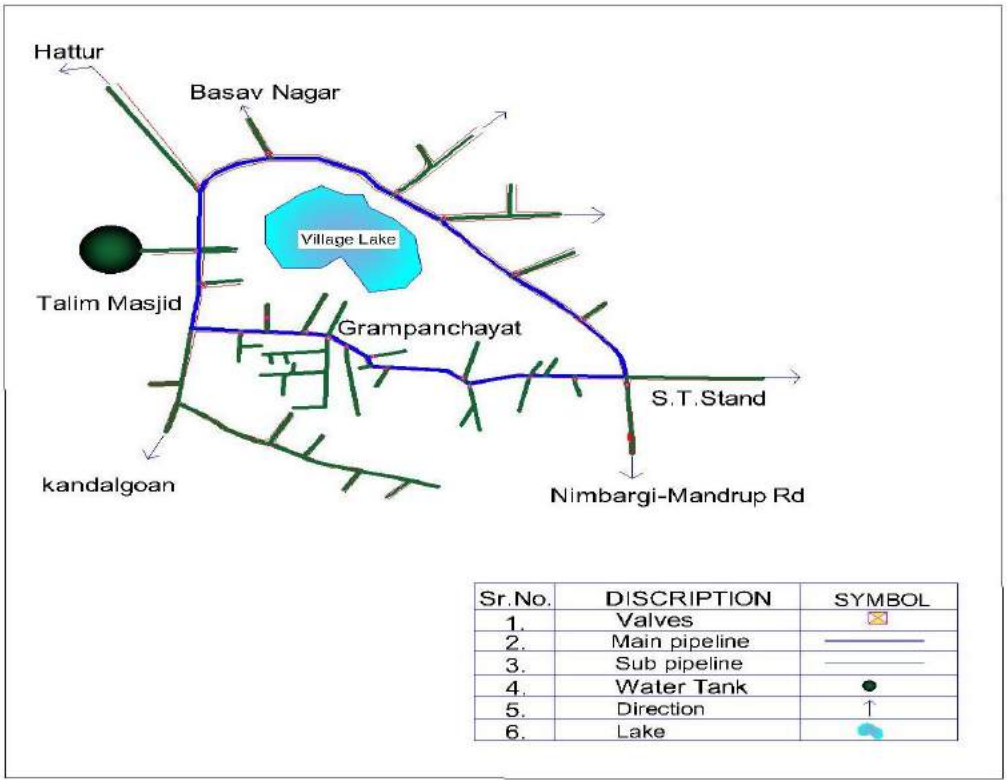

Figure no.6: Illustrates water Distribution System

VII.The house service connection material and methodology

The consumer connection for individual house is with ferrule and by continuous single length MDPE blue pipe from ferrule to the meter in the premises of consumer using electro fusion method. Ferrule is used to avoid illegal water connections and leak proof compression fitting,

Hdpe pipe

The last of the work but important from the point of view of service delivery was distribution network. In this project distribution system network is by HDPE good quality pipes. For the water distribution system the HDPE pipe of continuous 100mt length is used to avoid joints. After 100mt another HDPE pipe is joined with electro fusion coupler. Which also protect free from pipeline leakage and reduces loss of water.

Telescopic meter

The metered distribution of water and charging the consumer on actual consumption of quantity of water basis is also designed. 24 x 7 system with metered water supply and tariff as per actual use. Provided with ferrule and followed by, the bulk water AMR meter. Each water connection has been installed with automatic meter readers (AMR), which take meter reading with the help of radio frequency within the radius of 200 m. It is not necessary to go to the meter for taking readings. The data is fed into computer and accordingly water bill is processed. Since there is no any manual interference to take readings, the billing is accurate

Photo no.1: Illustrates HDPE Pipe

VIII.Economic Feasibility

In India, revenues from water and sewerage services typically cover less than 30% of operating cost. As a result, water and sewerage services have to be heavily subsidized by government. For the better funding and to run project successfully it is recommended to implement project on PPP mode with 90% government shares and 10 % public shares. From the calculation and analysis, it has been founded that one time water meter installation cost per house is Rs1800=00 and yearly operation and maintenance charge for each house is Rs200=00.Due to low pressure of water supply people living in building used to pump the water from ground to the tank on terrace for that they use to operate power pumps.24x7 water supply with high pressure has to save electricity consumption. After reduction of 5 hours pumping for water storage from source saves 150units of electricity daily. When water supply is pure and potable it also keep the people from various diseases and reduces medical expense also.24x7 continuous water supply reduces the cost of water storage equipments

Table no1: Illustrates saving details of mandrup town

Sr No.	Particular	Units	Rate	Total Saving in RS
1	Electricity conservation in pumping	4500units/Month	11.20/unit	50400/month
2	Electricity conservation from Household	11units/house/month (3709 houses x11 unit=40799 units	4.20/unit (40799x4.20)	171355/month
3	Medical expense	3709 Houses	300/house/month	1112700/month
4	Water storage equipments	3709 Houses	90/house/month	333810/month

Photo no.2: Illustrates telescopic meter

.**Electricity Bill**

40 hp motor

40 X 0.746 = 29.84 units /hour = 30 units /hour

1 unit =1 kw/hour

1 unit = 11.20 Rs/unit

For 5 hours reduction in pumping.

30 X 5 = 150 units

150 X 11.20 = 1680 Rs/day

- For 1 month
  =150 X 30 =4500 units
  =4500 X 11.20 = 50400 Rs/month
- For 1 Year
  =365 X 150= 54750 units
  54750 X 11.20 = 613200 Rs /year

  Saving in Medical expense

  Due to pure water used Reduction in diseases
  For 1 person =60 Rs/Month
  Assume 5 members in 1 House
  For 1 Family = approx. Rs 60 x 5 = 300 Rs/Month
  For all Houses =3709 x 300 = 1112700 Rs/Month

For 1 Year =1112700 x 12 = 13352400 Rs/Year

Reduces expense of Storage Equipments

Purchase and repair of storage equipment

For 1 Family = approx.800 Rs/ Year

For all Houses =3709 x 800 = 2967200 Rs/year

IX.Benefits of the study :

- Improvement in delivery time and services
- Providing good quality of Water
- Helps to decrease water borne illnesses in children
- Reduction in wastage of water and water loss
- Shifting control of the distribution system from Valve man to the Consumer
- Saving in Electricity & helping clean development initiatives
- Reduction in operation cost

X.Conclusion

Mandrup town has need to convert its water distribution system to 24x7 water supplies to achieve service level benchmark. There are technically three possibilities for implementation of 24x7 water supply system, which are different in material and construction technology For usage of water, the telescopic tariff has been design in 4 slabs according to usage of water. 24x7 water supply system is equally depended on technical, social, political and financial aspect of the project. This project is highly recommended better planning and operation strategy for successful completion of project.

References

Rutva N. Gohil1 1 PG Student ME-IV, Department of Civil Engineering 1S.S.E.C, Bhavnagar, Gujarat, India.

Evaluation of Intermittent Water Supply System and Design of 24x7 for a residential area in Mysore, Karnataka, India.

R. Sanjay and V. Dahasahasra Member Secretary

Study on Implemented 24x7 Water Supply Schemes Mane D.B 1 , Dhumal J.R 2 , Shetage A.A 3 , Bamanikar A.K 4

Agrawal, V., and Jagetai, M. (1997). Hydrochemical assessmentof groundwater quality in Udaipur city, Rajasthan, India. Proc. of National conference on dimensions of environmental stress in India. Department of Geology, MS University, Baroda, India, 151–154.

Altekar R.A., (2004) : Drinking water quality, IWWA publication, Mumbai, India, 60 P.

Amrita Singh and Choudhary, S. K, (2011) Chemical Analysis of Groundwater of Nath nagar Block under Bhagalpur District, Bihar (India)". Journal of Environmental Science and Engineering, Vol. 53(1) pp469-474.

Raju, N.J. and Reddy, T.V.K. (2007) Environmental and Urbanization Affect on Groundwater Resources in a Pilgrim Town of Tirupati, Andhra Pradesh, South India. *Applied Geochemistry*, **9**, 212-223.

Ramesh, K. (2008). Hydrochemical studies and effect of irrigation on groundwater quality in Tondiar basin, Tamil Nadu. PhD thesis (Unpublished), Anna University, Chennai, India.

Subba Rao, N. (1993). Environmental impact of industrial effluents in groundwater regions of Visakhapatnam Industrial Complex. Indian Journal of Geology, 65, pp.35–43 .

WHO (2004). Guidelines for drinking-water quality volume 1:recommendations, 3rd edn. WHO, Geneva

WHO. (1989). Health guidelines for the use of wastewater in agriculture and aquaculture. In: Report of a WHO Scientific Group: Technical report series 778, WHO, Geneva, 74.

Prajakta. et.al-BE project group of Prajakta Unale,Sagar Parve, Arati Chavan,PratikshaGilbile, Pradeep Fulsundar, Rama Pise

Analysis of Soil Quality from Mulashi Taluka, Pune District, Maharashtra.

K C Mujawar^1, P D Mali^2, Hiremath. et.al.^3,

1. Associate Professor, Department of Civil Engineering, N.B. Navale Sinhgad College of Engineering, Kegaon, Solapur

2. HOD , Geology department, Walchand college of Arts and Science Solapur

3. BE students, Department of Civil Engineering, N.B. Navale Sinhgad College of Engineering, Kegaon, Solapur

Abstract

The present study carried out to analysis of soil and water quality from Mulashi taluka Pune district, Maharashtra. Study area located in the ranges of Sahyadri Mountains having MSL 629-1256 meters. Location map of the study area is shown in Fig 1.1. The study area is lies between Latitude 18º50' N to 19º20' N and Longitude 73º25' E to 74º15' E. The topology of the area has been characterized by mountain, terraces and flood plains covering area 45.93 sq. km(Fig.no.1.1).Geologically the study area comprise of volcanic rock of Deccan trap with alternating layers of compact massive basalt and vesicular amygdaloidal basalts formed during the Cretaceous- Eocene times. Soil samples from 9 locations were collected in the present investigation. The various parameters determined from soil samples are pH, EC,OC, N, P, K at Solapur District soil testing laboratory Solapur (Table 3.2). Present study was undertaken to learn the soil geochemistry in Mulashi taluka basin Pune district, Maharashtra. The soils of Mulashi basin were loamy,sandy, silty and clayey in nature, alkaline in nature. The various elements are determined in parts per million (ppm).

Keywords: Mulashi taluka, Soil parameter, Clayey, loamy, sandy and silty soils, soil texture,

1. Introduction

The crop growing of soil has enabled humans to build empires and to improvement to what we are today. Man depends on soil and what it produces for food, energy and miscellaneous material. Soil forms very slowly over a period of tens of thousands years, too slow to be noticed. This happens to be the reason why ancient agriculture has erased itself in many places. It was soil and farming on soil led to productivity, which enabled human society to become denser

The important one was to promote agricultural land research on mapped soils so that soil based research finding can be transferred to other areas analogous in climate and soil-site conditions, ascertain the kinds

Further, to monitor the soil health and to forewarn the emerging constraints. Those who mastered agriculture, amassed wealth and power, A soil is a 3-D body occupying the uppermost part of the earth's crust and having properties differing from the underlying rock material as a result of interaction between hydrosphere, biosphere, atmosphere lithosphere etc. Further, its formation is largely controlled by parent rock, climate, geomorphology, relief, biological activity and time. Soils acts as natural sinks and filters for various metals Pendias and Pendias(1984). Geochemical elements in soils have mobility which is largely influenced by soil pore pH, CEC, REDOX potential, Z/r index of metals, organic chelation etc. (Govil et al 1999). The present study was carried out with the objective of identifying the quality of the soil for landslide prospect zonation of Mulashi Taluka, Pune District.

2. Objectives

- Geological study of the area
- To study soil quality of the area
- To provide a decision support tool for managers and planners

3. Study Area

Mulashi Taluka of Pune District, Maharashtra State, India. It is located 58 kms towards the west from District Headquarter 92 kms from the State capital Mumbai. Pune District lies in the Ecologically Sensitive Zone I. Located in the ranges of Sahyadri Mountains having MSL 629-1256 meters. Location map of the study area is shown in Fig 1.1. The study area is lies between longitude18º50' N to 19º20' N and latitude 73º25' E to 74º15' E. The topology of the area has been characterized by mountain, terraces and flood plains covering area 45.93 sq. km (Fig.no.1). Geologically the study area comprise of volcanic rock of Deccan trap with alternating layers of compact massive basalt and vesicular amygdaloidal basalts formed during the Cretaceous- Eocene times. 'Aa' and 'pahoehoe' lava flows of varying thickness constitute the lithology of the study area. 4. Soils of Pune District, Maharashtrais located on Deccan plateau and is divided into 3 sub-regions namely (a) upper Maharashtra plateau (b) lower Maharashtra plateau and (c) lower Maharashtra metamorphic plateau. National Bureau of Soil Survey and Land Use Planning (1995) had categorized Pune District under lower Maharashtra Deccan plateau and upper Maharashtra plateau. The soils are of undulating land with moderately gentle sloping are excessively drained, neutral (pH 6.5-7.5) loamy to clayey-skeletal lithic with moderately water holding capacity and moderate erosion (Fig.no.2 table 1).

The soils in Mulashi Taluka are entisols and inceptisols. The entisols is an order of embryonic soils that have no distinct pedo-genic horizons and represent the initiation of soil profile development. The clayey and loamy, and clay, sandy clay, silty clay, waterbody mask soils are observed in the Mulashi Taluka of Pune District (fig.no.2).

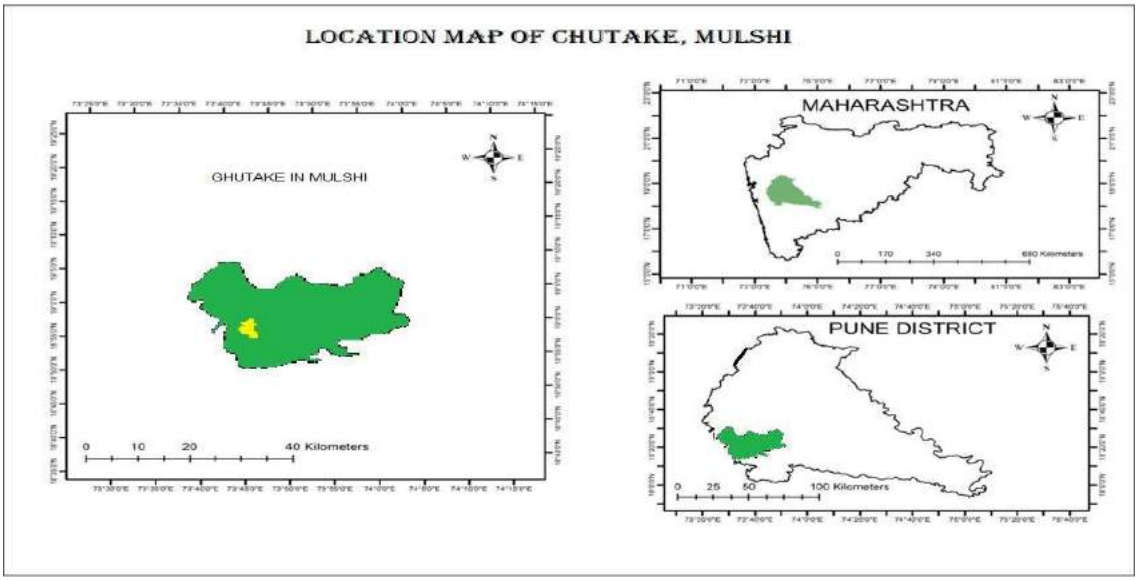

Fig.no.1. Location map of the study are

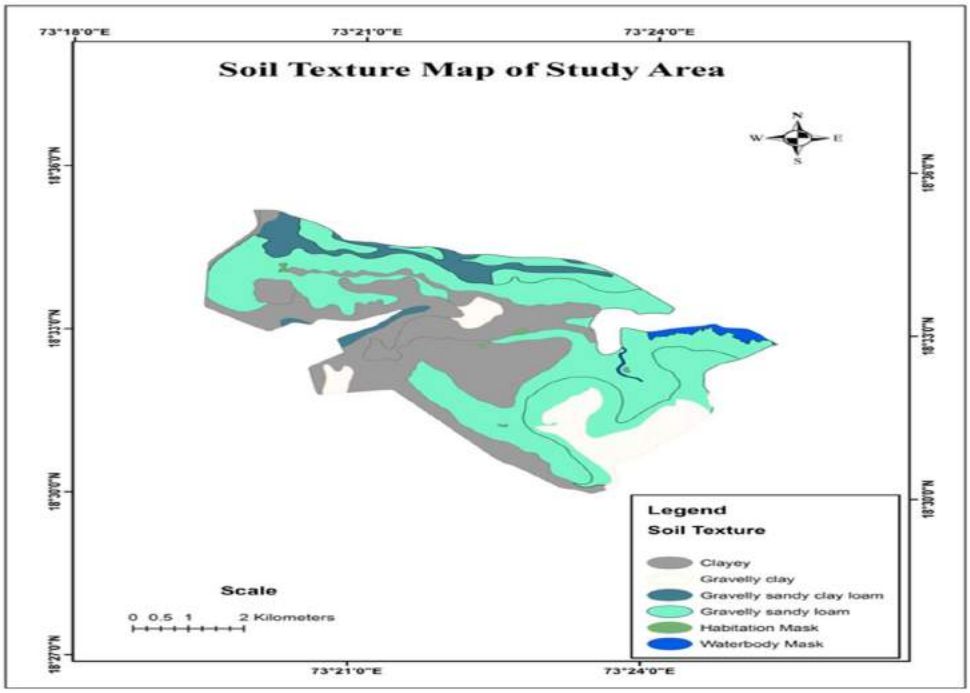

Fig. no.2 Illustrates the soil texture map of the study area

5. Materials and methods for soils

Sample collection, preparation and analysis of Soil

Soil samples from 9 locations have to be obtained with the help of village location map. The objective of the sampling is to collect a proportion of material small enough in volume, which can be coherently transported and handled easily in laboratory. In the present study representative soil-geochemical samples were collected from various locations the soil samples were subjected to sample preparation. This stage includes drying, hand crushing, sieving, grinding and lastly coning and quartering. This stage helps in obtaining a truly representative homogeneous sample. Considerable care was exercised to avoid contamination and finally submitted to District soil testing laboratory Solapur. The various parameters determined from soil samples are pH, EC, OC, N, P, K District soil testing laboratory Solapur. (Table 1).

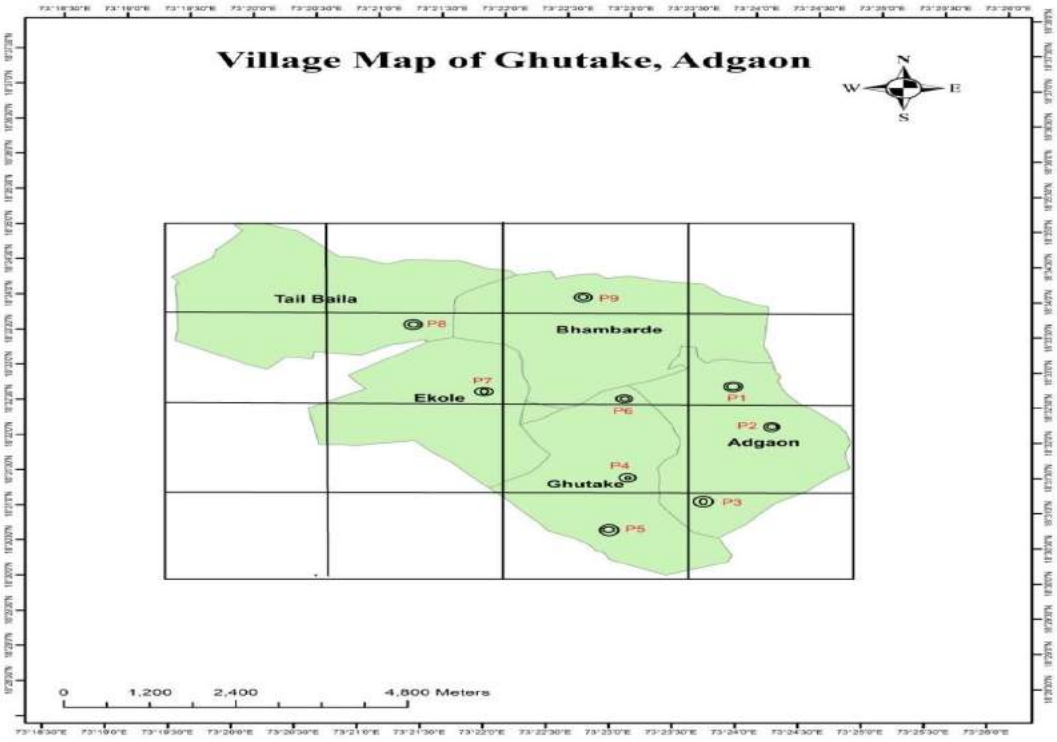

Fig.no.3- Illustrates the soil sample location map of the study area

6. Distribution of Distribution of various parameters in the soils from Mulashi taluka basin

Distribution of pH

The range of pH noticed in the Mulashi Taluka soils are from 6.63-7.05. The figure 4 illustrates the distribution of pH in the soils of investigated area. Relatively higher values of pH are noticed in the surface soils from Ghutake and Adgaon area towards the south east of the basin. Low values of soil pH are observed in and around gravely, chincholi,Barghar coinciding with weathered zeolitic and amygdaloidal basalts

Table no.1. - Illustrates soil parameter of the study area

SR.NO.	LOCATION	PH	EC	OC	N	P	K
1	P1	7.04	0.12	0.76	163	0.54	291.2
2	P2	6.9	0.17	0.43	175	0.62	200.48
3	P3	6.63	0.06	0.76	336	0.58	175.84
4	P4	6.8	0.14	0.76	288	0.61	576.8
5	P5	7.05	0.12	0.31	211	0.9	476
6	P6	6.94	0.1	0.25	363	0.65	76.16
7	P7	7.02	0.09	0.61	146	0.63	125.44
8	P8	6.84	0.12	0.91	243	0.65	444.64
9	P9	6.68	0.08	0.85	151	0.58	161.28

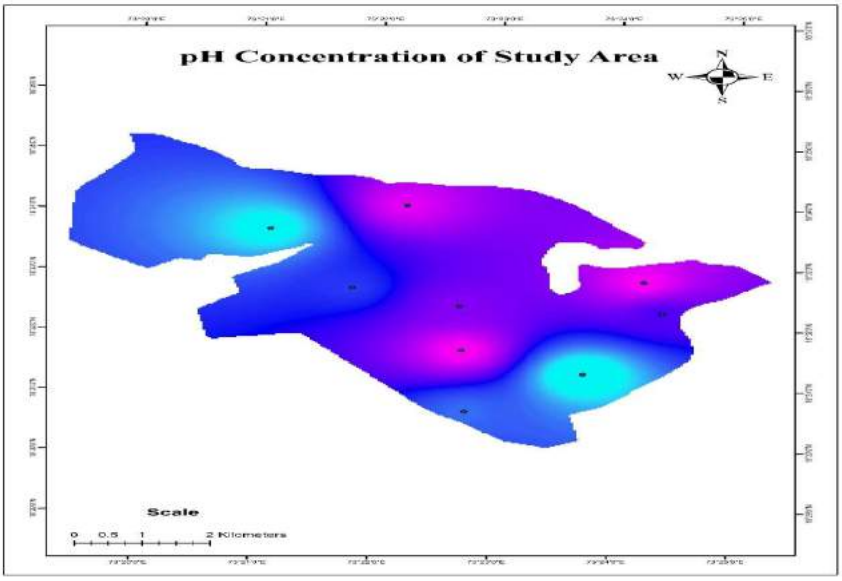

Fig no.4- Illustrates the distribution of PH from study area

Distribution of electrical conductivity

The electrical conductivity in the soils is estimated using conductivity meter. The range of EC in the soils from the area of study is from 0.17- 0.06. The average value for the entire soils from Mulashi Taluka is 0 .11. The high values are found Adgaon, located in the form of broad zones toward north-east parts of the basin. The low values are found near Bhamburde located in the north parts of study

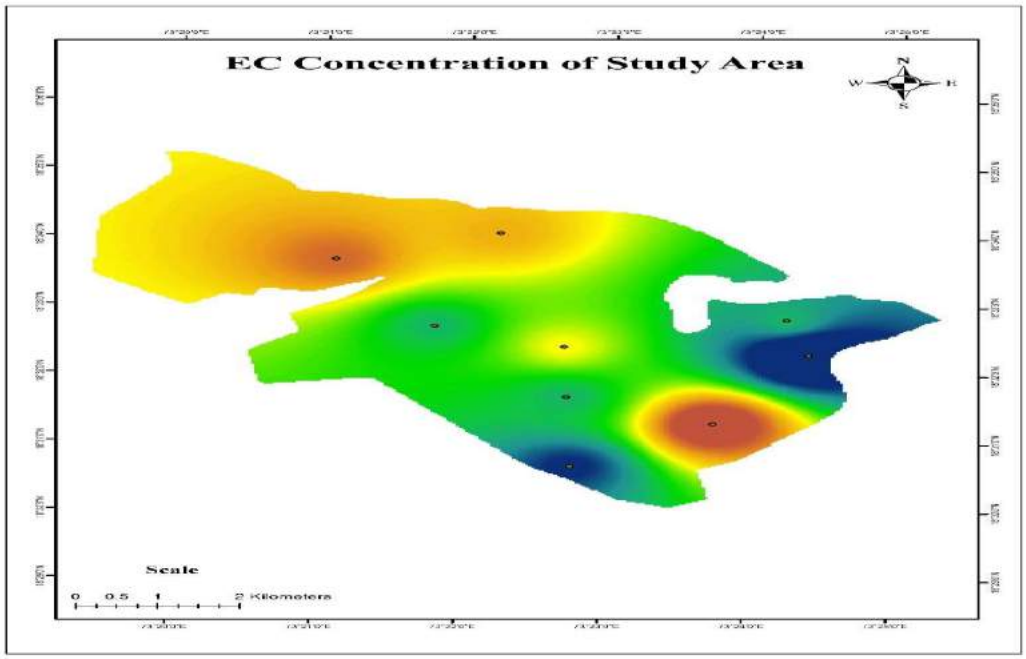

Fig no.5- Illustrates the distribution of EC from study area

Distribution of Nitrogen

The range of Nitrogen concentration in soils is between 146-363 ppm. The average concentration of N in the area is 230.667 ppm. It is observed from the figure 6 the higher concentration (Adgaon) contours are encircled around towards north east of Mulashi Taluka. Lower concentration (Ekole) contours are noticed at upper ridge. The Nitrogen has higher correlation coefficient values with EC, Ca and Mg.

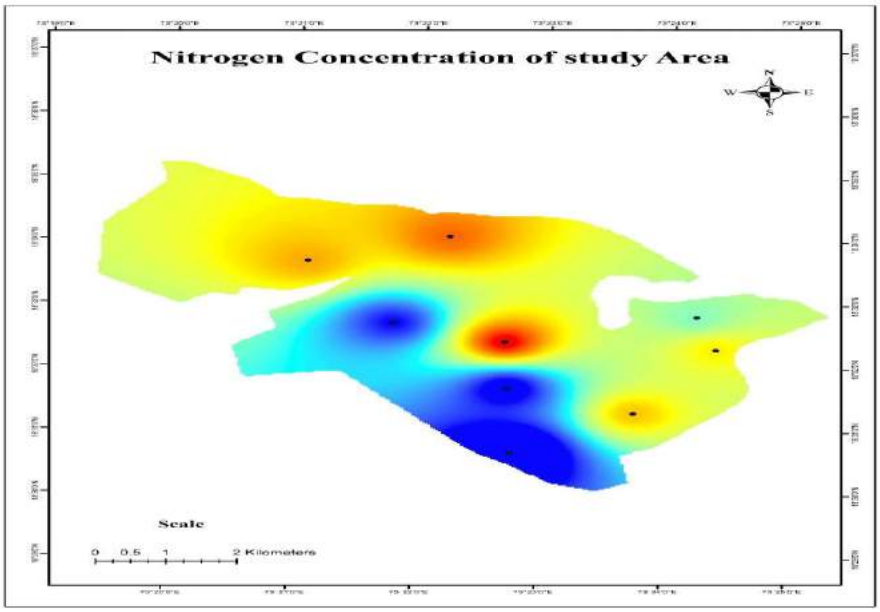

Fig no.6- Illustrates the distribution of Nitrogen from study area

Distribution of Phosphorous

The figure 7shows the dispersion of phosphorous in soils from investigated area. The maximum and minimum values of phosphorous in soils are 0.9 ppm and 0.54 ppm, respectively. The higher values of phosphorous are indicative of application of phosphate fertilizers for agricultural practices in the region and are non-lithogenic in its origin. Further, it does not show any positive correlation coefficient with other parameters. The low values are found Ghedegaon, Taleghar, Near Digaj. The high values are found in some areas of central part and western part of the study area.Application of synthetic fertilizers for cultivation of crops may have resulted in pervasively high values in the above mention region.

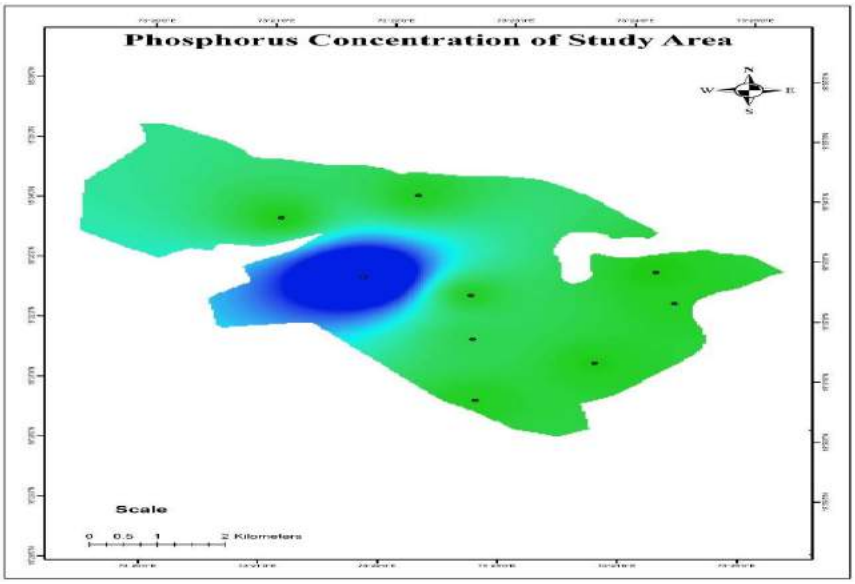

Fig no.7- Illustrates the distribution of Phosphorus from study area

Distribution of Potassium

The range of Potassium concentration in soils is between 76.16-576.8 ppm. The average concentration of K in the area is 280.87 ppm. It is observed from the figure 8 the higher concentration (Ghutake) contours are encircled around towards south of Mulashi Taluka. Lower concentration (Ekole) contours are noticed at upper ridge.

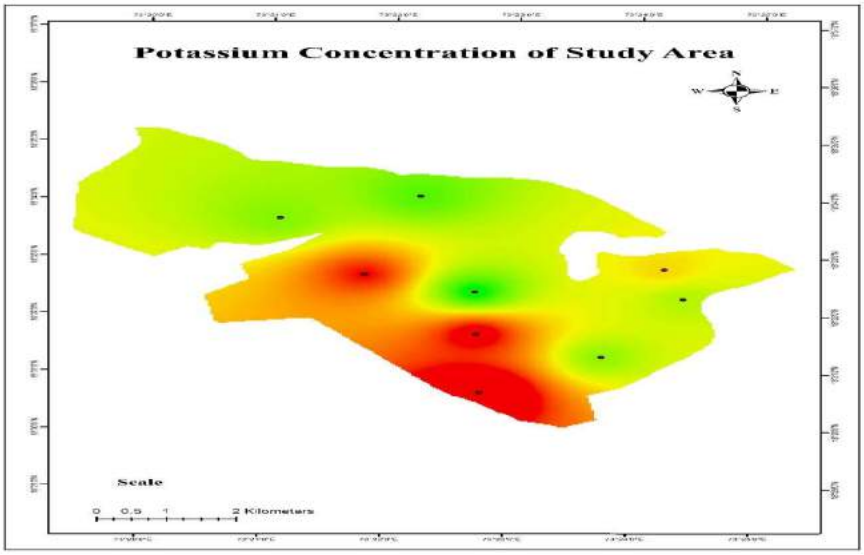

Fig no.8- Illustrates the distribution of Potassium from study area

Distribution of Organic Carbon

The thematic figure 9 illustrates the dispersion of potassium in the soils from the study area. Its minimum value is 0.25 ppm and noticed south of the basin and maximum 0.91 ppm observed at upper ridge. In the above mention region, the high values are found Tail Bailathe low values are found Ghutake.

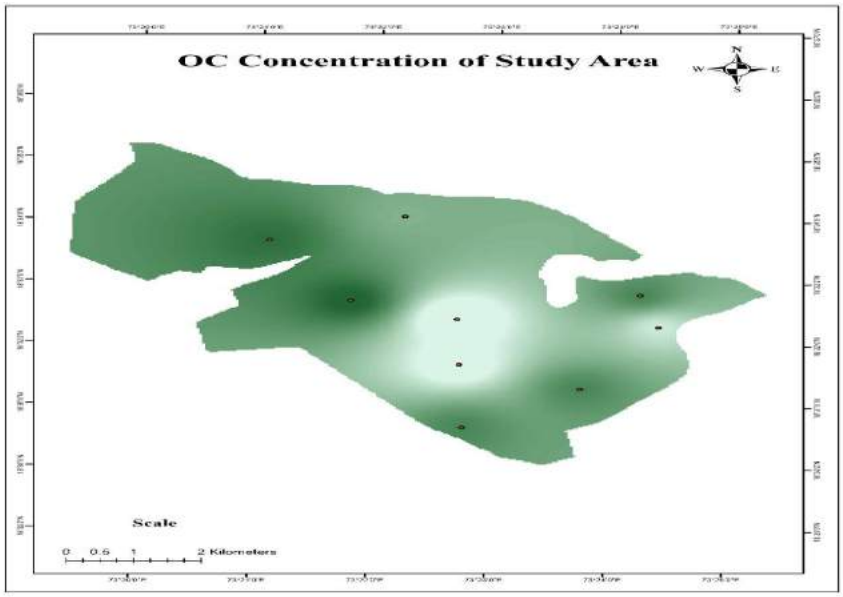

Fig no.9- Illustrates the distribution of OC from study area

7. Conclusion

A soil is a 3-D body occupies the uppermost part of the earth's crust and having properties differing from the underlying rock material as a result of interaction between hydrosphere, biosphere, atmosphere, lithosphere etc. Further, its formation is largely controlled by parent rock, climate, geomorphology, relief, biological activity and time. Soils acts as natural sinks and filters for various metals Pendias and Pendias (1984). In the present study the various parameters pH, EC,OC, N, P, K shows greatvariation in their concentration in the various parts of the Mulashi taluka basin. This gives the actual quality of soil in the basin. Geological and Geomorphologic aspects support the formation of soils such as Clayey, Loamy, Salty and sandy. The soils in the plains of the Mulashi basin are prone to saline and alkaline in nature.

References

[1] KabataPendias A and Pendias H., 1984: Trace elements in soils and plants (2nd Ed) CRC Press Inc., Boca Raton, Florida, 1-3.5 pp.

[2] Kaplay and Patode., 2004: Groundwater pollution due to industrial effluents of Tuppa,New Nanded, Maharashtra, Indian Environmental Geol. Jour.Vol. 46.,871-88

[3] Kelly, W. P.1951:Alkali soils – Their formation properties and Reclamation ,Reinoldpubl.corp, New York.

[4] Krauskopf. K.B., 1967: Introduction to Geochemistry, McGraw Hill, New York, 721 p.

[5] Kumar V.V.R., and Reddy,U.V.B., 2001:Cadmium contamination in soils of Pantancheru Industrial belt,Medak District, Andra Pradesh, India.Environmental geochemistry,Vol.4,No. 192,pp.23-26.

[6] Muller.W and fastaband.H. 1963: The influence of sorbed magnesium on water permeability structural properties of marsh soils Soils fertile 28.1420 p

[7] NBSS and LUP., 1995: Soils of Maharashtra for optimizing land use (Ed) J. Sengal., National Bureau of soil survey and land use planning, Nagpur, Maharashtra, India, 96 p.

[8] Mujawar KC et.al Soil Geochemical Dispersion Pattern around Molybdenite Deposits in Koheda Area, Karimnagar District, Telangana."In the International Journal of Creative Research Thoughts (IJCRT) ,vol-6 Issue-1,Feb-2108,pp2507-2513.

[9] Mujawar KC et.al.Study of Soil Quality from Aprupa watershed basin, Sangola Taluka, Solapur District, Maharashtra,India" In the IOSR Journal of Engineering (IOSRJEN), Vol-8 Issue4,April-2018 pp-22-28.

Hiremath et.al.: BE project group of Gangadhar Hiremath, Basavraj Gudage, Prasad Pomaji, Siddhanth Patil, Sandesh Martande, Siddharth Swami

Eco. Env. & Cons. 28 (January Suppl. Issue) : 2022; pp. (S152-S159)
Copyright@ EM International
ISSN 0971–765X

Environmental and Provinance study of Mudflats from Shastri Estuary, Ratnagiri District, Maharashtra using Clay Minerals

S.B. Joshi[1] and D. D. Kulkarni[2]

[1]Department of Geology, Walchand College of Arts & Science, Solapur 413 006, M.S., India
[2]Department of Geology, School of Earth Science, P.A.H Solapur University, Solapur 413 255, M.S., India

(Received 31 July, 2021; Accepted 30 August, 2021)

ABSTRACT

Coastal environment is most active, dynamic and transitional in nature and is characterized by the interplay of continental and marine environments. Estuary represents a most complex environment, developed in the transitional ecotone environment at the confluence point of river and sea. The Konkan Coastal Belt (KCB) of Maharashtra is traversed by eighteen major and thirty-six minor west flowing perennial rivers, originate in the Western Ghats and produce remarkable mud flats along their course. Shastri is one of the most important estuaries of west coast of Maharashtra. During present investigations, sedimentological, clay mineralogical studies of mud-flats from Shastri estuary have been carried with respect to genesis, environmental and provenance using pipette analysis, X-ray diffraction and I-R studies. Representative mud samples have been analyzed. In all samples, the water-soluble salts are found to be negligible in quantity than acid soluble salts. All sediment samples contain significant number of fines with < 63 ìm size. Pipette analysis shows that the sediments from mouth of estuary are of silty- sand type whereas the sediments from middle and upper reach of sandy-silt in nature. X-ray diffraction and I R studies show the presence of kaolinite, goethite, gibbsite, illite, muscovite, chlorite and montmorillonite minerals. The presence of particular clay mineral is due to chemical weathering of the host rock in humid and subtropical conditions. The process of laterization of basalt involves leaching of the most of the oxides from pyroxenes and feldspars. This leaching process is responsible for the formation of different clay minerals in the residual deposit.

Key words: *Environment, Shastri, Clay, X-ray diffraction, Basalt*

Introduction

The West Coast of India (WCI) has attracted the attention of many geo-scientist due to its neo-tectonic set up, continuing seismic activities, sea level changes, marine and estuarine environment as well as due to environmental degradation. The estuarine processes are more complex in tropical environment . According to Karbassi *et al.* (2008), the sediment volume fluctuates with in river-dominated estuaries. The intertidal mudflats are prominent sub-environments found on the fringe of estuaries (O' Brine, *et al.*, 2000). According to Reinecke and Singh, (1980), the mudflats are developed where the wave action is not strong to disturb the fine sediments. Fine sediments of the mud flats are derived from terrestrial as well as marine regions and considerably modified in terms of mineralogy, texture and

([1]Assistant Professor, [2]Assistant Professor)
Corresponding author's email: sanjaybj65@rediffmail.com

chemistry during the journey. (Shi and Chen, 1996). Numbers of Geo-scientists have contributed in relation with the sedimentological studies of the beach sand, Tertiary sediments and shales from different coastal zones of west coast of India. Review of literature shows that there is a scope to carry the sedimentological and mineralogical studies of the estuarine mud-samples in relation to environment of deposition. The Shastri represents one of the major rivers of west coast of Maharashtra. The present work has been attempted to carry out the detailed investigations related to sedimentological and clay mineralogical studies of the estuarine mud-samples of Shastri river Basin (SRB).

Materials and Methods

Study Area

SRB lies along the Western Coastal tract of India in Maharashtra state (lat.16^{0}57′N.; long.73^{0}15′E. and lat. 17^{0}30′N.; long. 73^0 50′ E.) (Fig.1, Fig. 2- Google Image). Shastri is a seventh ordere river having a length of about 72 km., flows in east-west direction It covers an area of about 2098 km^2 (SOI topographic sheet Nos. 47 G/3, G/4, G/7, G/8, G/11, G/12 and 47 H/9). The area falls in a tropical to subtropical humid climate with high rainfall, temperature and humidity. It receives average rainfall of 3000 mm.

Geology

SRB lies along the western periphery of the Deccan

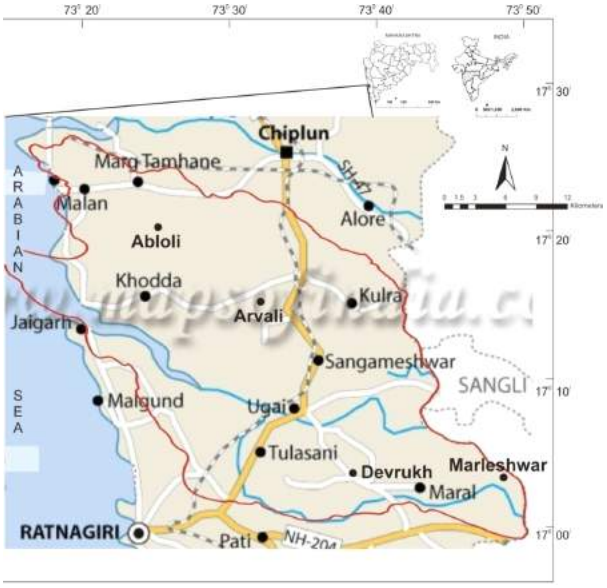

Fig. 1. Location Map of the Area (Shastri River Basin)

Trap province i.e. tholeiitic province of India, represented by basalts of Cretaceous to Eocene age. Deccan basalt lava flows belong to Ambenali and Poladpur formations of Wai sub-group (Mitchell and Cox, 1988), mainly exposed along river valleys, valley sides and near shore. These flows are capped by laterites of Pleistocene age while, the Quaternary sediments are exposed along the banks of Shastri River and its tributaries.

Drainage

Shastri river is characterized by presence of dendritic to sub-dendritic drainage pattern, with trellis and sub parallel at some places. It shows abnormal drainage characters at some places during the course indicating tectonic imprints viz. sharp bends, straight channels and ponding etc. at many places.

Sampling

The inter-tidal mud-flats are prominent in the lower and middle reaches, while poorly developed in the upper reaches of the Shastri estuary. The representative core samples of mud flats up to 10 cm depth were collected from six different localities, covering lower, middle and upper reaches of the estuary to carry the textural, mineralogical studies (Fig. 3). Two core samples of mud were collected near the mouth representing lower reach of the estuary (Tavsal 17^0 18^1 N, 73^0 14^1 E and Saitvada 17^0 15^{1}N, 73^0 15^1 E). Another two samples were collected from the middle part of the estuary (Agarnaral 17^0 12^1 N, 73^0 28^1 E and Phungus 17^0 12^1 N, 73^0 28^1 E)) and remaining two core samples were collected from the upper reaches of river (Sangmeshwar 17^0 11^1 N, 73^0 32^1 E and Phansavane 17 ^{0} 08′ N & 73 ^{0} 40′ E).

Insoluble Residue Analysis

Insoluble residue analysis of representative six samples (20 g) have been carried by following standard methods. The insoluble residue content was computed and results so obtained have been presented in Table 1.

Pipette Analysis

Insoluble residue analysis suggests that significant number of fines having < 63 ìm size are present in sediments. Pipette analysis of these sediments has been carried out (Krumbein and Petti John, 1938; Folk 1974; and Carver, 1971) and weights of various size fractions are calculated. The data so obtained has been presented (Table 2 and Fig. 4a, b and c).

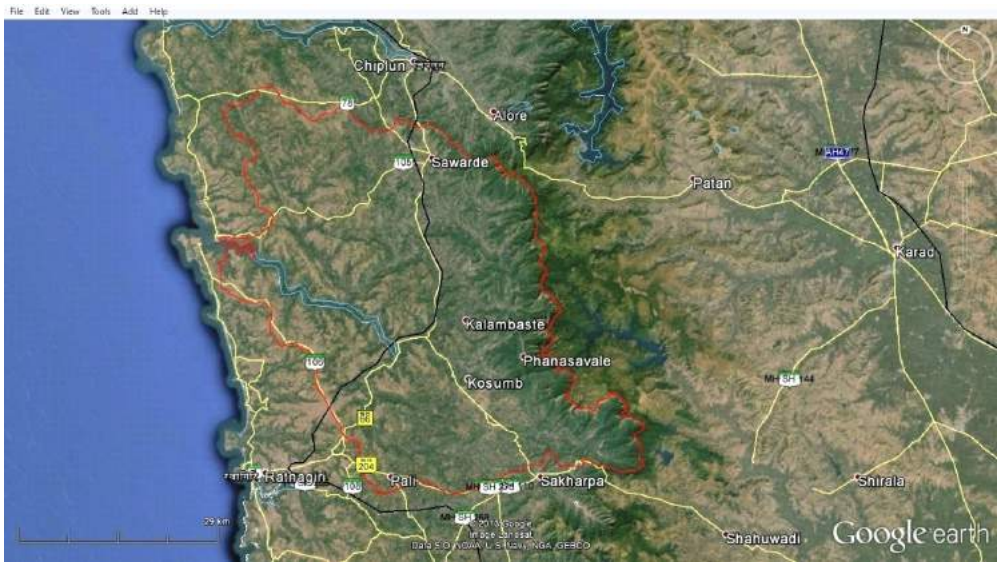

Fig. 2. Map of the SRB (Google Image)

Table 1. Insoluble Residue Content of the Mud Flat Samples from Shastri Estuary

Location	Sample No.	Position of Sample	Insoluble Residue %
Mouth	S1	Top	90.66
Tavsal		Bottom	88.89
Saitvada	S2	Top	91.45
		Bottom	91.88
Middle reach	S3	Top	86.80
Agarnaral		Bottom	89.89
Phungus	S4	Top	91.06
		Bottom	89.37
Upper reach	S5	Top	84.11
Sangmeshwar		Bottom	86.10
Phansavane	S6	Top	87.07
		Bottom	85.06

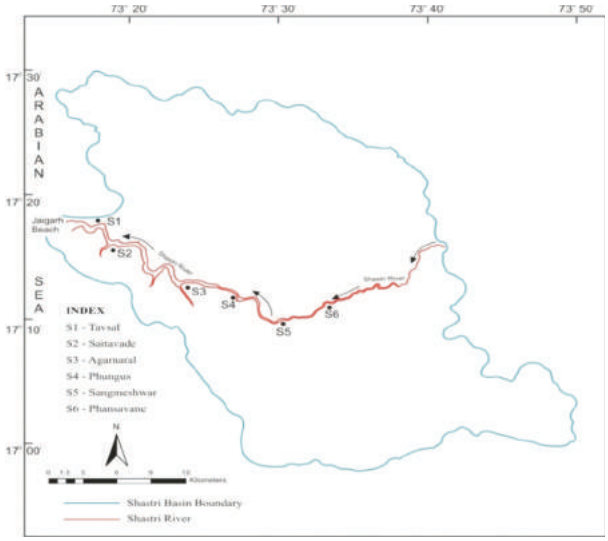

Fig. 3. Sample Location Map (SRB)

The percent size fractions present in each sample worked out as sand, silt and clay. The sand-silt-clay values obtained during pipette analysis have been plotted on the triangular diagram (Folk, 1980) (Fig. 5).

Clay Mineral Studies

Mud flats containing varieties of clay minerals are exposed at the mouth and along the Shastri estuary. The composition of clay depends mainly on the chemical composition of the parent minerals and physico-chemical environment under which the alteration takes place. The source and environment of deposition are important controlling factors of the clay mineralogy and their distribution (Grim, 1958). To understand these aspects, clay mineral studies of Shastri estuary is carried by following X-ray and Infra-Red Spectroscopic techniques.

X-Ray Diffraction Studies

The clay fractions of all six samples were examined and identified by using X-ray diffraction technique. The study has been carried out on a Phillip – 1710 X-ray diffractometer. The diffractograms were scanned within a range from 5^0 to 60^0 with a step width 0.02 and at speed of 2^0 per minute. The X-ray diffractograms for all mud samples are interpreted

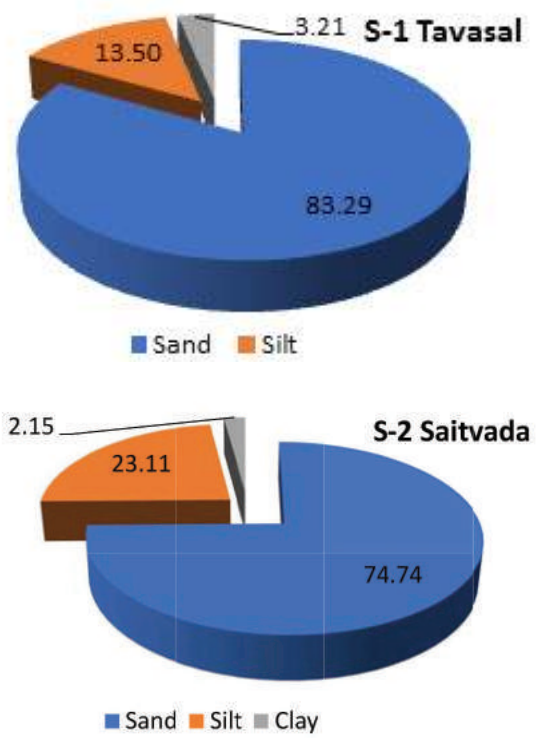

Fig. 4a. Grain Size Fractions (Sand – Silt – Clay) in Mudflat from Shastri Estuary (Lower Reach)

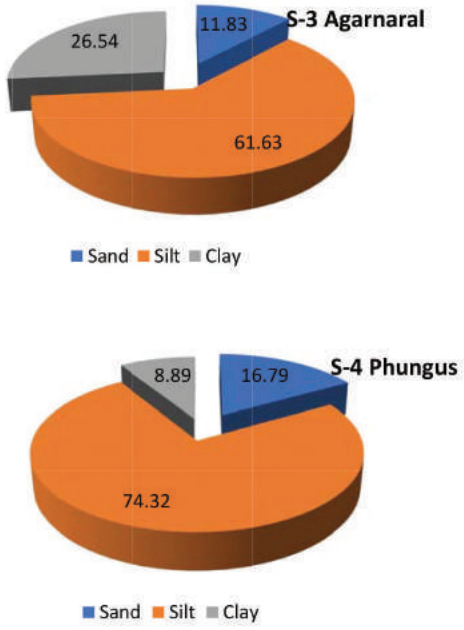

Fig. 4b. Grain Size Fractions (Sand – Silt – Clay) in Mudflat from Shastri Estuary (Middle Reach)

Table 2. Weight Percent of Sand, Slit and Clay of Mud Samples from Shastri Estuary

Sample No.	Sand	Slit	Clay
Mouth			
S–1 – Tavsal	83.29	13.50	3.21
S–2 – Saitavada	74.74	23.11	2.15
Middle Reach			
S–3 – Agarnaral	11.83	61.63	26.54
S–4 – Phungus	16.79	74.32	8.89
Upper Reach			
S–5 – Sangmeshwar	23.11	58.99	17.10
S–6 – Phansavane	21.77	60.52	17.71

Table 3. Semi-Quantitative abundances of clay minerals from X-Ray studies for mudflat samples of Shastri Estuary

Sample No.	Kaolinite	Goethite	Chlorite	Illite	Muscovite	Gibbsite	Montmorillonite
S-1	71.62	3.13	25.25	-	-	-	-
S-2	22.47	2.02	19.63	31.41	24.47	-	-
S-3	15.66	3.18	-	59.71	-	17.54	3.91
S-4	50.29	1.79	6.81	9.11	29.36	2.64	-
S-5	10.23	1.73	23.16	18.22	22.22	3.77	20.67
S-6	9.99	-	23.24	18.25	22.20	5.72	20.60
Mean	30.04	1.98	19.62	27.34	24.56	7.42	15.06

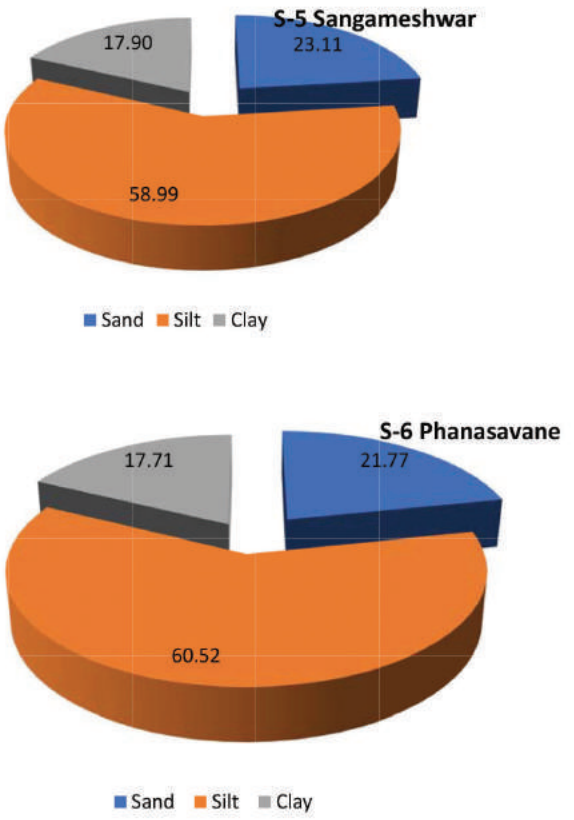

Fig. 4c. Grain Size Fractions (Sand – Silt – Clay) in Mudflat from Shastri Estuary (Upper Reach)

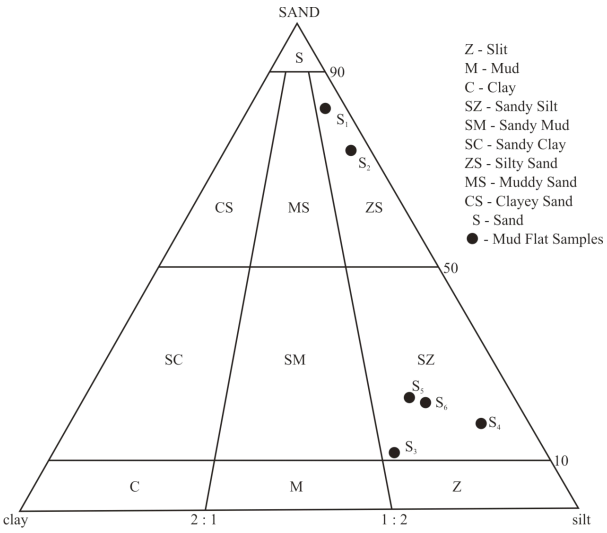

Fig. 5. Triangular Diagram Showing Classification of Mudflat (sand-silt-clay) samples from Shastri Estuary

(Fig. 6a, b and c) and clay mineral assemblages identified (Table 3).

Infrared Spectroscopic Studies

I. R. spectroscopic study of these mud samples was also carried. IR spectra for all six samples were obtained on a Perkin-Elmer model 783 Infra-Red spectrophotometer and interpreted (Fig. 7a, b and c) for mineral content (Table 4).

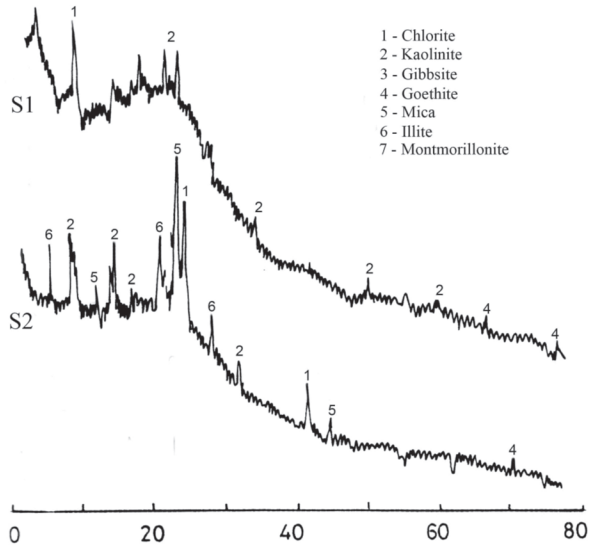

Fig. 6a. X-Ray Diffractograms of Mud Samples of Shastri Estuary (Lower reach)

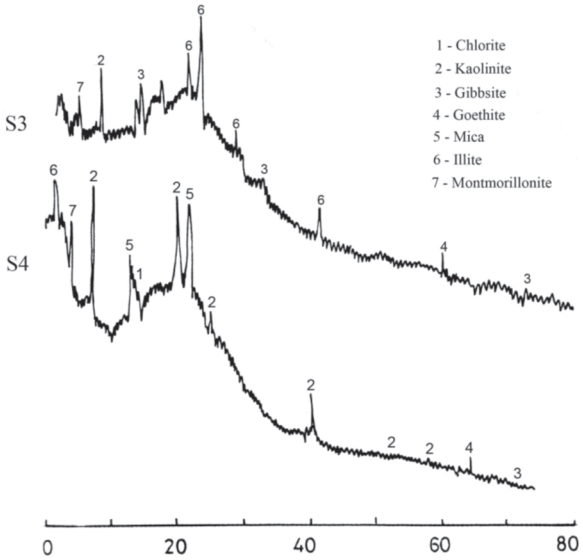

Fig. 6b. X-Ray Diffractograms of Mud Samples of Shastri Estuary (Middle reach)

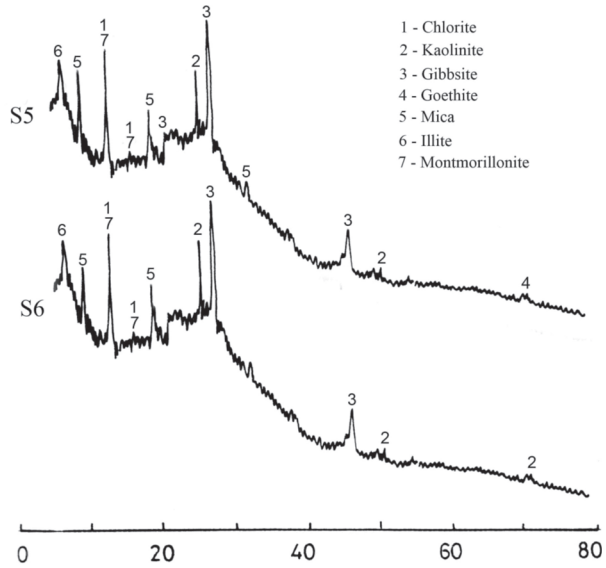

Fig. 6c. X-Ray Diffractograms of Mud Samples of Shastri Estuary (Upper reach)

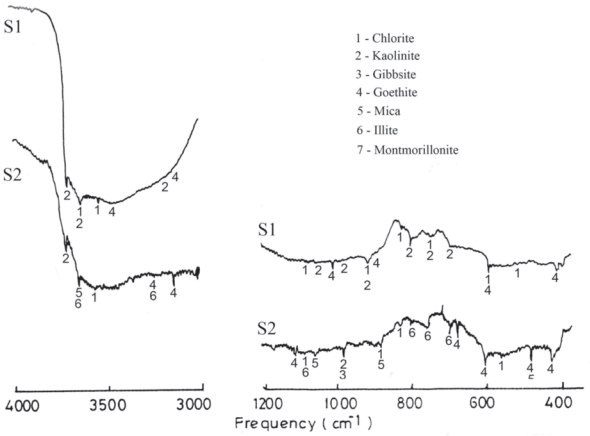

Fig. 7a. Infra-Red Spectra of Mud Samples Shastri Estuary (Lower reach)

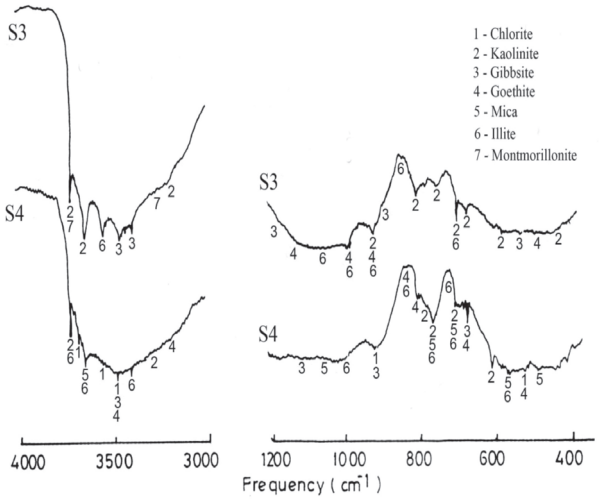

Fig. 7b. Infra-Red Spectra of Mud Samples Shastri Estuary (Middle reach)

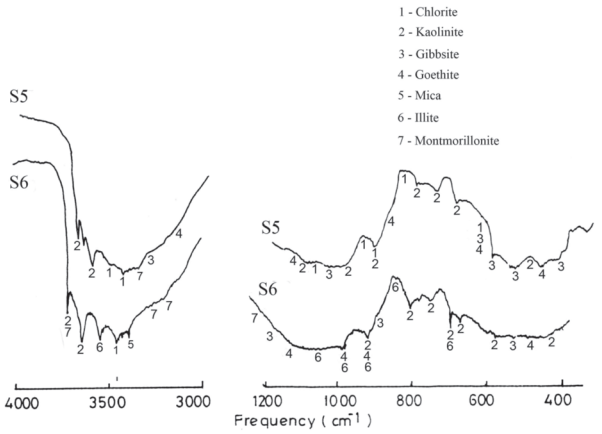

Fig. 7c. Infra-Red Spectra of Mud Samples Shastri Estuary (Upper reach)

Conclusion and Discussion

From the insoluble residue analysis, it has been observed that water-soluble salts are negligible in

Table 4. Clay mineral assemblages interred from X.R.D. and I.R. for mudflat samples of Shastri Estuary

Sample No.	X.R.D.	I.R.
S-1	Kaolinite, Goethite, Chlorite	Kaolinite, Goethite, Chlorite
S-2	Kaolinite, Goethite, Chlorite, Illite, Muscovite	Kaolinite, Goethite, Chlorite, Illite, Muscovite
S-3	Kaolinite, Goethite, Illite, Gibbsite, Montmorillonite	Kaolinite, Goethite, Illite, Gibbsite, Montmorillonite
S-4	Kaolinite, Goethite, Illite, Muscovite, Gibbsite	Kaolinite, Goethite, Illite, Muscovite,
S-5	Kaolinite, Goethite, Chlorite, Muscovite, Gibbsite, Montmorillonite	Kaolinite, Goethite, Chlorite, Muscovite, Gibbsite, Montmorillonite
S-6	Kaolinite, Chlorite, Illite, Muscovite, Gibbsite, Montmorillonite	Kaolinite, Chlorite, Illite, Muscovite, Gibbsite, Montmorillonite

quantity than acid soluble salts in all samples. The low content might be due to the absence of biological activities at the time of deposition of these sediments while, the presence of acid soluble fractions might be due to deposition of carbonates during post depositional phase.

Significant number of fines with < 63 ìm size are present in sediments. From the grain size analysis, it has been observed that the percentage of coarser fraction is maximum in the samples from lower reaches, near the mouth of the estuary. It might be due to active hydrodynamic conditions facilitating the deposition of sand fractions near the mouth. Presence of finer fractions are maximum in the middle reaches, might be due to the release of the fine sediments by tributaries in the Shastri river. From the plots on triangular diagram, the sediments from mouth of estuary can be classified as silty-sand whereas the sediments from middle and upper reach can be classified as sandy-silt.

The X-ray diffraction and IR Spectroscopic studies show presence of clay minerals like kaolinite, montmorillonite, illite along with muscovite, chlorite, goethite, gibbsite minerals. Presence of particular clay mineral is an indication of the degree and extent of chemical weathering of the host rock i.e., basalt under humid and subtropical conditions (Suryavanshi, *et al.,* 2014) The process of laterization of basalt involves leaching of the most of the oxides from pyroxenes and feldspars. It seems that leaching process is responsible for the formation of clay minerals in the residual deposit. It is a primary environment in the area in which the clay minerals are formed. These clay minerals might have transported from laterites through lithomarge clay to the mud flats and deposited along the banks of estuarine mouth and hinterland zones, representing a secondary environment.

According to Biscay, (1965), the formation and presence of kaolinite in the mudflats takes place due to intense chemical weathering of the plagioclase feldspars from the basaltic soils developed under heavy rainfall, good drainage and acidic water. In marine environment, kaolinite concentrates near the shore (Keller, 1970). Kaolinite is weathering product of feldspar and other silicates, produced by ion stripping in power pH environment. (Saha, *et al.,* 2020) Presence of kaolinite in the mudflat of Shastri might be due to its deposition under estuarine environment.

Presence of illite from transitional environment along estuaries of Maharashtra coast have been reported by Pandian and Sukhtankar (1991). Kaolinite, when subjected to subsequent digenesis during burial of sediments, gives rise to illite + chlorite (Velde, (1968). When fluvial system discharges kaolinite into ocean, it probably begins to dissolve under the influence of marine environment with the formation of illite (Keller, 1970)

Montmorillonite clay also shows its genesis in the primary environment like that of kaolinite, from laterite and lithomarge clay. It might have been transported through the major stream at the time of deposition. It is formed due to intense chemical weathering of volcanic material (Keller, 1970). According to Kenett, (1982), formation of montmorillonite takes place from the basaltic flows or from laterites. Its abundance depends on the hydraulic conditions of the estuarine environment (Grim, 1968). Along the Shastri estuary, presence of higher percentage of kaolinite as compared to montmorillonite might be due to the estuarine environment.

Presence of Gibbsite in the mud flats indicate its formation by breaking away of the feldspars from basalt (Khanadal and Devraju, 1987). It might also be formed due to chemical weathering of kaolinite. With the increasing degree of leaching, kaolinite gets transferred to gibbsite by a hydrolysis process (Jackson, 1959; Velde, 1985). The presence of kaolinite, gibbsite along with goethite indicate their formation under intense chemical weathering of pyroxene i.e. augite present in the Deccan basalts (Sahastrabudhe, 1989).

Chlorite and muscovite minerals are reported in less number in mud flats of the Shastri estuary. Formation of chlorite might be due to digenetic alteration of kaolinite or gibbsite.

Muscovite is flaky in habit and has relatively less specific gravity. It can easily migrate through medium of water. It might have formed by the hydrothermal alteration of pyroxenes present in the Deccan basalts or due to longshore transport, being derived from the Precambrian terrain, exposed in the southern part of the study area.

Acknowledgement

Dr. S. B. Joshi express sincere thanks to Dr. V. S. Koti, Principal, Walchand college of Arts & Science, Solapur for his continuous encouragement and help extended during present work.

References

Biscay, P. E. 1965. Mineralogy and sedimentation of recent deep-sea clay in the Atlantic Ocean and adjacent seas and oceans. *Bull. Geo. Soc. Amer*. 76 : 803-832.

Folk, R. L. 1980. *Petrology of Sedimentary Rocks. Austin Texas.* USA, Hemphill Pub. Co. II Edi. pp. 184

Grim, R. E. 1958. Concept of digenesis in Argillaceous sediments. *Bul. Ame. Asso. Petr. Geol.* 42, : 246-253.

Grim, R. E. 1968. *Clay Mineralogy, McGraw Hill book Co.* New York, pp. 126-164

Jackson, M. L. 1959. Frequency distribution of clay minerals in major soil groups as related to factors of soil formation. Clay Min. 6, : 133-143.

Karbassi, A. R., Monavari, S. M. Bidhendi, G.R. N. Nouri, J. and Nematpour, K. 2008. Metal pollution assessment of sediment and water in the Shur River. *Env. Monitor Asses.* 147 (1-3) : 107-116.

Keller, W. D. 1970. Environmental aspects of clay minerals, Jour. *Sed. Pet.* 40 : 788-813.

Kenett, J. 1982. *Marine Geology*, Prentice Hill Inc. Eaglewood. Cliffs. N.J. 07632, pp. 752

Khandal, S.D. and Devraju, T.C. 1987. Laterite-bauxite of Paduvari plateau, South Kanara, Karnataka state. *Geol. Soc. Ind.* 30 (4) : 225-266

Mitchel, C. and Cox, K.G. 1988., A Geological sketch map of southern part of Deccan Province, Memoir of *Geological Soc. of India*. 10 : 27-33

O' Brian, D.J., Whitehouse, R.J. and Cramp, A. 2000. The cyclic development of macrotidal mudflats on varying time scale Cont. *Shelf Res.* 20 : 1593-1620.

Pandian, R.S. and Sukhtankar, R.K. 1991. Clay mineralogical studies of mudflats Agashi and Bassein creeks, Dist. Thane, Maharashtra. *Proc. Quat. Landscape of Indian sub-continent*, Geo. Dep. M.S. U. Baroda, pp. 94-106.

Reineck, H.E. and Singh, I. B. 1980. *Depositional Sedimentary Environment.* Springer-Verlag Pub. Pp. 549

Saha, S., Syed, S.A., Munir, H. and Roy, M.K. 2020. Study of Clay Minerals of the Sediments of the Jayanti Estuary, Shariatpur-Barisal, Bangladesh. *International Journal of Recent Research and Applied Studies.* 7 4 (2): 6-14

Sahasrabudhe, K.S. 1989. Coastal laterites of M.S. Proc. Tertiary and recent sedimentation along west coast between Bombay and Ratnagiri, Dept. of Geology, N. Wadia college, Pune

Shi, Z. and Chen, P.Y. 1996. Morpho-dynamics and sediment dynamics on inter tidal mud-flats in China. *Cont. Shelf Res.* 16 (15) : 1909-1926.

Suryavanshi, R. A., Sawant, P. T. and Kolekar, R. B. 2014. Clay Mineral Study in Tertiary Sediments from Bhatia and Jaigarh Creek, Ratnagiri, M.S. (India). *Int. Journal of Advances in Earth Sciences.* 3 (2) : 52-60

Velde, B. 1968. Effects of chemical reduction on stability of Pyrophyllite and Kaoline in phyllitic rocks. *Jour. Sed. Pet.* 38 : 13-16.

Velde, B. 1985. Clay minerals: A physic-chemical explanation of their occurrence. Elsevier pub. Pp. 427

Nature Environment and Pollution Technology
An International Quarterly Scientific Journal

p-ISSN: 0972-6268
(Print copies up to 2016)
e-ISSN: 2395-3454

Vol. 21 | No. 1 | pp. 000-000 | 2022

Original Research Paper

https://doi.org/10.46488/NEPT.2022.v21i01.000

Open Access Journal

Use of Remote Sensing and GIS Techniques in Identification of Landslide Vulnerable Zones of Shastri River Basin, Along the West Coast of Ratnagiri District, Maharashtra

S. B. Joshi *† and D. D. Kulkarni**
*Department of Geology, Walchand College of Arts & Science, Solapur, Maharashtra, India
**Department of Geology, School of Earth Sciences, P.A.H. Solapur University, Maharashtra, India
†Corresponding author: S. B. Joshi;

Nat. Env. & Poll. Tech.
Website: www.neptjournal.com

Received: 08-06-2021
Revised: 00-00-2021
Accepted: 14-07-2021

Key Words:
Natural hazards, Remote sensing, DEM, GIS, Landslide

ABSTRACT

The atmosphere, hydrosphere, and lithosphere are subjected to different processes, leading to natural hazards like weathering, erosion, floods, cyclones, landslides, earthquakes, tectonic movements, etc. Environmental degradation is a serious aspect of the recent past, mainly due to natural and manmade interactions. The pressure for infrastructure development due to rapid urbanization has led to the expansion of construction activities. It has catapulted the frequency of landslides to dramatic proportions in recent decades, especially along western ghats. The West Coast of India (WCI) has attracted the attention of Geo-scientists due to its neo-tectonic setup, continuing seismic activities, sea-level changes, and also due to environmental degradation. It is followed that very limited attempts have been made related to the land sliding along the west coast tract of Maharashtra. The present investigations are emphasized mainly to locate the landslide vulnerable zones of Shastri River Basin (SRB), Ratnagiri district of Maharashtra by using remote sensing data, GIS techniques along field studies. The area lies within a triple junction of Koyana-Kurduwadi Lineament (KKL), West Coast Fault (WCF), and Panvel Flexure (PF). Based on the integration of data from various thematic maps viz. lithology, lineaments, slope, geomorphology, land use-land cover along with inventory map, Landslide Vulnerable Map (LVM) of the SRB has been prepared. It follows that about 29% area of the SRB forms a highly vulnerable zone for land sliding. These zones are mainly confined to steep slopes, wasteland, highly weathered basalts, and deep valleys and in the vicinity of lineaments.

INTRODUCTION

Land degradation is one of the serious environmental problems, causing due to the demand for natural resources by the growing population for food, fodder, fuelwood, and intensive industrial as well as anthropogenic activities. The key problems of land degradation are desertification, deforestation, soil erosion, waterlogging, salination, economic pressure, and poverty. Due to natural and manmade interactions, the atmosphere, hydrosphere, and lithosphere are subjected to different processes, leading to natural hazards. Natural hazards and disasters continue to have an increasing impact on humans around the world. However, studies show that this impact is heavily tilted towards developing countries like India, which might be due to the increasing population. Amongst all the natural disasters, landslides severely damage infrastructure, cause a loss of life and properties, and impact the daily life of people living in the affected regions (Juang et al. 2019). The pressure for infrastructure development due to rapid urbanization has led to the expansion of construction activities. It has accelerated the frequency of landslides to dramatic proportions in recent decades, especially in hilly terrains.

The studies carried out by many scholars have indicated that the various geosystems viz. lithology, lineaments, geomorphology, slope, land use/land cover, etc. occurring in different combinations, assign differing landslide vulnerability grades (Nagarajan et al. 1998, Guzzetti et al. 2012, Meena et al. 2019, Prakash et al. 2020, Edison & Ganpati 2020). Ramakrishnan et al. (2002) prepared thematic layers in a GIS platform using aerial photos and orthophotos. Heavy rainfall is a critical factor in triggering landslides as it generates a rapid increase in pore pressure in the vadose zone and groundwater flow in the saturated area (Jiu et al. 2005). Various geological structures along with lineaments and lithology play a vital role in triggering landslides (Greenbaum et al. 1995). The susceptibility of the slopes for landslides can also be influenced by land-use and landcover changes caused due to natural or manmade activities (Diaz et al. 2005). According to Van Westen et al.

(2006), the soil also acts as one of the most sensitive parameters of land sliding.

The pre- and post-disaster landslide studies have been carried out by many governments and semi-government agencies, academic institutions viz. GSI, CBRI, CRRI, NRSA, WIHG, DTRL, Govind Ballabh Pant Institute of Himalayan Environment, IIT-Roorkee, etc. These organizations have carried work mostly related to landslide-prone regions of the parts of the Himalayas, Uttarakhand, and most of the North-Eastern parts of India. However, very limited attempts have been made with respect to land sliding along Western escarpments of India, especially the west coast of Maharashtra. Therefore, the present studies have been envisaged to locate the landslide-prone zones present within the Shastri River Basin (SRB), Ratnagiri district of Maharashtra. The SRB lies within a triple junction of Koyana- Kurduwadi Lineament (KKL), West Coast Fault (WCF), and Panvel Flexure (PF). It forms a part of one of the seismically active regions of the Indian continent (Valdiya 2011), characterized by sloping topography, presence of shear zones, accelerating rain-splash erosion, sheet erosion as well as gully erosion.

Study Area

The area lies along the West Coast of Maharashtra (India) (lat.$16^0$57'N.; long.$73^0$15'E. and lat. 17°30'N.; long. 73° 50' E.) (Figs. 1 and 2). Shastri is a seventh-ordered river having a length of about 72 km. It flows from NE to SW direction following major trends of the lineaments and covers an area of about 2098 km^2 (SOI topographic sheet Nos. 47 G/3, G/4, G/7, G/8, G/11, G/12, and 47 H/9). The SRB forms a part of the western periphery of the Deccan Trap province of India. It represents the presence of basaltic lava flows of Cretaceous to Eocene age (Mitchell & Cox 1988), exposed along river valleys, valley sides, and near shore. Most of these are capped by laterites of the Pleistocene age. The drainage pattern is dendritic to sub-dendritic, with trellis and sub-parallel at some places controlled by lineaments.

Fig. 1: Location map of the area (Shastri River Basin).

OBJECTIVES

The main objectives of the present study of SRB are to

- Investigate the causative factors of landslides
- Prepare various thematic maps of these factors viz. slope, geology, lineament, geomorphology, land use/ land cover, etc.
- Prepare a map of the landslide vulnerable zones of SRB

MATERIALS AND METHODS

Present investigations have been carried through the following stages (Fig. 3).

Pre-field studies: These include the review of literature related to landslides, collection of data from topographic sheets, and remote sensing data

Field studies: These include identification of landslides in the field; a collection of their coordinates using GPS, a collection of attributes and training data (GCP) for supervised classification of remote sensing data, and identification of

Fig. 2: Map of the SRB (Google Image).

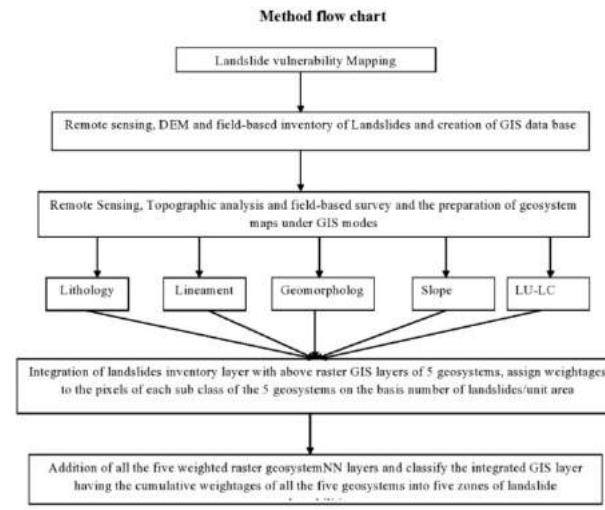

Fig. 3: Method flow chart.

Table 1: Distribution and the morphology of the existing landslides in SRB.

Location No.	L. S. – 1	L. S. – 2	L. S. – 3	L. S. – 4	L. S. – 5	L. S. – 6	L. S. – 7	L. S. – 8
Location	Bhatgaon	Bhatgaon	Near Ukshi village	Close to Konkan Railway line	Karjuve Bridge	Near Bhatgaon village	Near Bhatgaon village	Near Bhuiwadi village
Road Status	Bhatgaon-Abloli Road	Bhatgaon-Abloli Road	Jaigarh-Ukshi Road	Phungus-Sangmeshwar Road	Phungus-Sangmeshwar Road	Bhatgaon-Asore Road	Bhatgaon-Asore Road	Narsinge-Bhuiwadi Road
Lat. And Long.	17°18'20", 73°21'33"	17°17'54", 73°21'45"	17°06'35", 73°26'30"	17°09'55", 73°29'29"	17°11'15", 73°28'22"	17°12'26", 73°25'00"	17°11'46", 73°25'10"	17°12'40", 73°24'00"
Altitude	220 m	120 m	210 m	100 m	100 m	140 m	180 m	200 m
Nature of Slope	Naturally Moderately Steep	Naturally Moderately Steep	Naturally Moderate Top cut Slope	Naturally Moderate Top cut Slope	Natural Top cut Slope	Naturally Moderate Top Cut Slope	Naturally Top cut Slope (Hill Side)	Naturally Steep Top Cut Slope
Strike Dir. of Hill	NNW-SSE	NNW-SSE	N-S	NNE-SSW	NNE -SSW	NNW-SSE	N-S	N-S
Rock Type	Highly altered Deccan Basalt	Lateritic rock mass	Highly Jointed Deccan Basalt	Lateritic soil	Highly altered Laterite	Highly weathered, porphyritic Basalt	Highly weathered Lateritic Soil	Weathered Basalt
Soil Type	Fine Yellowish to Brown, 3 m thick	Dark Brown, 1 m thick	Light yellow thin < 0.5 m	Deep red, Depth couldn't ascertain	Dark brown Lateritic Soil, upto 4 m thick	Brown, thin < 0.5 m	Brown, thin 2 -5 m	Brown, 4 -5 m thick
Type of L. S.	Debris Slide	Minor Slump	Rock Fall	Soil slump	Soil Slump	Rock Slide	Soil Slump	Soil Slump
L. S. Dimensions	Ht. of Crown ≈ 10 m, Width≈ 4 m	Ht. of Crown ≈ 3.5 m, Width≈ 7 m	Ht. of Crown ≈ 2 -4 m, Width≈ 60 m	Ht. of Crown ≈ 2.5 m, Width≈ 70 m	Ht. of Crown ≈ 4 m, Width≈ 52 m	Ht. of Crown ≈ 6 m, Width≈ 85 m	Ht. of Crown ≈ 3 m, Width≈ 40 m	Ht. of Crown ≈ 4 m, Width≈ 25 m

Location No.	L. S. – 9	L. S. – 10	L. S. – 11	L. S. – 13	L. S. – 14	L. S. – 15
Location	Near Bhuiwadi village	Near Bhuiwadi village	Near Dhamnase village	Near Kondye village	Near Chavanwadi village	Near Nayari village (Hilltop)
Road Status	Chaphe – Agarnaral - Bhiwandi Road	Khalgaon – Bhuiwadi Road	Ratnagiri - Ganpatipule Road	Close to Sangmeshwar - Ratnagiri Road	Devrukh – Sangmeshwar Road	Nayari – Sangmeshwar Road
Lat. and Long.	17°13'14", 73°20'15"	17°12'48", 73°23'21"	17°07'55", 73°19'31"	17°10'11", 73°27'35"	17°07'04", 73°32'32"	17°12'55", 73°39'11"
Altitude	200 m	180 m	160 m	200 m	200 m	300 m
Nature of Slope	Naturally Small cut Slope	Natural Moderate Top Cut Slope	Natural Top cut Slope (Hillside)	Naturally Moderate cut Slope	Natural Moderately cut Slope (Hillside)	Natural Steep Slope
Strike Dir. Of Hill	N-S	NE-SW	NW-SE	N-S	NNE-SSW	N-S
Rock Type	Deccan Basalt with 3 sets of joints	Soil with Colluvial Material	Lateritic Blocks	Laterite, Jointed Basalt at Base	Laterite	Poorly jointed Basalt
Soil Type	Dark Brown, 1.5 m thick	Lateritic Red, 4-5 m thick	Lateritic Red Soil	Red Lateritic, 3 m Thick	Red, 5 m thick	Yellow, Murum, < 0.5 m thick
Type of L. S.	Rock Fall	Debris Fall	Soil Creep	Debris Slide	Moderate Soil Slump	Debris Fall, Cracks to ground
L. S. Dimensions	Ht. of Crown ≈ 3.5 m, Width ≈ 25 m	Ht. of Crown ≈ 9 m, Width ≈ 15 m	Ht. of Crown ≈ 3 -4 m, Width ≈ 9 m	Ht. of Crown ≈ 5 m, Width ≈ 50 m	Ht. of Crown ≈ 8 m, Width ≈ 60 m	Ht. of Crown ≈ 10 m, Width ≈ 25 m

various types of anthropogenic activities in the study region. The GPS data is also collected for the ground truth, validation, and accuracy assessment of multispectral and elevation data.

Post-field studies: Post-field study was carried out after preparing thematic maps for validation and accuracy assessment of LVZ using techniques such as Geo-referencing of maps and images; digitization of topographic maps; supervised classification of remote sensing data; generation of Digital Elevation Model (DEM); preparation of various thematic maps viz. slope, geological, lineament, land use/landcover, etc. and preparation of final Landslide Vulnerable Zone (LVZ) map of SRB using ArcGIS techniques.

Data Used

For the comprehensive study and to achieve more accurate results, following types of data have been used.

- Topographic sheets of 1:50000 scale to create GIS-based vector layers
- IRS-R2 LISS III remote sensing data for temporal and spatial changes and also to prepare various thematic maps in raster format
- Digital Elevated Model (DEM) (Fig. 4)
- Rainfall data from GSDA, Ratnagiri, Govt. of Maharashtra
- IDRISI 3 software for image raster analysis and Arc GIS software for vector analysis.

Attempts have been made to generate a landslide vulnerability map for the study area using a GIS-based geosystem response model.

Location and Characters of Existing Landslides

In the first step, distribution and the morphology of the existing landslides observed during the field inventories with GPS and data have been presented in (Table 1). The preliminary inventory map has been prepared (Fig. 5).

Generation of GIS Databases on Geosystem Parameters

Then vector GIS databases showing the features (in the form of polygons) were generated for various geological parameters viz. lithology, lineaments, geomorphology, slope, land use /land cover, etc. which only dominantly assign the landslide vulnerability grades to the area. These five vector GIS layers were converted into raster layers using ArcGIS (Figs. 6, 7, 8, 9, and 10). Over these five raster GIS layers, the landslide distribution map (Fig. 5) was independently overlaid using Arc GIS software. Based on the number of landslides falling in each subclass of the five geosystem layers, landslides per unit area (weightage) were worked out. This was obtained by dividing the number of landslides falling in each subclass by the total number of pixels of the corresponding subclass. Thus, the weightages were assigned to each subclass or the polygon class of all the five geosystem GIS layers. The data is given in respective tables. The weightage was also assigned to road frequencies.

Table 2: Landslide vulnerability weightages of various classes of lithology (SRB).

Sr. No.	Lithology	No. of Landslides (LS)	Area or No. of Pixel (A)	(LS /A)	LV weightage (LS/A) × 1000
1	Laterite	15	12070	0.0012428	1.24
2	Alluvium	0	169	0	0
3	Purandargadh weathered basalt	10	6773	0.0014765	1.48
4	Diveghat	9	16221	0.0005548	0.55
5	Shastri River	5	1882	0.0026567	2.66

Table 3: Landslide vulnerability weightages of various classes of lineaments (SRB).

Sr. No.	Lineament Buffer	No. of Landslides (LS)	Area or No. of Pixel (A)	(LS /A)	LV weightage (LS/A) × 1000
1	400	23	11555	0.0019905	1.99
2	800	10	10671	0.0009371	0.94
3	1200	4	7696	0.0005198	0.52
4	1600	1	4765	0.0002099	0.21
5	2000	0	3051	0	0

Table 4: Landslide vulnerability weightages of various classes of geomorphology (SRB).

Sr. No.	Geomorphology	No. of Landslides (LS)	Area or No. of Pixel (A)	(LS /A)	LV weightage (LS/A) × 1000
1	Deep Valley	14	658663	0.000021	0.0212
2	Shallow Valley	4	400006	0.000009	0.0099
3	Plain	1	150126	0.000006	0.0066
4	Slope	12	43833	0.000274	0.2737
5	Ridges	8	766442	0.000010	0.0104

Table 5: Landslide vulnerability weightages of various classes of slope (SRB).

Sr. No.	Slope	No. of Landslides (LS)	Area or No. of Pixel (A)	(LS /A)	LV weightage (LS/A) × 1000
1	Gentle (0°-5°)	1	686389	0.00000	0.0014
2	Moderate (6°-10°)	4	596648	0.00001	0.0067
3	Steep (11°-20°)	33	709059	0.00005	0.0465
4	Very Steep (21°-35°)	1	29376	0.00003	0.0340
5	Precipitous (>35°)	0	4553	0.00000	0

These weighted raster GIS layers were then added using the raster calculator menu of Arc GIS software and thus the final integrated GIS layer was generated with each pixel having the cumulative weightage of all the GIS geosystem layers. Finally, based on the dynamic range of the weightages of the final integrated GIS layer, the study area (SRB) was classified into 5 Landslide vulnerable zones viz. very high, high, moderate, low, and very low (Fig. 11). Details of various steps are discussed in the following paragraphs.

Lithology: SRB is predominantly covered by Deccan Basalts. It has undergone different degrees of weathering. The area has been studied by using tonal difference, drainage density, vegetal coverage from the satellite data and subsequently followed by the field checks. Litho-logically the area is classified into different categories viz. highly weathered, weathered, moderately weathered, poorly weathered, and un-weathered. The zones covered by these classes were digitized into five polygon classes using the screen digitization technique by Arc-GIS. The GIS layer was generated by the conversion of vector to raster form for the lithological studies (Fig. 6).

Lineament density: Based on the tonal, textural, topographical, drainage, and vegetation linearities and curvi-linearities, the fracture-controlled lineaments were observed in IRS- R2 LISS III raw, FCC data, and DEM data. It was mapped and checked in the fields. The buffering technique was adapted to understand the influence of lineaments. For this purpose, five buffer zone classes were marked viz. 400 m, 800 m, 1200

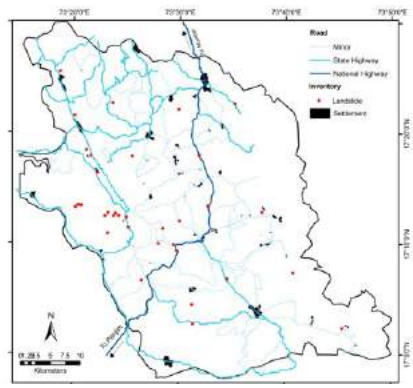

Fig. 5: Landslide inventory and road map of SRB.

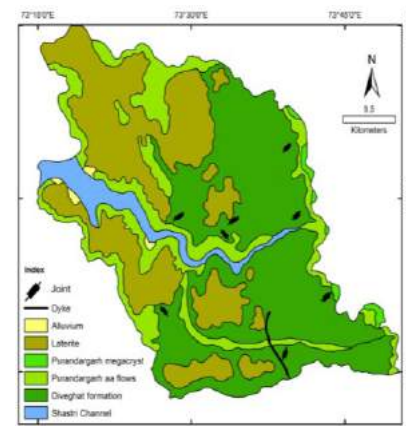

Fig. 6: Lithological map of SRB.

Table 6: Landslide vulnerability weightages of various classes of LULC (SRB).

Sr. No.	LULC	No. of Landslides (LS)	Area or No. of Pixel (A)	(LS /A)	LV weightage (LS/A) × 1000
1	Grassy land	23	117890	0.0001951	0.1951
2	Water	0	24393	0	0
3	Barren (Laterite)	6	431900	0.0001389	0.0139
4	Forest	9	528741	0.0001722	0.0170
5	Agriculture	1	475596	0.0002103	0.0021

Table 7: Landslide vulnerability weightages of various classes of roads (SRB).

Sr. No.	Distance	No. of Landslides (LS)	Area or No. of Pixel (A)	(LS /A)	LV weightage (LS/A) × 1000
1	50	7	1854	0.00377562	3.7756
2	100	4	1731	0.002310803	2.3108
3	150	1	1656	0.000603865	0.6039
4	200	1	1586	0.000630517	0.6305
5	250	8	1546	0.005174644	5.1746

m, 1600 m, and 2000 m. The GIS database in the form of a raster layer was generated using these five classes with the help of ARC-GIS (Fig. 7).

Geomorphology: For geomorphic studies, the IRS R2 LISS – III data was subjected to various image processing techniques, like contrast stretching, false-color composites, color composites of principal component images, etc. Various geomorphic features considered for the landslide studies viz. deep valleys, plains, ridges, shallow valleys and slopes, etc. along with vegetation were interpreted and vectorized as individual polygon classes. The GIS database was generated by the conversion of the data into the raster layer (Fig. 8).

Slope: To understand the landslide vulnerability zones, the slopes were classified into five categories viz. precipitous (> 35^0), very steep (35^0– 21^0), steep (11^0– 20^0), moderate (6^0– 10^0), and gentle (0^0– 5^0) (Wentworth, C. K., 1930). The vector GIS layer was generated for these zones showing five polygon classes of slopes and then converted into a raster layer (Fig. 9).

Land use/Land cover: This parameter provides varying degrees of protection and vulnerability to landslides. The natural vegetation and the thick forests anchor the soils and protect the slopes from slope failures, while, the plantations, settlements, highly developed areas with a network of roads, increase the probability of the occurrence of landslides. For this study, the digitally processed IRS R2 LISS –III data were used. The features viz. water bodies, agriculture, forests, built-up, and wasteland were interpreted. They were

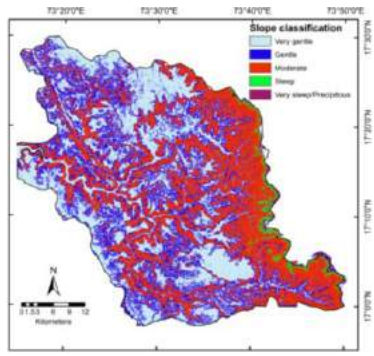

Fig. 9: Slope map of SRB.

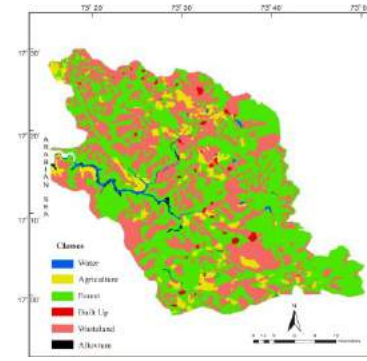

Fig. 10: Land use/Landcover Map of SRB.

Table 8: Distribution of landslide vulnerable zones (SRB).

Sr. No.	Class	Area or No. of Pixel (A)	Percentage of Area
1	Very High	12212	28.20
2	High	422	0.98
3	Moderate	10274	23.73
4	Low	11331	26.17
5	Very Low	9058	20.92

digitized and a vector GIS layer was generated showing all the features as different polygon classes (Fig. 10).

Assigning Landslide Vulnerability Weightages to Geosystem Parameters

Generation of raster GIS layers is followed by the assignment of the landslide vulnerability weightages to each feature class of all the five geosystem layers, based on the number of landslides per unit area. These are raster layers and hence the polygon classes are referred to as the feature classes. The same procedure is done by overlaying the GIS layer of landslides inventory map (Fig. 5) over the above five raster GIS layers of different geosystems individually. It is followed by the counting of the total number of landslides falling in the individual feature class of these five raster layers. It includes counting the total number of pixels in each feature class. The number of landslides (LS) has been divided by the data so obtained, falling in each feature class with the total number of pixels (A) covered by the corresponding feature class. In this step, we assign "weights" to the normalized inputs by multiplying each of them by a value by 1000 and the landslide vulnerability weightages (LVW) assigned to each feature class. (Table 2 – Lithology, Table 3 – Lineaments, Table 4– Geomorphology, Table 5– Slope, Table 6 - LULC and Table 7 - road frequencies).

GIS Integration and Landslide Vulnerability

After assigning the Landslide Vulnerable Weightages (LVW) to the 5 rasterized geosystem layers' feature classes, they were all merged using Raster Calculator. The LVW value of each pixel of the weighted raster layers of all Geo systems and roadways (Fig. 5) was then added and matched, and the final integrated GIS layer representing different landslide vulnerable zones (LVZ) was generated (Fig. 11). In all 43297 pixels, such an integrated GIS output has completely collected LV weightages. Five LVZs have been found based on the LVZ map and data (Table 8), including very high, high, moderate, low, and very low.

CONCLUSION

The map showing LVZ was prepared by superimposing the landslide inventory layer over the final integrated GIS layer on landslide vulnerability. From the above investigations, it can be concluded that

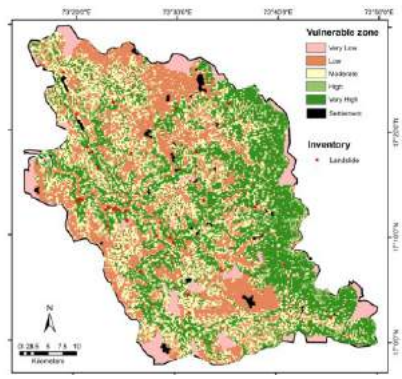

Fig. 11: Landslide vulnerable zone map of SRB.

Fig. 12: Rockfall near Bhatgaon – (17°16' N, 73° 24' E).

Fig. 13: Debris Slide near Asore (17°18' N, 73°22' E).

About 29% area of the Shastri River Basin (SRB) forms a highly vulnerable zone for land sliding.

These zones are mainly confined to steep slopes (11^0–20^0), grassy-land, highly weathered basalts (Purandargarh and Diveghat formation) (Fig. 12 and 13), and deep valleys, and in the vicinity of lineaments (400 m).

Results so obtained are validated in the field using GPS.

ACKNOWLEDGMENT

Dr. S. B. Joshi is thankful to Dr. S. V. Koti, Principal, Walchand College of Arts and Science, Solapur for extending help during present work and encouragement.

REFERENCES

Diaz, S., Fargione, J., Chapin, F.S. and Tilman, D. 2005. Biodiversity loss threatens human well-being, PLoS Biol., 4: 1300-1305.

Edison, T, and Ganapathy, P. 2020. Evaluation of landslide hazard and its impacts on the hilly environment of the Nilgiris District - a geospatial approach. Geoenviron. Disasters, 7(3): 139. https://doi.org/10.1186/s40677-019-0139-3

Greenbaum, D., Tutton, M., Bowker, M., Browne, T., Bulekha, J., Greally, K., Kuna, G., McDonald, A., Marsh, S., O'Connor, E. and Tragheim, D. 1995. Rapid methods of landslide mapping: Papua New Guinea case study. British Geol. Sur., Keyworth, Nottingham, UK, Tech. Report WC/95/27, p. 121

Guzzetti, F., Mondini, A.C., Cardinali, M., Fiorucci, F., Santangelo, M. and Chang, K.T. 2012. Landslide inventory maps: new tools for an old problem. Earth Sci. Rev., 112: 42-66. https://doi.org/10.1016/j.earscirev.2012.02.001

Jiu, J.J., Xu-Sheng, W. and Subhas, N. 2005. Confined groundwater zone and slope instability in weathered igneous rocks in Hong Kong. Eng. Geol., 80: 71-92

Juang, C.S., Stanley, T.A. and Kirschbaum, D.B. 2019. Using citizen science to expand the global map of landslides: introducing the cooperative open online landslide repository (COOLR). PLoS One, 14: e0218657

Meena, S.R., Ghorbanzadeh, O. and Hölbling, D. 2019. Comparison of Event-Based landslide inventories: A case study from Gorkha earthquake 2015, Nepal. Paper presented at the European Space Agency's 2019 Living Planet Symposium, Milan, Italy, 13-17 May 2019, European Space Agency, Paris, France, pp. 1-18.

Mitchell, C. and Cox, K.G. 1988. A geological sketch map of southern part of the Deccan province. Memoir of Geol. Soc. India, 10: 27-33

Nagarajan, R., Mukharji, A., Roy, A. and Khaire, M.V. 1998. Temporal remote sensing data and GIS application in landslide hazard zonation of part of Western Ghat, India. Int. J. Remote Sens., 19(4): 573-585

Prakash, N., Manconi, A. and Loew, S. 2020. Mapping landslides on EO data: performance of deep learning models vs. traditional machine learning models. Remote Sens., 18**:** 1937-1950

Ramakrishnan, S.S., Sanjeevi Kumar V., Zaffar Sadiq, M.G.S.M., Arulraj, M. and Venugopal, K. 2002. Landslide disaster management and planning: A GIS-based approach. Indian Cartog., 05: 192-195

Valdiya, K.S. 2011. Some geodynamic hot spots in India require urgent comprehensive studies. Curr. Sci., 100 (10): 1490-1499

Van Westen, T.W.J. Van, A. and Soeters, R. 2006. Landslide hazard and risk zonation: Why is it so difficult? Bull. Eng. Geo. Env., 65(2): 167-184

Wentworth, C.K.1930. A simplified method of determining the average slope of land surfaces Am. J. Sci., 21: 184-194

Materials Chemistry and Physics 275 (2022) 125250

Contents lists available at ScienceDirect

Materials Chemistry and Physics

journal homepage: www.elsevier.com/locate/matchemphys

Effects of sintering temperature on microstructure, initial permeability and electric behaviour of Ni-Mn-Zn ferrites

U.B. Gawas [a], V.M.S. Verenkar [b,*], V.T. Vader [c], Anil Jain [d], Sher Singh Meena [d,**]

[a] Department of Chemistry, Dnyanprassarak Mandal's College and Research Centre, Assagao, Goa, 403 507, India
[b] School of Chemical Sciences, Goa University, Taleigao Plateau, Goa, 403 206, India
[c] Department of Chemistry, Walchand College of Arts and Science, Solapur, 413 006, India
[d] Solid State Physics Division, Bhabha Atomic Research Centre, Mumbai, 400 085, India

HIGHLIGHTS

- Ni-Mn-Zn ferrites with dense and fined grained microstructure are obtained at relatively lower sintering temperature.
- Mössbauer spectra confirmed only sextets in low Mn-substitution ($x \leq 0.2$) while $x \geq 0.3$ exhibits sextets and doublet.
- Room temperature dc resistivity values observed in the range 10^8–10^7 are found to be appreciably higher.
- Dielectric measurements suggest the better stoichiometry and homogeneity for all the sintered compositions.
- Improvement in the initial permeability is observed upon Mn substitution in Ni-Zn ferrites.

GRAPHICAL ABSTRACT

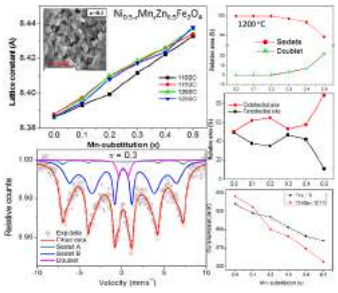

ARTICLE INFO

Keywords:
Ni-Mn-Zn ferrites
IR spectroscopy
Mössbauer spectroscopy
dc resistivity
Dielectric constant
Initial permeability

ABSTRACT

The effects of sintering temperature on microstructure, initial permeability, and electrical behaviour of $Ni_{0.5-x}Mn_xZn_{0.5}Fe_2O_4$ ($0.0 < x < 0.5$) prepared using the precursor combustion method have been investigated. X-ray diffraction analysis confirmed the single phase cubic spinel structure of $Ni_{0.5-x}Mn_xZn_{0.5}Fe_2O_4$ ($0.0 < x < 0.4$) compositions sintered at 1100 °C. The Mn^{2+} substituent preferentially occupies tetrahedral sites as indicated by the Rietveld analysis and the increase in the IR absorption frequency of ν_1 band with increasing Mn substitution. The SEM measurements have revealed homogeneous microstructures of the ferrites with narrow grain size distribution in the range 0.93μm–1.86 μm. Mössbauer spectra exhibit a superposition of two Zeeman sextets for the compositions $x \leq 0.2$, a superposition of two Zeeman sextets, and a paramagnetic doublet for the compositions, $x = 0.3$ and 0.4, and one sextet and single quadrupole doublet for a composition, $x = 0.5$. The activation energy in the range 0.258 eV–0.612 eV suggests a polaron hopping type conduction mechanism in all the sintered ferrites. The dielectric constant in the range 0.057–55.21 and lower dielectric loss (10^{-2}) imply better stoichiometry and homogeneity. The initial permeability increases at lower Mn substitution ($x = 0.2$) and exhibits a decrease as the Mn substitution increases. The dc resistivity, dielectric constant, and initial permeability values suggest the suitability of these ferrites for high frequency device applications.

* Corresponding author.
** Corresponding author.
E-mail addresses: vmsv@rediffmail.com (V.M.S. Verenkar), ssingh@barc.gov.in (S.S. Meena).

https://doi.org/10.1016/j.matchemphys.2021.125250
Received 23 March 2021; Received in revised form 27 August 2021; Accepted 14 September 2021
Available online 18 September 2021

1. Introduction

Soft magnetic ferrites have been subjected to detailed investigation for their electromagnetic properties which find use in technological applications such as transformer core, multilayered chip inductors (MLCIs), information storage systems, electronic communication, computer circuitry, microwave filters, etc. [1–5]. The electromagnetic properties of spinel ferrites are much better and more practicable over pure metal due to their high electrical resistivity, excellent magnetic permeability and, availability of simple and easy preparation routes, which lowers the processing cost. Furthermore, the spinel class ferrites exhibit high corrosion resistance and excellent thermal stability. Among, the spinel ferrite system, the Ni-Zn ferrites, and Mn-Zn ferrites have been investigated extensively for their electric, dielectric, magnetization as well as permeability properties which are important in specific applications [6–9]. The Mn-Zn ferrites with low electrical resistivity and high magnetic permeability are useful for low frequency applications [10–12] while, the Ni-Zn ferrites with high resistivity and relatively low permeability are suitable for high frequency applications [13–15]. However, for the best performance in high frequency applications, ferrites with high permeability as well as high resistivity are indispensable. This has initiated a lot of research work on various mixed Ni-Mn-Zn ferrite compositions to synthesize materials with better permeability and resistivity characteristics [16–20]. It is a well known fact that the electromagnetic properties of spinel ferrites are controlled by the particle/grain size, microstructure, heat treatment (during synthesis), and cation distribution-rearrangements (during sintering) among the tetrahedral [A] and octahedral [B] interstices in the cubic lattice. These characteristics ultimately depend on the synthesis technique employed and hence there has been a lot of focus on the development of the novel synthetic routes to improve upon the electromagnetic characteristics. Various synthetic approaches adopted by the different researchers include, citrate precursor method [16], co-precipitation [17–19], sol-gel [20,21], combustion [21], precursor combustion method [22,23] etc. The precursor combustion method which utilizes hydrazinated carboxylate precursors has been employed for the synthesis of various materials including spinel ferrites [21–23] due to the autocatalytic decomposition and self-propagating combustion of these precursors. Moreover, the mixed metal oxides are formed at relatively lower temperatures. To the best of our knowledge, the structural and electromagnetic properties of mixed $Ni_{0.5-x}Mn_xZn_{0.5}Fe_2O_4$ ($0.0 < x < 0.5$) ferrites at lower sintering temperature from 1100 °C to 1250 °C with an interval of 50 °C is not reported so far. Here, we are reporting the effects of sintering temperature on the microstructure, electric, and initial permeability of $Ni_{0.5-x}Mn_xZn_{0.5}Fe_2O_4$ ($0.0 < x < 0.5$) ferrites processed using the fumarato hydrazinate precursor combustion method.

2. Experimental

2.1. Synthesis of $Ni_{0.5-x}Mn_xZn_{0.5}Fe_2O_4$ ($0.0 < x < 0.5$)

The manganese substituted nickel zinc ferrites, $Ni_{0.5-x}Mn_xZn_{0.5}Fe_2O_4$ ($0.0 < x < 0.5$) ferrites were prepared using the fumarato hydrazinate precursor combustion method. All the reagents used in the synthesis were analytical grade. In a typical synthesis, the yellow coloured precipitate of nickel manganese zinc ferrous fumarato hydrazinate complex was obtained by adding an aqueous solution of mixed metal chlorides to an aqueous solution of sodium fumarate-hydrazine hydrate mixture under the N_2 atmosphere. The precipitate was then filtered, washed with ethanol, and dried on suction using diethyl ether. The details of the synthesis protocol, characterization of the precursor complexes, and the spectroscopic and magnetic properties of the 'as obtained' nanoferrites are reported elsewhere [24,25]. The 'as obtained' nanoferrites were ground for 2 h using mortar and pestle and calcined at 500 °C for 5 h to remove the residual carbon completely. The calcined powders were pelletized and pre-sintered at 800 °C for 5 h using a muffle furnace. The pre-sintered pellets were then milled for 2 h and pressed into pellets (10 mm × 2 mm dimension) and toroids (20 mm × 10 mm x 2 mm dimension) under a pressure of 7 tons/inch^2 for 3 minutes using a die and hydraulic press. The pellets and toroids were finally sintered in the air for 1 h at different temperatures from 1100 °C to 1250 °C with an interval of 50 °C (heating rate 5 °C per minute) using an open tubular furnace and air-cooled.

2.2. Material characterization

The structural analysis of the sintered $Ni_{0.5-x}Mn_xZn_{0.5}Fe_2O_4$ ($0.0 < x < 0.5$) ferrites were performed using the Rigaku X-ray diffractometer (Ultima-IV) employed with the copper K_α X-ray source and nickel filter. The IR spectra were recorded using Shimadzu FTIR spectrometer (Prestige 21). Mössbauer spectroscopic measurements were performed at room temperature with a Mössbauer spectrometer operated in a constant acceleration mode (triangular wave) in transmission geometry using Co-57 γ-radiation source in the Rh matrix of strength 10 mCi. The velocity scale calibration was done employing an enriched α-^{57}Fe metal foil. The line width (inner) of the calibration spectra was 0.26 mms^{-1}. The Mössbauer spectroscopic data were fitted by using a Win-Normos site fit program. Neutron powder diffraction (NPD) experiment was performed at room temperature using the neutron powder diffractometer PD-I ($\lambda = 1.094$ Å) with three linear position-sensitive detectors at Dhruva reactor, Bhabha Atomic Research Center, India. Rietveld refinement of the powder NPD data was performed using FULLPROF software package. The surface topology of the sintered ferrites was studied using a JEOL scanning electron microscope (5800LV). The energy dispersive X-ray spectroscopic measurements were carried out using ZEISS scanning electron microscope (EVO 18). The average grain sizes (grain diameter) were obtained from the optical micrographs by the linear intercept method [26]. Average 60–80 grains were used for the grain diameter measurements. The room temperature and high temperature dc resistivity studies were performed by using two probes method and the current flow across the sample (at constant voltage) was measured using the Keithley multimeter (2010). The resistivity was calculated using relation [27].

$$\rho = R\ A\ /\ l \tag{1}$$

where ρ is resistivity, R is the resistance calculated from measured current, A is the area of cross-section of pellet, and l is the thickness of the pellet. The dc resistivity was measured from room temperature to 773 K. The log resistivity (ρ) values were then plotted against 1000/T. The resistivity-temperature behaviour obeys the relation [27].

$$\rho = \rho_o\ \exp^{Ea\ /\ kT} \tag{2}$$

where ρ is the resistivity at absolute temperature T, E_a is the activation energy and k is the Boltzman constant. The activation energy of each sample was determined from the slope of the linear plots using the relation [27].

$$\text{Slope} = E_a\ /\ k \tag{3}$$

The dielectric measurements were carried out by using Wayne Kerr LCR meter (6500P) in the frequency range 20 Hz to 10 MHz at room temperature and all the high temperature measurements (up to 250 °C) were performed at 1 kHz on silver coated pellets. The dielectric constant (ε') was calculated using the relation [28].

$$\varepsilon' = Cd\ /\ A\ \varepsilon_o \tag{4}$$

where C represents the capacitance of the pellet (in Farad), d is the thickness of the pellet (in meters), ε_o is the permittivity of free space (8.854×10^{-12} F m^{-1}) and A is the cross-sectional area of the pellet (in m^2). The dielectric loss tangent (tan δ) was calculated using the relation:

$$tan\ \delta = D = 1\ /\ Q \tag{5}$$

where D is the dissipation factor and Q is the quality factor. The inductance of the toroidal cores of 50 turns was measured at room temperature over the frequency range from 100 Hz to 10 MHz using Wayne Kerr LCR meter (6500P). All the high temperatures (up to 773 K) inductance measurements were carried out at 1 kHz. The initial permeability of the toroidal core was calculated from the low field inductance by using the formula [29].

$$L = 0.0046\ \mu_i\ N^2\ h\ \log\ d_1 / d_2 \quad (6)$$

where L is the inductance (in μH), d_1 is the outer diameter of a toroid (in meters), d_2 is the inner diameter of a toroid (in meters), μ_i the initial permeability of the core and h is the height of the core (in meters).

3. Results and discussion

3.1. X-ray diffraction measurements

The XRD patterns of $Ni_{0.5-x}Mn_xZn_{0.5}Fe_2O_4$ ($0.0 < x < 0.5$) ferrites sintered at the 1100 °C and 1250 °C are represented in Fig. 1a and 1b, respectively, while the XRD patterns of ferrites sintered at the 1150 °C and 1200 °C are given in Fig. S1(a-b). The XRD patterns indicate the formation of cubic spinel structure [17] except for a composition $x = 0.5$ sintered at 1100 °C and 1150 °C. For composition $x = 0.5$, small impurity peaks observed at $2\theta = 24.4°$, 33.1°, 36.4° and 54.1° were indexed to the α-Fe_2O_3 impurity phase [23]. The enlarged view of (311) peak in the XRD pattern of the ferrites Fig. S2(a-d) shows a clear shift in (311) peak. The insets of Fig. S2(a-d) in the form of a graph further clearly demonstrates the shift in the position of (311) peak linearly towards the lower angle with the increasing Mn substitution. This shift of (311) peak towards a lower angle indicates that the lattice constant increases with increasing Mn substitution [30,31]. As per Bragg's law, the value of lattice constant 'a' $\propto 1/\sin\theta$. The structural parameters derived from XRD analysis are presented in Table S1. The lattice constants exhibit a linear increase from 8.3859 Å - 8.4327 Å, 8.3879 Å −8.4340 Å, 8.3859 Å - 8.4371 Å, and 8.3865 Å - 8.4379 Å in ferrites sintered at 1100 °C, 1150 °C, 1200 °C, and 1250 °C, respectively. The variation of lattice constant with Mn substitution (x) is shown in Fig. 1c. There is no significant increase in lattice constant observed after sintering at 1150 °C, 1200 °C, and 1250 °C except for ferrites sintered at 1100 °C, wherein a small increase in the lattice constant is observed. This variation in lattice parameters with the increasing Mn substitution is attributed to the larger ionic radius of the substituent Mn^{2+} ions (0.82 Å) than that of the Ni^{2+} ions (0.70 Å). The X-ray density, experimental density, and porosity exhibit decreasing trend with increasing Mn substitution (x) [Table S1]. However, the trend of these properties in each ferrite composition sintered at different temperatures is found to be different. The X-ray density shows a negligible variation while, the experimental density exhibits a significant increase with an increasing sintering temperature, thus causing a sharp decrease in the porosity [Table S1]. The decrease in the densities with the increase in Mn substitution is due to a) the substitution of heavier NiO by the lighter MnO in the cubic lattice and b) the substitution by larger Mn^{2+} ions for smaller Ni^{2+} ions which cause the lattice expansion and thereby increase in the unit cell volume, consequently, the density decreases. However, with an increase in the sintering temperature, the experimental density increases linearly. This is because of the increased thermal energy that generates the force which drives the grain boundaries to grow over the pores, consequently, the pore volume decreases, thereby decreasing the porosity. The Rietveld refined XRD patterns of $Ni_{0.5-x}Mn_xZn_{0.5}Fe_2O_4$ (0.0 and 0.5) ferrites sintered at 1250 °C are shown in Fig. S3 (a,b), while the variation of the tetrahedral bond length 'r_A' is shown in Fig. S3(c). The tetrahedral bond length increases linearly with increasing Mn substitution up to $x = 0.4$. This is due to the site preference of Mn^{2+} ions for tetrahedral *(A)* sites over that of Fe^{3+} ions. Thus, the increase in the Mn^{2+} (r = 0.82 Å) concentration results in the transfer of Fe^{3+} (r =

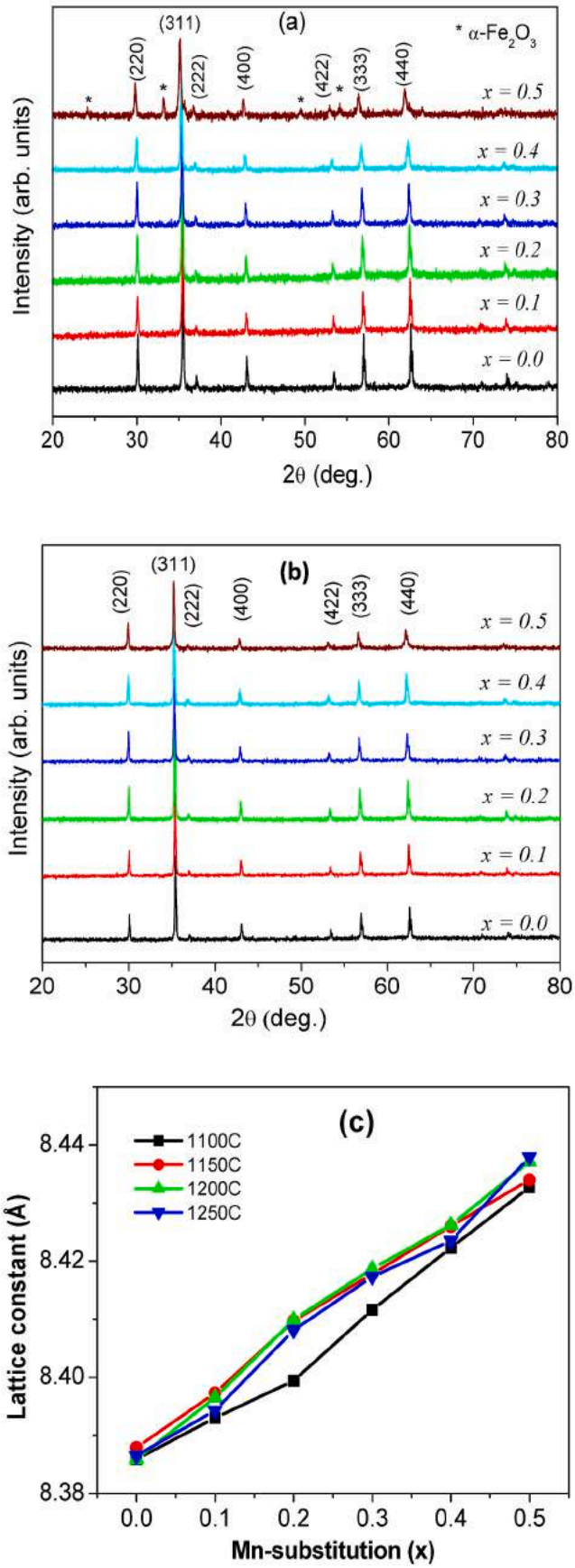

Fig. 1. XRD patterns of $Ni_{0.5-x}Mn_xZn_{0.5}Fe_2O_4$ ($0.0 < x < 0.5$) ferrites sintered at, (a) 1100 °C and (b) 1250 °C. (c) Variation in lattice constant with increasing the temperature and Mn-substitution (x).

0.645 Å) ions from tetrahedral *(A)* sites to octahedral [B] sites thereby increasing the tetrahedral bond length (r_A).

3.2. IR spectroscopic studies

The FTIR spectra of ferrites sintered at 1200 °C and 1250 °C are shown in Fig. 2a and b, respectively, and the IR absorption frequencies of all the sintered ferrites are given in Table S2. The occurrence of two principal absorption bands (ν_1, ν_2) in the frequency range 750 cm^{-1}-340 cm^{-1} is a characteristic feature of spinel ferrites. The high frequency band (ν_1 = 590 cm^{-1} - 564 cm^{-1}) is due to the tetrahedral Fe^{3+}—O^{2-} bonds stretching vibrations, while, the low frequency band (ν_2 = 421 cm^{-1} - 404 cm^{-1}) arises due to the Fe^{3+}–O^{2-} groups occupying octahedral interstices in the cubic spinel structure of ferrites [32–34]. The observed differences in the positions and intensities of IR bands are due to the different M^{n+}–O^{2-} bond lengths for the tetrahedral *(A)* and octahedral [B] sites, as the frequency of bond vibration, depends on the cation mass, M^{n+}–O^{2-} distance, and the bonding force [35]. The weak shoulder (ν'_1) which appears in the region 733 cm^{-1} - 728 cm^{-1} with the increasing Mn substitution has been attributed to the Mn^{2+}–O^{2-} bonds stretching vibration at the tetrahedral sites [36]. Another weak shoulder (ν''_1) observed in the range 650 cm^{-1} - 600 cm^{-1} has been assigned to stretching vibrations of the tetrahedral Zn^{2+}–O^{2-} bonds. At lower Mn substitution the concentration of Fe^{3+} ions at tetrahedral (*A*) sites is relatively high as a result the ν''_1 band is merged with ν_1 band in the compositions, x = 0.0 and 0.1. As the Mn substitution increases ($x \geq$ 0.2), the concentration of Mn^{2+} ions at the *A* sites increases, resulting in the transfer of Fe^{3+} ions from *A* sites to B sites thereby decreasing their concentration at the *A* sites. This causes the decrease in the intensity of the ν_1 band as a result the ν''_1 shoulder is visible in the compositions, $x \geq$ 0.2. Mohammad et al. [37] have observed similar shoulder in the IR spectra of Mg-Zn ferrites and Deraz [38] has reported similar results for the alumina-doped zinc ferrites. They have assigned this shoulder to both Fe^{2+}–O^{2-} and Zn^{2+}–O^{2-} tetrahedral complexes. However, the Mössbauer study of these sintered compositions has ruled out any possibility of Fe^{2+} ions existence and hence this weak shoulder (ν''_1) has been assigned to the tetrahedral Zn^{2+}–O^{2-} bonds stretching vibrations. A very weak band (ν'_2) observed in the region 468 cm^{-1} - 461 cm^{-1} for all the compositions (except for x = 0.5) has been assigned to the octahedral Ni^{2+}–O^{2-} bond stretching vibrations, as the concentration of Ni^{2+} ions at the B sites is relatively high [39]. The IR band (ν''_2) observed in the region 349 cm^{-1} - 337 cm^{-1} is assigned to Zn^{2+}–O^{2-} stretching vibrations at the B sites [39–41]. The observed deviation in the position of the peaks is mainly due to the factors such as the amount of dopant, synthesis technique, grain size, and density [42–44]. The variation in the absorption frequency of ν_1 and ν_2 bands with increasing Mn substitution in the ferrites sintered at 1200 °C and 1250 °C are shown in Fig. 2c and d, respectively. The wavenumber for absorption band ν_1 (A-site) is found to decrease with an increasing Mn substitution indicating that the tetrahedral bond length is increasing. The wavenumber for absorption band ν_2 (B-site) is found to decrease up to $x \leq 0.3$ and beyond $x > 0.3$, it increases [Table S2]. These observations can be explained considering the site preference and distribution of cations among *A* and B sites. When Mn^{2+} ions (r = 0.82 A°) are introduced for Ni^{2+} ions (r = 0.70 A°) in the spinel lattice they displaces Fe^{3+} ions (r = 0.645 A°) from *A* to B sites, since Mn^{2+} ions prefers tetrahedral sites over Fe^{3+} ions. This results in a decrease in the concentration of Fe^{3+} ions at the *A* sites and an increase in the tetrahedral bond length (r_A). As a result, the absorption frequency and intensity of ν_1 band decrease. For the ν_2 band Mn substitution has hardly any effect on octahedral bond length (r_B) as a result there is no noticeable change in the absorption frequency of the ν_2 band , however, the intensity increases due to an increase in the Fe^{3+} ions concentration at the B sites. Thus, there is a significant contribution of the tetrahedral bond length (r_A) to the increase in the unit cell dimensions which is in

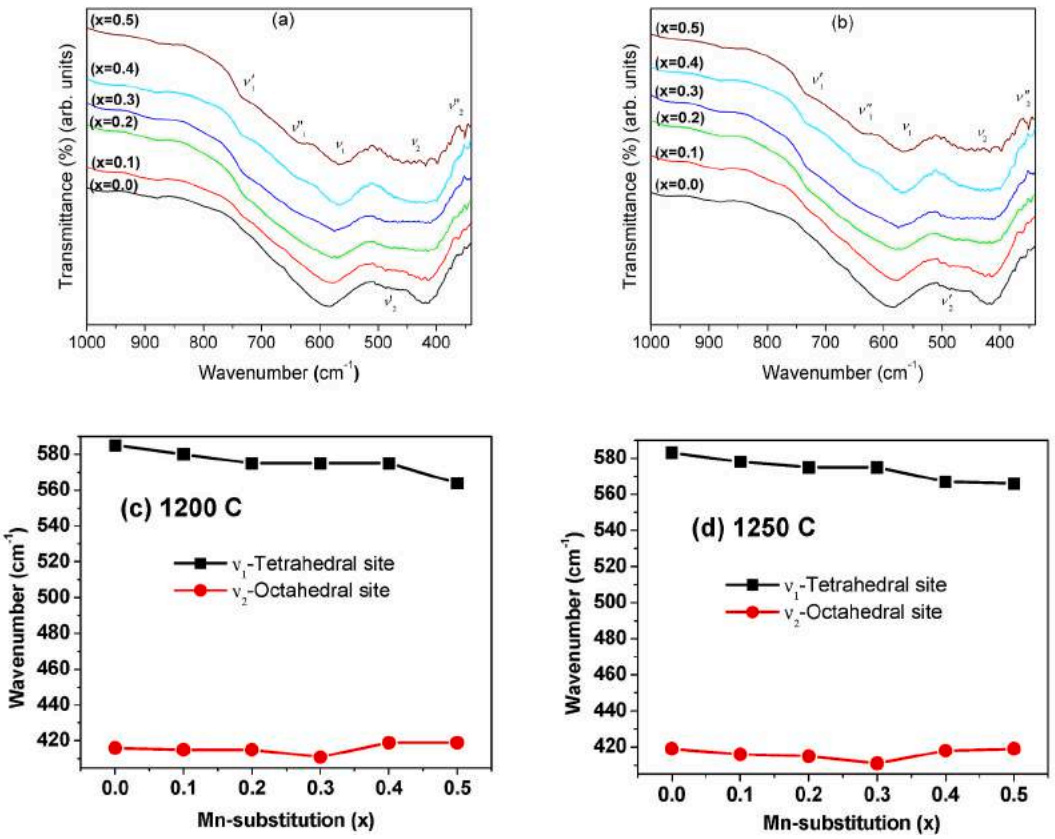

Fig. 2. (a–d). IR spectra of $Ni_{0.5-x}Mn_xZn_{0.5}Fe_2O_4$ ($0.0 < x < 0.5$) ferrites sintered at (a) 1200 °C and (b) 1250 °C. Variation in absorption bands (ν_1 and ν_2) with increasing the Mn-substitution in samples sintered at (c) 1200 °C and (d) 1250 °C.

agreement with the Rietveld analysis results and Mössbauer study.

3.3. SEM microstructure and EDX measurements

The SEM images of ferrite compositions sintered at 1200 °C and 1250 °C are presented in Fig. 3a and b, respectively. The average grain sizes (grain diameter) obtained from optical micrographs are given in Table S4. The variation in average grain size with increasing Mn substitution in $Ni_{0.5-x}Mn_xZn_{0.5}Fe_2O_4$ ($0.0 < x < 0.5$) ferrites sintered at different sintering temperatures is shown in Fig. 3c. The average grain size increases linearly (0.59 μm–1.86 μm) with an increase in Mn content [45]. This is due to the lower melting point of Mn as compared to Ni [20]. The increase in grain diameter is very small at lower Mn content ($x \leq 0.2$) but at higher Mn content ($x > 0.2$) the grain size increases to a greater extent. The samples sintered at 1100 °C and 1150 °C have revealed less dense microstructure with wider grain distribution in the range of 0.59 μm–1.13 μm and 0.62 μm–1.21 μm, respectively, while the samples sintered at 1200 °C and 1250 °C presented a homogeneous denser microstructure with narrow grain distribution in the range of 0.93 μm–1.36 μm and 1.30 μm–1.86 μm, respectively [Table S4]. The average grain diameter increases with Mn substitution and the largest particle diameter (3.91 μm) is observed for composition, $x = 0.3$, sintered at 1250 °C which is much lower than those reported by the conventional method [46,47]. The intragranular porosity is found to be very low in all the sintered compositions. The EDX spectra of the sintered $Ni_{0.5-x}Mn_xZn_{0.5}Fe_2O_4$ ($x = 0.0$ and 0.5) ferrites are represented in Fig. S4 and the compositional percentage (weight %) of zinc in ferrites sintered at different temperatures are given in Table S3. These results suggest that there is either no zinc loss or it is negligible in all the samples sintered up to the sintering temperature of 1250 °C. Therefore the samples maintain the proper stoichiometric composition at all sintering temperatures studied in the present investigation.

3.4. Mössbauer spectroscopic and neutron powder diffraction (NPD) studies

The Mössbauer spectra of ferrites sintered at 1200 °C are given in Fig. 4 (a,b) and the Mössbauer effect parameters derived from the room temperature Mössbauer spectra are presented in Table 1. The Mössbauer spectra for compositions $x \leq 0.2$, display superposition of the two Zeeman sextets. The sextet with a higher magnetic field is attributed to Fe^{3+} ions occupying the tetrahedral *(A)* sites and the one with a lower magnetic field is assigned to Fe^{3+} ions present at the octahedral [B] sites. The Mössbauer spectra of the compositions $0.2 < x > 0.4$ exhibit a superposition of two Zeeman sextets due to the *A* and B site Fe^{3+} ions and a paramagnetic doublet, while for the composition, $x = 0.5$, the spectrum consists of one sextet and single quadrupole doublet. The internal magnetic field for *A* and B sites shows a decrease with an increase in Mn concentration at lower Mn substitution ($x \leq 0.2$) and increases at higher Mn substitution ($x \geq 0.3$) for the B site. The internal magnetic field for site *A* is greater than that of site B sites which indicates that the Mn(A)–Fe(B) supertranferred interaction is less than the Fe(A)-Fe(B) interaction and presence of Mn^{2+} ions as nearest neighbours decreases the magnetic hyperfine field at the B sites [48]. The spectra of ferrites with composition, $x > 0.2$ indicate that the ferrites have ferromagnetic and paramagnetic nature simultaneously. The appearance of the central paramagnetic doublet is ascribed to the Fe^{3+} ions surrounded by the non-magnetic neighbours which are not involved in the long range magnetic ordering. The variation in relative area of sextets and doublet, the relative area of the *A* and B site, and hyperfine magnetic field with increasing Mn-substitution are presented in Fig. 4c,d,e, respectively. The variation in the average outer line width (<Γ>) of sextets is shown in Fig. 4f. The value of <Γ> is found to be maximum for composition, $x = 0.2$ which confirms the maximum distortion around Fe^{3+} ions, possibly due to slight variations in the spin-lattice relaxation times with an increase in Mn substitution [32]. The values of isomer shift (δ) for the *A* site and B site are found to be between 0.224 mms^{-1} - 0.313 mm s^{-1} and 0.271 mm s^{-1} - 0.365 mm s^{-1}, respectively, whereas the isomer shifts values for doublet are found between 0.309 mm s^{-1} - 354 mm s^{-1}. These values indicate that Fe-ions are present in +3 high spin states [49–53]. For plotting the tetrahedral and octahedral sites of Fe-ions, we have considered the doublet arising due to both sites of Fe-ions [54].

The Mössbauer spectra of ferrites sintered at 1100 °C are given in Fig. 5 (a) and the parameters derived from the spectra are presented in Table 2. The values of isomer shift (δ) for sextets are found to be between 0.282 and 0.534 mm s^{-1}, whereas the isomer shifts values for doublet are found between 0.352 and 376 mm s^{-1}. These values indicate that Fe-ions are in +3 high spin state [49–53]. Variation in relative area of sextets and doublet with increasing the Mn-substitution (x) is shown in Fig. 5 (b). The trend in relative area of sextets and doublet is matching with the earlier measurements done on samples sintered at 1200 °C [Fig. 4c]. Based on the Mössbauer results, we have not found any indication of the presence of Fe^{2+} ions in both series (samples sintered at 1100 and 1200 °C) of samples.

We have fitted high angle part of the neutron diffraction pattern (to avoid the magnetic peaks present at the low angle) and refined the occupancies of oxygen ions [Fig. S5]. In the refinement, we have assumed only nuclear part and the magnetic part has been neglected. Therefore, we have fitted only high angle part of the neutron diffraction data. Determination of the magnetic structure is out of the scope of the present work. The neutron diffraction is very sensitive to the oxygen position and occupancies. Our analysis shows that compositions are $Ni_{0.2}Mn_{0.3}Zn_{0.5}Fe_2O_{4.16}$ and $Mn_{0.5}Zn_{0.5}Fe_2O_{4.18}$.

Mössbauer shows that Fe is in +3 state and Zn and Ni ions are allowing in 2+ state. To keep the charge neutrality of the ions in both compositions the following Mn oxidation state can be suggested.

$$Ni_{0.2}[Mn^{3+}]_{0.3}Zn_{0.5}Fe_2O_{4.16} \text{ and } [Mn^{2+}]_{0.17}[Mn^{3+}]_{0.33}Zn_{0.5}Fe_2O_{4.18}$$

Therefore, it is concluded that Mn is in the mixed oxidation states (3+ and 2+) in these samples.

3.5. Dc resistivity

The plot of log resistivity (log ρ) against 1000/T of the ferrites sintered at 1100 °C and 1250 °C are given in Fig. 6a and b respectively. The plots exhibit a typical negative temperature coefficient of the resistance (NTCR) behaviour of semiconductors and each plot can be divided into three linear regions. The first (lower temperature) region extends up to the 390 K, where a change in the slope is observed. In this region, the conductivity is found to be very low and nearly independent of the temperature. The second resistivity region extends up to 645 K and conductivity in this region is found to depend on the Mn content and is much lower than that of the first region. Also, there is a transition observed in this region which is attributed to the change in the magnetic behaviour from ferrimagnetic state to paramagnetic state, and the temperature at which this change occurs is referred to as Curie temperature. The third (higher temperature) region of resistivity up to 773 K represents the conductivity in the paramagnetic region. In this region, the concentration of Fe^{2+} and Mn^{3+} increases by the processes [55].

$$Ni^{2+} + Fe^{3+} \leftrightarrow Ni^{3+} + Fe^{2+} \quad (7)$$

$$Fe^{3+} + Mn^{2+} \leftrightarrow Fe^{2+} + Mn^{3+} \quad (8)$$

This increase in the concentration of Fe^{2+} and Mn^{3+} ions increases the hopping and thereby the conductivity in the higher temperature region. In the ferrimagnetic region (from 390 K up to 645 K), the activation energies are observed in the range 0.258 eV–0.491 eV while, the values vary from 0.349 eV to 0.612 eV in the paramagnetic region [Table S4]. The values of activation energy observed for all the sintered compositions are found to be higher than those reported for various other ferrites [56,57]. These values suggest the polaron hopping type

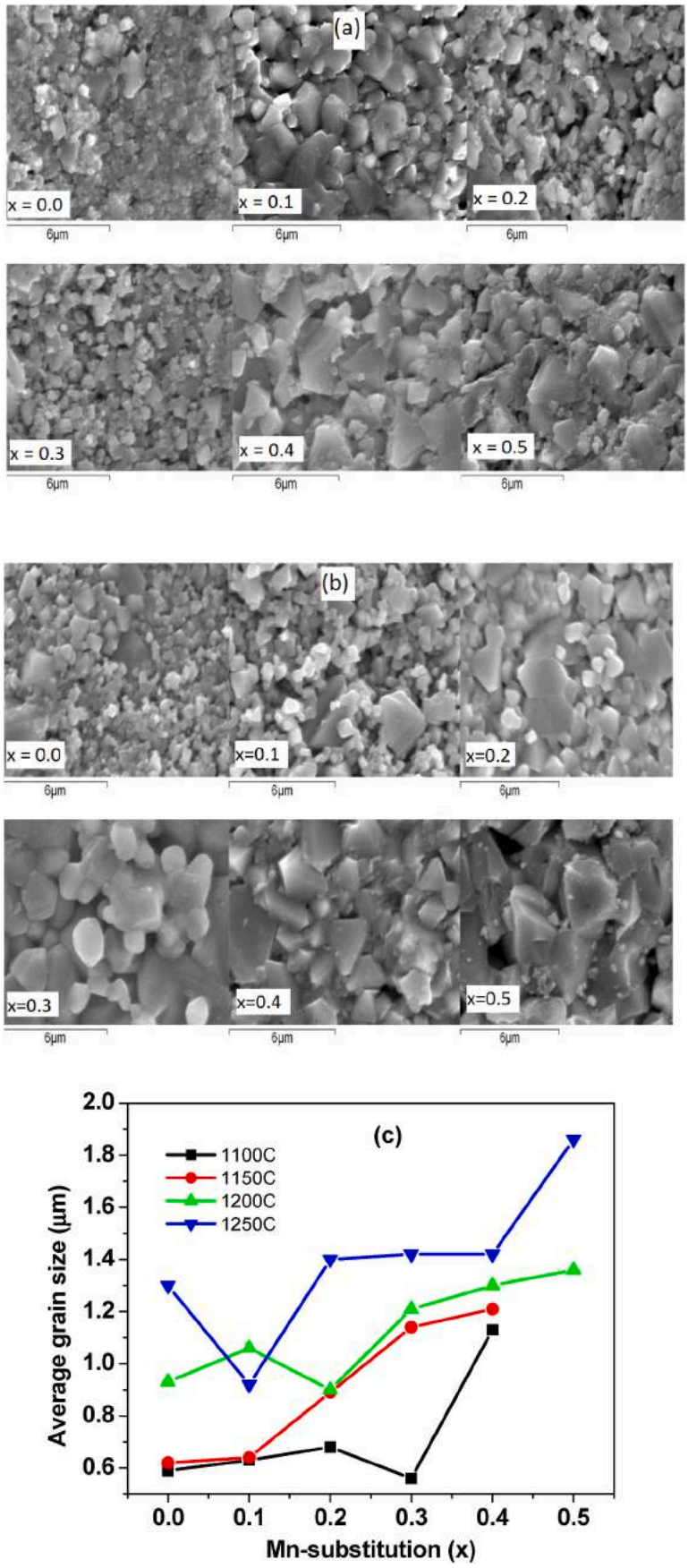

Fig. 3. (a–c). SEM of $Ni_{0.5-x}Mn_xZn_{0.5}Fe_2O_4$ ($0.0 < x < 0.5$) ferrites sintered at, (a) 1200 °C and (b) 1250 °C. (c) Variation in average grain size with increasing Mn-substitution (x).

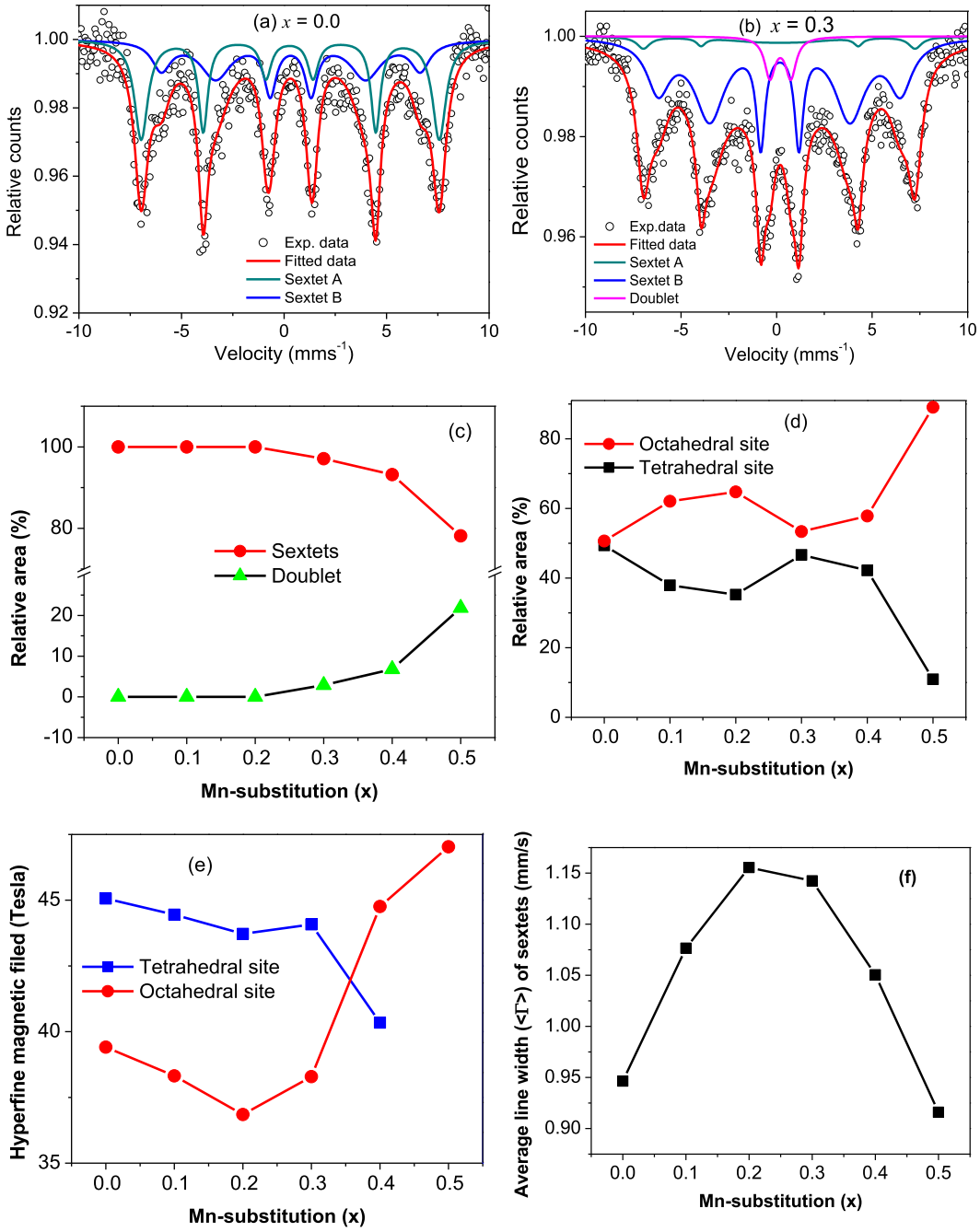

Fig. 4. (a–f). Mössbauer spectra of $Ni_{0.5-x}Mn_xZn_{0.5}Fe_2O_4$, a) $x = 0.0$ and b) $x = 0.3$ sintered at 1200 °C. (c) Variation in relative area of sextets and doublet with increasing the Mn-substitution (x). (d) Variation in relative area of tetrahedral site, octahedral site. (e) Variation in hyperfine magnetic field with increasing the Mn-substitution (x). (f) Variation in average outer line width (<Γ>) of sextets.

conduction mechanism in ferrites [57,58]. The room temperature log ρ (log ρ = 10^7–10^8 Ω cm) values [Table S4] of the ferrite compositions sintered at 1200 °C were found higher than the reported [59]. Further, the dc resistivity is found to decrease with increasing Mn substitution. This variation is explained considering the cation distribution among the tetrahedral *(A)* and octahedral [B] sites in cubic spinel lattice. It is known that Zn^{2+} ions and Ni^{2+} ions occupy *A* sites and B sites respectively, while, the Fe^{3+} ions and Mn^{2+}/Mn^{3+} ions can occupy both *A* and B sites. However, the probability of finding Fe^{3+} at B sites and Mn^{2+}/Mn^{3+} ions at *A* sites is more [58,60]. When Mn^{2+}/Mn^{3+} ions are introduced at the cost of Ni^{2+} ions, some of the Fe^{3+} ions move from *A* to B sites, which increases the concentration of Fe^{3+} ions at the B sites thereby increasing the ion hopping probability and hence the conductivity [61,62]. Moreover, the increase in grain size with increasing Mn substitution further contributes to their low resistivity. The dc resistivity is found to decrease with an increase in the sintering temperature [Table S4]. This behaviour is attributed to the increase in the grain size [59,62] since the average grain size increases from 0.56 μm to 1.86 μm with an increase in the sintering temperature from 1100 °C to 1250 °C. The higher dc resistivity values of samples sintered at the temperatures ≤1200 °C are ascribed to the smaller grains with a large number of grain boundaries [63]. These grain boundaries act as scattering centers for electron flow, thus increasing the grain boundary resistance and hence the resistivity. Moreover, the oxidation of Fe^{2+} formed during the sintering process advances faster in the smaller grains due to a larger surface to volume ratio [63], and hence the re-conversion

Table 1
Room temperature Mössbauer effect parameters: isomer shift 'δ', quadrupole splitting 'Δ', hyperfine field 'H_{hf}', relative Area 'R_A' and outer line width 'Γ' of $Ni_{0.5-x}Mn_xZn_{0.5}Fe_2O_4$ ($x = 0.0$–0.5) ferrites sintered at 1200 °C/1h.

Mössbauer effect parameters	Site	x					
		0.0	0.1	0.2	0.3	0.4	0.5
*δ (mms^{-1})	Sextet 1, (*A*)	0.283	0.306	0.224	0.261	0.313	–
	Sextet 2, [*B*]	0.317	0.365	0.275	0.271	0.316	0.331
	Doublet	–	–	–	0.309	0.333	0.354
Δ (mms^{-1})	Sextet 1, (*A*)	0.035	−0.011	0.019	−0.022	−0.028	–
	Sextet 2, [*B*]	0.008	0.064	0.044	−0.022	0.0028	−0.013
	Doublet	–	–	–	1.095	0.692	0.453
H_{hf} (Tesla)	Sextet 1, (*A*)	45.06	44.45	43.72	44.08	40.34	–
	Sextet 2, [*B*]	39.41	38.32	36.85	38.29	44.76	47.03
	Doublet	–	–	–	–	–	–
R_A (%)	Sextet 1, (*A*)	49.37	37.94	35.25	45.2	38.78	–
	Sextet 2, [*B*]	50.63	62.06	64.75	51.90	54.54	78.15
	Doublet	–	–	–	2.90	6.68	21.85
Γ (mms^{-1})	Sextet 1, (*A*)	0.795	0.739	0.929	0.823	1.264	–
	Sextet 2, [*B*]	1.098	1.414	1.382	1.462	0.837	0.916
	Doublet	–	–	–	0.665	0.933	0.385
Goodness of fit (χ2)		1.131	1.055	1.131	1.123	1.085	1.155

*Isomer shift values are relative to α-Fe metal foil (δ = 0.0 mm s^{-1}), (): tetrahedral, []: octahedral.

of any Fe^{2+} back to Fe^{3+} takes place readily [64]. Therefore, the samples sintered at a lower temperature (≤1200 °C) displayed high resistivity. The lower dc resistivity of the ferrites sintered above 1200 °C has been attributed to an increase in the grain size and zinc losses due to volatilization [65–67]. However, the EDX measurements have revealed negligible zinc losses in the ferrites sintered at 1250 °C and hence the lower dc resistivity can be attributed to their larger and non-uniform grain sizes. From the dc resistivity study, it can be inferred that the samples sintered at ≤ 1200 °C exhibit higher dc resistivity and activation energy which is credited to the better purity and homogeneity with negligible zinc loss obtained via the precursor combustion technique.

3.6. Dielectric behaviour

The frequency variation of dielectric constant (ε′) and dielectric loss tangent (tan δ) of $Ni_{0.5-x}Mn_xZn_{0.5}Fe_2O_4$ ($0.0 < x < 0.5$) ferrites sintered at 1200 °C are depicted in Fig. 7a and b respectively, while the dielectric constant and dielectric loss of all the sintered compositions obtained at 1 kHz are given in Table S5. The ferrites exhibit normal behaviour of dielectrics, wherein the dielectric constant decreases rapidly up to 1 kHz, followed by a gradual decrease from 1 kHz to 100 kHz and is nearly independent of frequency above 100 kHz [28]. Highest values of 55.31 is observed for composition, $x = 0.5$ (sintered at 1250 °C), while for mixed ferrite compositions ($0.1 < x < 0.4$) the dielectric constant values are observed in the range 0.057–42.1. These values are found to be 10^3 times lower than those reported for ferrites prepared using conventional ceramic methods [68,69]. Moreover, the dielectric constant values are comparable to those reported using the citrate precursor method [65]. This variation in the dielectric constant can be explained based on space charge polarization which is a result of the presence of higher conductivity phases (grains) in the insulating matrix (grain boundaries) of the dielectrics, causing localized accumulation of the charge [70,71]. Under the influence of externally applied field the electrons travel towards the grain boundaries through hopping and due to the high grain boundary resistance, they pile up to produce polarization. However, as the frequency of the applied field is increased, there is a phase lag between the moving electrons and the applied field making the electrons reverse the direction of the motion. Consequently, the probability of the electrons reaching the grain boundaries decrease and as a result, the polarization decreases. Therefore, the dielectric constant decreases with the increasing frequency of the applied field [72]. The frequency variation of the dielectric loss tangent (tan δ) of the ferrites sintered at 1200 °C (Fig. 7b) show a decrease with increasing frequency whereas those sintered at 1100 °C and 1150 °C [Fig. S6(a-b)] show an initial decrease followed by a resonance peak in the frequency range 100 kHz to 1 MHz. The dielectric losses are found to be very low (of the order 10^{-2}) in the MHz range for all the sintered compositions which are comparable to the reported values for the mixed Ni-Mn-Zn ferrites [63]. The initial decrease of tan δ is explained based on Koop's theory [71] while the resonance peak is due to the matching of the time period of the applied electric field with that of the corresponding relaxation phenomena. The resonance is due to the jump of an ion between more than one of its equilibrium positions [71] and it occurs when an ion has more than one equilibrium position of equal potential energies, separated by the potential barrier. The jump probability between the equilibrium positions is the same and depending on this probability, the ion exchanges position between the two states with frequency, called the natural frequency of jump. When an external alternating electric field that matches the natural oscillation frequency is applied, maximum electrical energy is transferred to the oscillating ions and power loss shoots up, resulting in the resonance [71]. When the larger Mn^{2+} ions ($r = 0.82$ Å) are substituted for the smaller Ni^{2+} ions ($r = 0.70$ Å) in a mixed Ni-Mn-Zn ferrite system, the substituted Mn^{2+} ions push apart the neighbouring ions which increase the equilibrium positions of the next neighbouring ions. Consequently, the jump probability between the two next neighbouring positions increases. This results in an increase in the jump frequency and hence a shift in the resonance peak towards a higher frequency [71].

The thermal variation of the dielectric constant and dielectric loss tangent (at 100 Hz) of the ferrites sintered at 1250 °C are shown in Fig. 8a and b, respectively. The dielectric constant increases with increasing temperature at all the frequencies. The increase in the dielectric constant is very large (of the order 10^6) at lower frequencies (100 Hz), while at higher frequencies (10 MHz) the increase is small (up to 25) [73]. In general, the dielectric constant of any material is the resultant of its dipolar, electronic, ionic, and interfacial polarization [74]. At low frequencies, the temperature dependent dipolar and interfacial polarization plays an important role. The interfacial polarization increases with temperature due to the creation of crystal defects while the dipolar polarization decreases with an increase in temperature. The rapid increase in the dielectric constant with the temperature at low frequencies suggests that the effect of temperature is more pronounced on the interfacial polarization than on the dipolar polarization. While, at higher frequencies, electronic and ionic polarizations significantly contribute to the dielectric constant, but their temperature dependence is insignificant resulting in low value of dielectric constant [73]. For mixed Ni-Mn-Zn ferrite compositions ($0.1 < x < 0.4$), the dielectric constant exhibits increase with increase in sintering

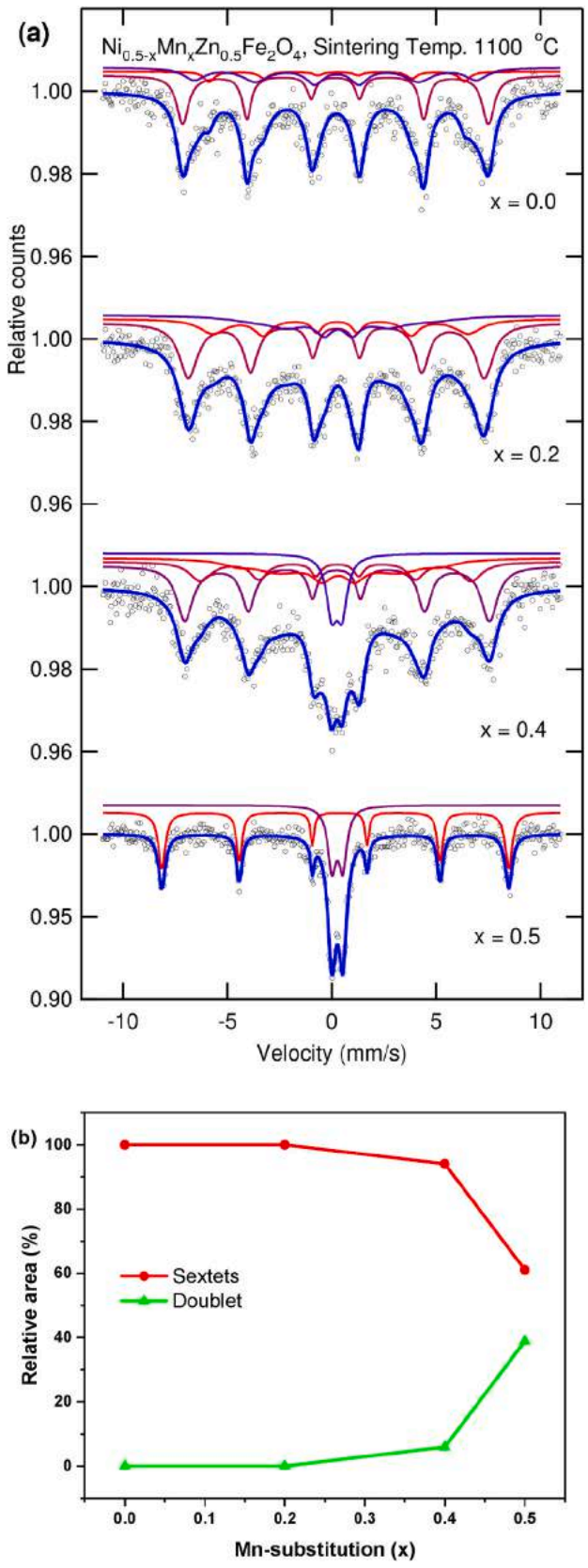

Fig. 5. (a). Mössbauer spectra recorded at room temperature of $Ni_{0.5-x}Mn_xZn_{0.5}Fe_2O_4$ (0.0, 0.2, 0.4, and 0.5) ferrites sintered in the air at temperatures 1100 °C. **(b)** Relative area of sextets and doublets with increasing the Mn content.

temperature up to 1150 °C, followed by a decrease at sintering temperature of 1200 °C and thereafter exhibits increase with further increase in the sintering temperature (1250 °C). For composition $x = 0.0$, the dielectric constant decreases with increase in the sintering temperature up to 1200 °C and exhibits a sharp increase at sintering temperature of 1250 °C. The dielectric constant is found to be relatively higher for the ferrites sintered at 1250 °C. This increase in the dielectric constant is ascribed to an increase in the grain size from 0.59 μm to 1.36 μm with increasing sintering temperature.

The thermal variation of dielectric loss tangent (tan δ) shows increase with increase in sintering temperature at all frequencies. This increase is large at lower frequencies while at a higher frequency region the increase is very small. The increase in the dielectric loss is due to an increase in interfacial polarization with the increase in temperature. The energy losses in the dielectrics result from the electrical conductivity and the relaxation effects related to the dipole orientation. With the increase in temperature, the losses due to dipole orientation decreases while those due to electric conductivity increases [74]. The increase in dielectric loss observed for the sintered ferrites with increasing temperature suggest that the losses due to electric conductivity are dominant over those due to relaxation effects. The dielectric constant and dielectric loss are found to be relatively lower for all the sintered compositions [Table S5] which further confirms the better stoichiometry, homogeneity, and very low zinc losses in ferrites processed using the precursor combustion method.

3.7. Initial permeability

The room temperature frequency variation of initial permeability (μ_i) and loss factor of $Ni_{0.5-x}Mn_xZn_{0.5}Fe_2O_4$ ($0.0 < x < 0.5$) ferrites sintered at 1250 °C are depicted in Fig. 9a and b, respectively. The μi decreases gradually with increasing frequency up to about 6 MHz and thereafter exhibits an increase up to 10 MHz (except for composition, $x = 0.5$). In ferrite materials, the μ_i originates from domain wall displacement and the decrease in the μ_i with frequency is due to phase lag between the applied field and the domain wall displacement. The ferrites generally exhibit two resonance peaks one due to domain wall oscillations [75] at lower frequencies (1 MHz–100 MHz) and the other due to Larmor precession of electron spins at higher frequencies (~1 GHz) [76]. The increase in the μ_i above 10 MHz is attributed to the onset of the resonance due to domain wall oscillations [74,75]. The μ_i values at 1 kHz are found to be in the range of 25.7–621.3 [Table S5] which are higher than the reported [39]. The μ_i initially increases with increasing Mn substitution (up to $x = 0.2$) and decreases with further increase in the Mn content. The μ_i depends on many factors such as composition, stoichiometry, crystal anisotropy, impurities, grain diameter, and porosity. The value of μ_i is found to increase with the increase in grain size and stoichiometry [77,78], and decreases with an increase in the porosity and magnetocrystalline anisotropy [79,80]. Since the domain wall motion is the major contributor for the μ_i, the number of domain walls increases with an increase in the grain size. The initial increase in μ_i (up to $x = 0.2$) suggests that the effects of an increase in grain size and decrease in magnetocrystalline anisotropy (with decreasing Ni content) play a dominant role [81] while, the decrease in μ_i for higher Mn substitution ($x > 0.2$) suggests that the effect of an increase in the porosity is dominant over the increasing grain size. The loss factor is found to decrease with the increasing frequency. The loss is due to the lag in the motion of domain walls to the applied alternating magnetic field and can be attributed to imperfections in the lattice [82]. The room temperature loss factor of the ferrites sintered at 1250 °C are found in the range 100 to 10^{-3}.

The thermal variation of initial permeability and loss factor of ferrites sintered at 1200 °C are depicted in Fig. 10a and b respectively. The initial permeability increases gradually with increase in the temperature reaching a peak value near the Curie temperature (Tc) and then exhibits a sharp fall. These sharp drop in μ_i at Tc indicate the complete phase

Table 2
Room temperature Mössbauer effect parameters: isomer shift 'δ', quadrupole splitting 'Δ', hyperfine field 'H_{hf}', relative Area 'R_A' and outer line width 'Γ' of $Ni_{0.5-x}Mn_xZn_{0.5}Fe_2O_4$ ($x = 0.0 \leq 0.5$) ferrites sintered at 1100 °C/1h.

Sample Composition (x)	Iron Sites	Relative area (R_A) %	Outer Line width, (Γ) mm/s (±0.02)	Isomer shift, (δ) mm/s (±0.01)	Quadrupole splitting, (Δ) mm/s (±0.02)	Hyperfine field (H_{hf}) Tesla (±0.1)	Fitting quality (χ^2)
0.0	Sextet A	36.6	0.701	0.282	0.006	45.4	0.97
	Sextet B	7.9	0.587	0.376	−0.06	37.9	
	Sextet C	55.4	1.232	0.315	−0.07	41.9	
0.2	Sextet A	47.2	1.016	0.330	−0.001	44.1	0.96
	Sextet B	37.0	1.291	0.534	0.268	31.8	
	Sextet C	15.8	1.143	0.420	0.136	39.1	
0.4	Sextet A	32.5	0.945	0.348	0.027	45.2	0.89
	Sextet B	45.3	1.595	0.454	0.061	30.6	
	Sextet C	16.2	1.254	0.337	−0.07	40.2	
	Doublet	5.9	0.606	0.352	0.489	–	
0.5							0.96
	Sextet A	61.1	0.406	0.373	−0.212	51.5	
	Doublet	38.9	0.472	0.376	0.517	–	

*Isomer shift values are relative to α-Fe metal foil (δ = 0.0 mm s^{-1}).

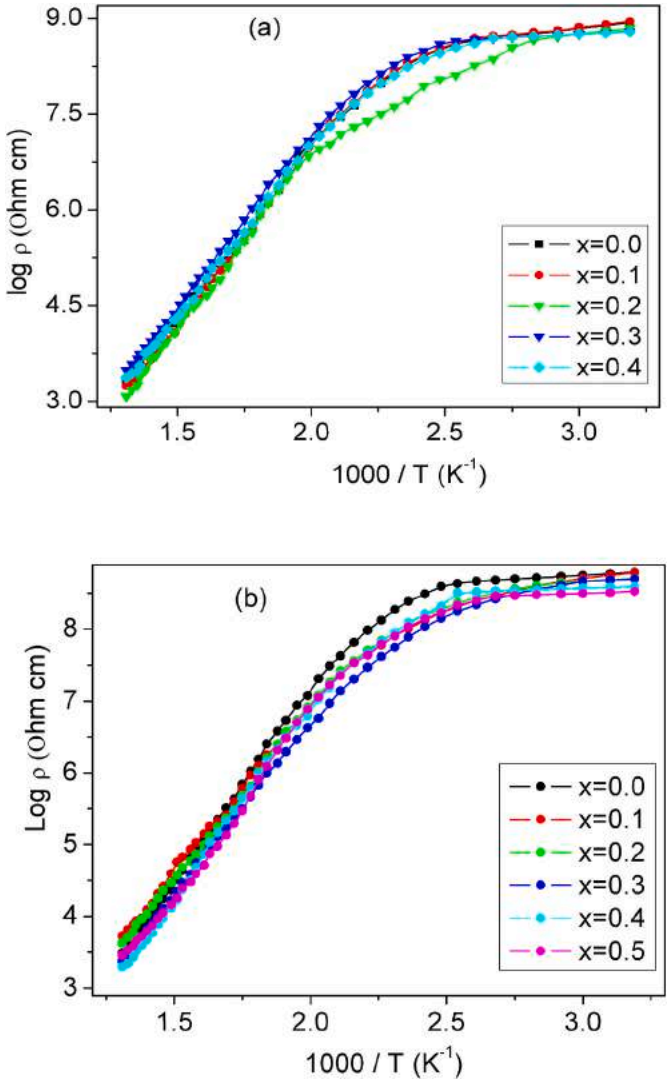

Fig. 6. (a–b). Thermal variation of log ρ against 1000/T for $Ni_{0.5-x}Mn_xZn_{0.5}Fe_2O_4$ ($0.0 < x < 0.5$) ferrites, sintered at (a) 1100 °C, and (b) 1250 °C.

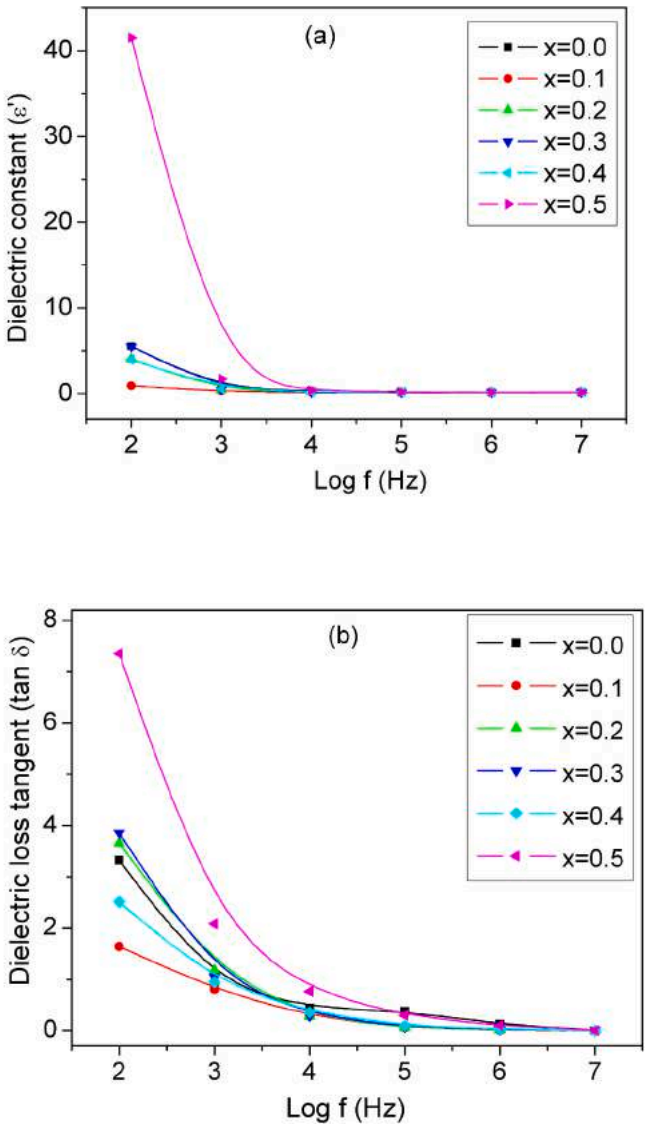

Fig. 7. (a–b). Dielectric constant (a) and dielectric loss (b) of $Ni_{0.5-x}Mn_xZn_{0.5}Fe_2O_4$ ($0.0 < x < 0.5$) ferrites sintered at 1200 °C.

formation and better homogeneity of samples [83]. The μ_i increases with increase in the sintering temperature from 1100 °C to 1200 °C (except for $x = 0.4$) and exhibits decrease at the sintering temperature of 1250 °C [Table S5]. This increase in μ_i is attributed to the increase in density and grain size. As the grain size increases the number of domain walls in each grain increases and as the movement of domain walls

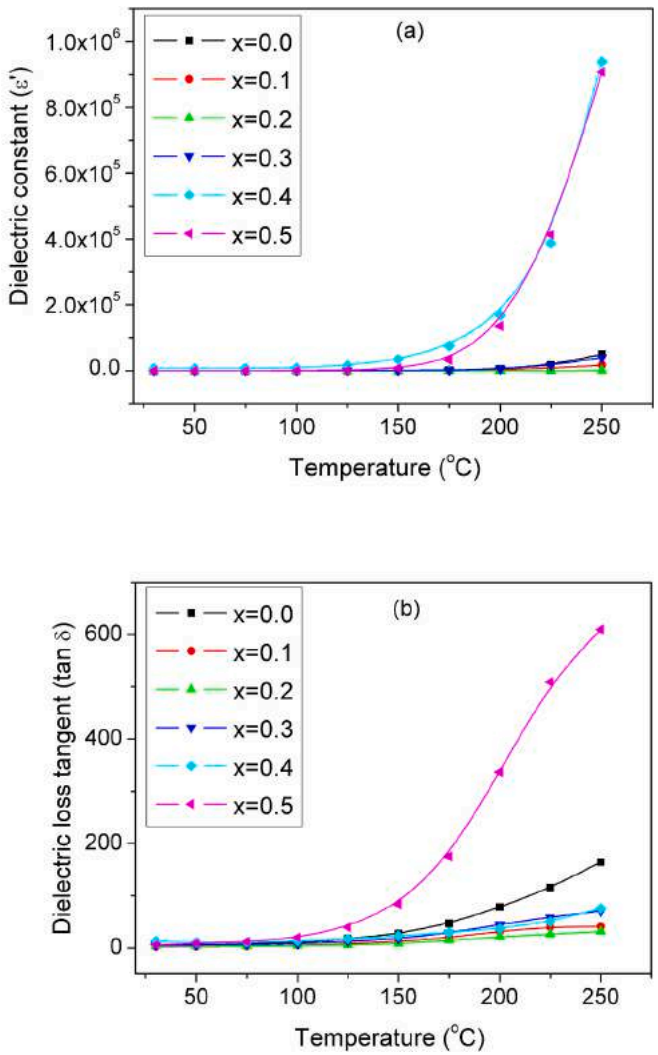

Fig. 8. (a–b). Variation of (a) dielectric constant and (b) dielectric loss against temperature at 100 Hz for $Ni_{0.5-x}Mn_xZn_{0.5}Fe_2O_4$ ($0.0 < x < 0.5$) ferrites sintered at 1250 °C.

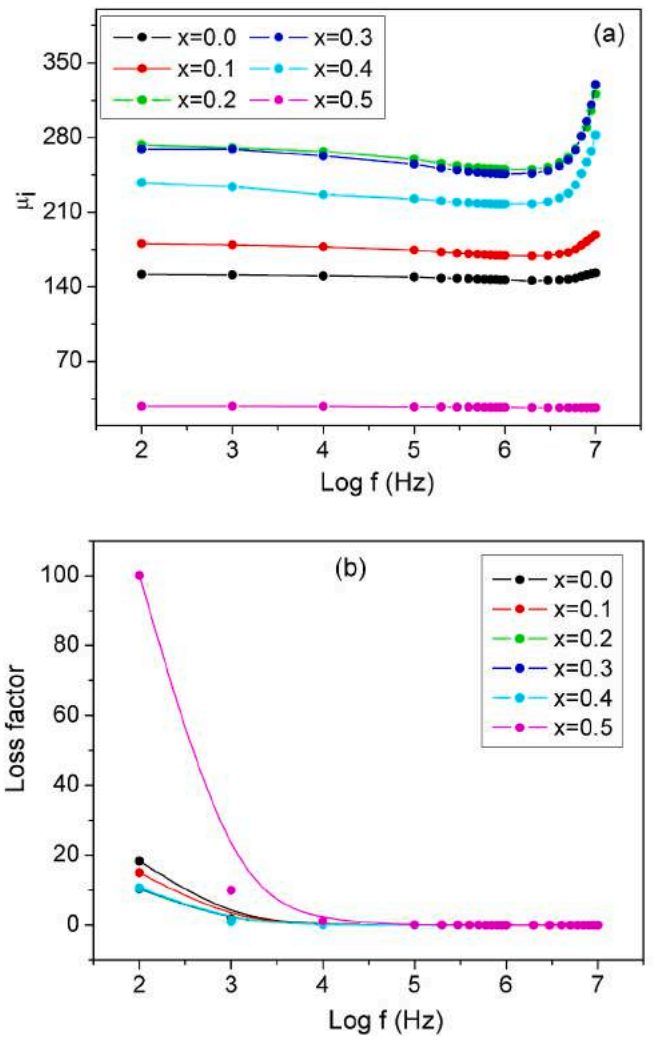

Fig. 9. (a–b). Variation of (a) initial permeability and (b) loss factor against log f for $Ni_{0.5-x}Mn_xZn_{0.5}Fe_2O_4$ ($0.0 < x < 0.5$) ferrites sintered at 1200 °C.

determines the μ_i, the increase in the number of domain walls increases the μ_i [84,85]. Further, the magnetocrystalline anisotropy decreases with an increase in sintering temperature and therefore enhances the μ_i [84,86]. However, at higher sintering temperatures (<1200 °C) there is an increase in the intragranular pores trapped in the grains. These pores act as pinning centers for the domain wall movement consequently, domain wall movement is restricted and the μ_i decreases [85]. The loss factor remains nearly constant from room temperature till Tc and exhibits a sharp increase at the Tc. Accordingly, the Tc of all sintered compositions were determined from the thermal variation of μ_i and loss factor.

3.8. Curie temperature

The variation of Tc with Mn substitution in the ferrites sintered at 1200 °C is shown in Fig. 11 and Tc determined from the thermal variation of dc resistivity and μ_i are listed in Table S6. The Tc are found to decrease with an increase in Mn substitution. This decrease in the Tc is attributed to the decreasing *A*-B interaction resulting from the replacement of Fe^{3+} ions by Mn^{2+} ions at the tetrahedral *(A)* sites. As the concentration of Mn^{2+} ions is increased, the ferromagnetic Fe^{3+} ions at the *A* sites are displaced by the diamagnetic Mn^{2+} ions. This displacement decreases the density of the magnetic ions at the A sites and hence the magnetic moment of the *A*-B sublattice decreases resulting in the weakening of *A*-B exchange interactions. Secondly, the lattice parameter increases with increase in the Mn substitution as a result the distance between the cations increases, which leads to a further decrease in *A*-B interactions. Since the Tc is determined by an overall strength of the *A*-B exchange interactions, the weakening of the $Fe^{3+}{}_{(A)}$–O^{2-}–$Fe^{3+}{}_{(B)}$ interaction results in the decrease in the Tc [40]. Moreover, the exchange integral 'J' between Fe^{3+} ions and Ni^{2+} ions ($J = -24$ K) is greater than that between Fe^{3+} ions and Mn^{2+} ions ($J = -19.1$ K) which causes a further decrease in *A*-B interactions [87] and hence the Tc. The Tc of all sintered compositions are found increase with an increase in the sintering temperature up to 1200 °C and exhibit a decrease in the samples sintered at 1250 °C.

4. Conclusions

Ni-Mn-Zn ferrite compositions processed using the precursor combustion method are found to exhibit improved electrical and initial permeability behaviour. Monophasic mixed Ni-Mn-Zn ferrites can be obtained at the lower sintering temperature of 1100 °C. Mn substitution is found to increase the lattice parameter Ni-Zn ferrites as revealed by the XRD measurement. The EDS measurement has confirmed very low zinc losses in all the sintered compositions. The room temperature dc resistivity of the order 10^8-10^7 Ω cm is found to be appreciable higher than those obtained for ferrites processed by the conventional ceramic

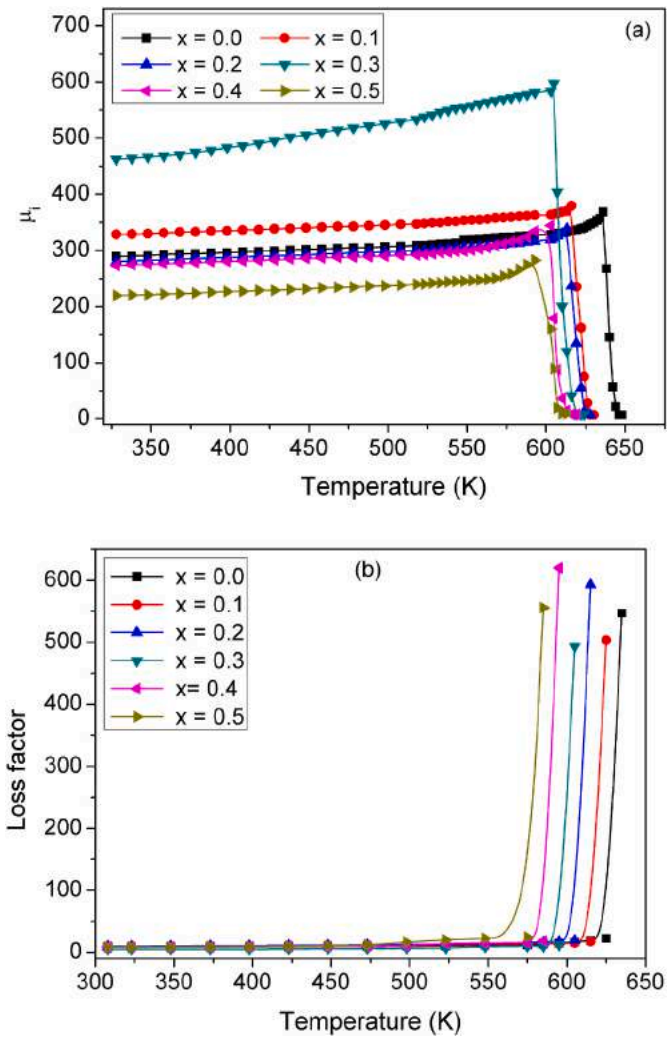

Fig. 10. (a–b). Variation of (a) initial permeability and (b) loss factor against temperature at 1 KHz for $Ni_{0.5-x}Mn_xZn_{0.5}Fe_2O_4$ ($0.0 < x < 0.5$) ferrites sintered at 1200 °C.

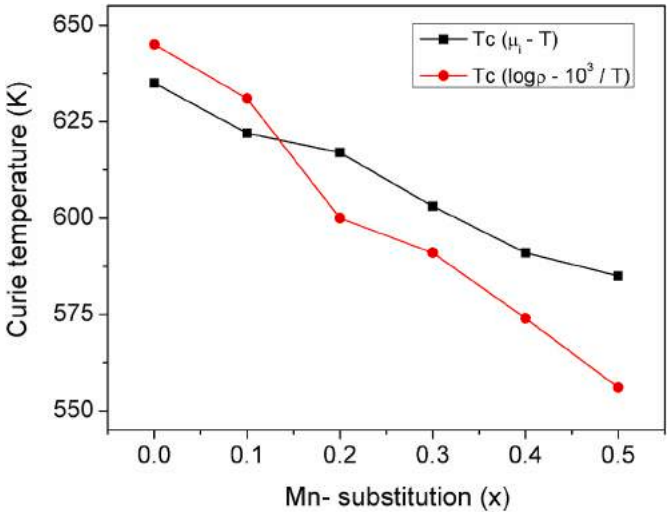

Fig. 11. Variation of Curie temperature with Mn substitution for $Ni_{0.5-x}Mn_xZn_{0.5}Fe_2O_4$ ($0.0 < x < 0.5$) ferrites sintered at 1200 °C.

method. The dielectric constant values in the range 0.057–55.21 and appreciably lower values of dielectric losses (10^{-2}) imply better stoichiometry and homogeneity in all the sintered ferrites. Highest initial permeability value of 621.3 is observed for the composition, $x = 0.2$ sintered at 1200 °C. The ferrites with the lower dielectric losses, higher resistivity and initial permeability are suitable for high frequency device applications.

CRediT authorship contribution statement

U.B. Gawas: Conceptualization, Software, Validation, Investigation, Writing – original draft. **V.M.S. Verenkar:** Conceptualization, Methodology, Resources, Writing – review & editing, Supervision, Project administration. **V.T. Vader:** Data curation. **Anil Jain:** Software, Investigation. **Sher Singh Meena:** Software, Investigation, Writing – review & editing.

Declaration of competing interest

The authors declare that they have no known financial interests or personal relationships that could have appeared to influence the work reported in this paper.

Acknowledgment

One of the authors, UBG would like to thank the Directorate of Higher Education, Government of Goa for financial assistance wide Grant No. 9/328/2026-17/SPSE-PP/DHE/3607. We would like to thank DST, New Delhi for financial support through Nano Mission Project, No. SR/NM/NS/-86/2009 and also under FIST. Also, we would like to acknowledge, Mr. V. D. Khedekar, Principal Technical Officer, and Mr. Girish Prabhu, Senior Technical Officer, CSIR-National Institute of Oceanography, Dona Paula-Goa for providing SEM and XRD data of ferrite samples, respectively. We thank the University Science Instrumentation Center (USIC), Goa-University for providing EDX measurements.

Appendix A. Supplementary data

Supplementary data to this article can be found online at https://doi.org/10.1016/j.matchemphys.2021.125250.

References

[1] R. Hao, R. Xing, Z. Xu, Y. Hou, S. Gao, S. Sun, Synthesis, functionalization, and biomedical applications of multifunctional magnetic nanoparticles, Adv. Mater. (2010), https://doi.org/10.1002/adma.201000260.
[2] Y. Liu, X. Liu, X. Wang, Synthesis and microwave absorption properties of Ni-Zn-Mn spinel ferrites, Adv. Appl. Ceram. (2015), https://doi.org/10.1179/1743676114Y.0000000194.
[3] Y. Cao, H. Qin, X. Niu, D. Jia, Simple solid-state chemical synthesis and gas-sensing properties of spinel ferrite materials with different morphologies, Ceram. Int. (2016), https://doi.org/10.1016/j.ceramint.2016.03.184.
[4] Y. Wang, X. Gao, X. Wu, W. Zhang, Q. Wang, C. Luo, Hierarchical $ZnFe_2O_4$@RGO@CuS composite: strong absorption and wide-frequency absorption properties, Ceram. Int. 44 (2018), https://doi.org/10.1016/j.ceramint.2018.02.220.
[5] J. Pei, Z. Wang, Y. Gao, H. Zhang, Structure and magnetic properties of $Ni_{0.5}Zn_{0.5}Mn_{0.5-x}Mo_xFe_{1.5}O_4$ ferrites prepared by the sol-gel auto-combustion method, Curr. Appl. Phys. (2019), https://doi.org/10.1016/j.cap.2019.01.013.
[6] S. Atiq, M. Majeed, A. Ahmad, S. K Abbas, M. Saleem, S. Riaz, S. Naseem, Synthesis and investigation of structural, morphological, magnetic, dielectric and impedance spectroscopic characteristics of Ni-Zn ferrite nanoparticles, Ceram. Int. (2017), https://doi.org/10.1016/j.ceramint.2016.11.046.
[7] P. Priyadharsini, A. Pradeep, P.S. Rao, G. Chandrasekaran, Structural, spectroscopic and magnetic study of nanocrystalline Ni-Zn ferrites, Mater. Chem. Phys. (2009), https://doi.org/10.1016/j.matchemphys.2009.03.011.
[8] J. Topfer, A. Angermann, Nanocrystalline magnetite, and Mn-Zn ferrite particles via polyol process: synthesis and magnetic properties, Mater. Chem. Phys. (2011), https://doi.org/10.1016/j.matchemphys.2011.04.025.
[9] Y. Ying, Y. Gong, D. Li, W. Li, J. Yu, L. Jiang, S. Che, Effect of MoO_3 addition on the magnetic properties and complex impedance of Mn-Zn ferrites with high Bs and

high initial permeability, J. Supercond. Nov. Magnetism (2017), https://doi.org/10.1007/s10948-017-4002-z.
[10] Y. Liu, S. He, Development of high DC-bias Mn-Zn ferrite working at a frequency higher than 3MHz, J. Alloys Compd. (2010), https://doi.org/10.1016/j.jallcom.2009.09.099.
[11] S.H. Keluskar, R.B. Tangsali, G.K. Naik, J.S. Budkuley, High permeability of low loss Mn-Zn ferrite obtained by sintering nanoparticle Mn-Zn ferrite, J. Magn. Magn Mater. (2006), https://doi.org/10.1016/j.jmmm.2006.01.018.
[12] Z. Maleknejad, Kh Gheisari, A. Honarbakhsh Raouf, Structure, microstructure, magnetic, electromagnetic, and dielectric properties of nanostructured Mn-Zn Ferrite synthesized by microwave-induced urea-nitrate process, J. Supercond. Nov. Magnetism (2016), https://doi.org/10.1007/s10948-016-3572-5.
[13] S. Hallynck, G. Pourroy, S. Vilminot, P.M. Jacquart, D. Autissier, N. Vukadinovic, H. Pascard, Synthesis of high aspect ratio of $Ni_{0.5}Zn_{0.5}Fe_2O_4$ platelets for electromagnetic devices, Solid State Sci. (2006), https://doi.org/10.1016/j.solidstatesciences.2005.10.007.
[14] I.H. Gul, W. Ahmed, A. Maqsood, Electrical and magnetic characterization of nanocrystalline Ni-Zn ferrite synthesis by co-precipitation route, J. Magn. Magn Mater. (2008), https://doi.org/10.1016/j.jmmm.2007.05.032.
[15] S. Zahi, A.R. Daud, M. Hashim, A comparative study of nickel-zinc ferrites by sol-gel route and solid-state reaction, Mater. Chem. Phys. (2007), https://doi.org/10.1016/j.matchemphys.2007.06.031.
[16] C. Venkataraju, G. Sathishkumar, K. Sivakumar, Effect of cation distribution on the structural and magnetic properties of nickel substituted nano structured Mn-Zn ferrites prepared by co-precipitation method, J. Magn. Magn Mater. (2010), https://doi.org/10.1016/j.jmmm.2009.08.043.
[17] C. Venkataraju, G. Sathishkumar, K. Sivakumar, Effect of nickel on the electrical properties of nanostructured MnZn ferrite, J. Alloys Compd. (2010), https://doi.org/10.1016/j.jallcom.2010.03.160.
[18] T.S. Kuru, M. Kuru, S. Bagci, Dielectric, humidity behavior and conductivity mechanism of $Mn_{0.2}Ni_{0.3}Zn_{0.5}Fe_2O_4$ ferrite prepared by co-precipitation method, J. Mater. Sci. Mater. Electron. (2018), https://doi.org/10.1007/s10854-018-9807-4.
[19] A.K.M. Akther Hossain, T.S. Biswas, S.T. Mahmud, T. Yanagida, H. Tanaka, T. Kawai, Enhancement of initial permeability due to Mn substitution in polycrystalline $Ni_{0.50-x}Mn_xZn_{0.50}Fe_2O_4$, J. Magn. Magn Mater. (2009), https://doi.org/10.1016/j.jmmm.2011.02.03.
[20] K. Jalaiah, K.V. Babu, Structural, magnetic and electrical properties of nickel doped Mn-Zn spinel ferrite synthesized by sol-gel method, J. Magn. Magn Mater. (2017), https://doi.org/10.1016/j.jmmm.2016.09.114.
[21] U.B. Gawas, M.M. Kothawale, Rajesh Pednekar, S.S. Meena, N.K. Prasad, S.K. Alla, Investigation of resistivity, magnetic susceptibility and dielectric properties of nanocrystalline Ni-Mn-Zn ferrites, J. Supercond. Nov. Magnetism (2017), https://doi.org/10.1007/s10948-016-3927-y.
[22] U.B. Gawas, V.M.S. Verenkar, S.R. Barman, S.S. Meena, Pramod Bhatt, Synthesis of nanosize and sintered $Mn_{0.3}Ni_{0.3}Zn_{0.4}Fe_2O_4$ ferrite and their structural and dielectric studies, J. Alloys Compd. (2013), https://doi.org/10.1016/j.jallcom.2012.12.054.
[23] P.P.G. Dessai, V.M.S. Verenkar, Synthesis and characterization of $Ni_{0.7-x}Mn_xZn_{0.3}Fe_2(C_4H_2O_4)_3{\cdot}6N_2H_4$ (x = 0.1-0.6): a precursor for the synthesis of nickel-manganese-zinc Ferrites, J. Therm. Anal. Calorim. (2020), https://doi.org/10.1007/s10973-020-09485-2.
[24] U.B. Gawas, V.M.S. Verenkar, Synthesis, thermo-analytical and IR spectral studies of hydrazinated mixed metal carboxylates: a single source precursor to nanosize mixed metal oxides, Thermochim. Acta (2013), https://doi.org/10.1016/j.tca.2013.01.017.
[25] U.B. Gawas, V.M.S. Verenkar, S.S. Meena, Pramod Bhatt, Influence of Mn substitution on Mössbauer and magnetic properties of Ni-Zn Ferrites nanoparticles, J. Supercond. Nov. Magnetism (2017), https://doi.org/10.1007/s10948-017-4149-7B.
[26] M.I. Mendelson, Average grain size in polycrystalline ceramics, J. Am. Ceram. Soc. (1969), https://doi.org/10.1111/j.1151-2916.1969.tb11975.x.
[27] Lorentz, D. Ihle, Calculation of the electrical conductivity above and below the Verwey transition in magnetite, Phys. Status Solidi B (1975), https://doi.org/10.1002/pssb.2220690216.
[28] D. Ravinder, K. Vijaya Kumar, Dielectric behaviour of erbium substituted Mn-Zn ferrites, Bull. Mater. Sci. (2001), https://doi.org/10.1007/BF02706722.
[29] A. Verma, T.C. Geol, R.G. Mendiratta, P. Kishan, Magnetic properties of nickel-zinc ferrites prepared by the citrate precursor method, J. Magn. Magn Mater. (2000), https://doi.org/10.1016/S0304-8853(99)00585-5.
[30] M. Hashim, S.S. Meena, R.K. Kotnala, S.E. Shirsath, P. Bhatt, S. Kumar, E. Şentürk, R. Kumar, N. Gupta, Exploring the structural, Mössbauer and dielectric properties of Co2+ incorporated Mg0.5Zn0.5-xCoxFe2O4 nanocrystalline ferrite, J. Magn. Magn Mater. (2014), https://doi.org/10.1016/j.jmmm.2014.01.047.
[31] S.P. Yadav, S.S. Shinde, P. Bhatt, S.S. Meena, K.Y. Rajpure, Distribution of cations in Co1-xMnxFe2O4 using XRD, magnetization and Mössbauer spectroscopy, J. Alloys Compd. (2015), https://doi.org/10.1016/j.jallcom.2015.05.270.
[32] M. Deepty, Ch Srinivas, E. Ranjith Kumar, N. Krisha Mohan, C.L. Prajapat, T. V. Chandrasekhar Rao, S.S. Meena, A.K. Verma, D.L. Sastry, XRD, EDX, FTIR and ESR spectroscopic studies of co-precipitated Mn-substituted Zn-ferrite nanoparticles, Ceram. Int. (2019), https://doi.org/10.1016/j.ceramint.2019.01.029.
[33] K. Mohan, Y.C. Venudhar, Far-infrared spectra of lithium-cobalt mixed ferrites, J. Mater. Sci. Lett. (1999), https://doi.org/10.1023/A:1006604805937.
[34] R.D. Waldron, Infrared spectra of ferrites, Phys. Rev. (1955), https://doi.org/10.1103/PhysRev.99.1727.
[35] P.P. Hankare, R.P. Patil, K.M. Garadkar, R. Sasikala, B.K. Chougule, Synthesis, dielectric behavior and impedance measurement studies of Cr-substituted Zn-Mn ferrites, Mater. Res. Bull. (2011), https://doi.org/10.1016/j.materresbull.2010.11.026.
[36] Q.M. Wei, J.B. Li, Y.J. Chen, Cation distribution and infrared properties of $Ni_xMn_{1-x}Fe_2O_4$ ferrites, J. Mater. Sci. (2001), https://doi.org/10.1023/A:1012473207424.
[37] K.A. Mohammed, A.D. Al-Rawas, A.M. Gismelseed, A. Sellai, H.M. Widatallah, A. Yousif, M.E. Elzain, M. Shongwe, Physica B, Infrared and Structural Studies of $Mg_{1-x}Zn_xFe_2O_4$ Ferrites, 2012, https://doi.org/10.1016/j.physb.2011.12.097.
[38] N.M. Deraz, Fabrication, characterization and magnetic behaviour of alumina-doped zinc ferrite nanoparticles, J. Anal. Appl. Pyrol. (2011), https://doi.org/10.1016/j.jaap.2011.01.002.
[39] S.E. Shirsath, B.G. Toksha, R.H. Kadam, S.M. Patange, D.R. Mane, G.S. Jangam, A. Ghasemi, Doping effect of Mn2+ on the magnetic behavior in Ni-Zn ferrite nanoparticles prepared by sol-gel auto-combustion, J. Phys. Chem. Solid. (2010), https://doi.org/10.1016/j.jpcs.2010.08.016.
[40] T.T. Srinivasan, C.M. Srivastava, N. Venkatramani, M.J. Patni, Infrared absorptions in spinel ferrites, Bull. Mater. Sci. (1984), https://doi.org/10.1007/BF02743958.
[41] O.S. Josyulu, J. Sobhanadri, The far-infrared spectra of some mixed cobalt zinc and magnesium zinc ferrites, Phys. Status Solidi (1981), https://doi.org/10.1002/pssa.2210650209.
[42] A.M. Shaikh, S.A. Jadhav, S.C. Watawe, B.K. Chougule, Infrared spectral studies of Zn substituted Li-Mg ferrites, Mater. Lett. (2000), https://doi.org/10.1016/S0167-577X(00)00025-2.
[43] A. Alarifi, N.M. Deraz, S. Shaban, Structural, morphological and magnetic properties of $NiFe_2O_4$ nano-particles, J. Alloys Compd. (2009), https://doi.org/10.1016/j.jallcom.2009.06.192.
[44] G. Chandrasekaran, S. Selvandan, K. Manivannane, Electrical and FTIR studies on Al substituted Mn-Zn mixed ferrites, J. Mater. Sci. Mater. Electron. (2004), https://doi.org/10.1023/A:1026276501072.
[45] M.F. Yan, D. Johnson, Impurity-induced exaggerated grain growth in Mn-Zn ferrites, J. Am. Ceram. Soc. (1978), https://doi.org/10.1111/j.1151-2916.1978tb09325.x.
[46] G.F. Dionne, R.G. West, Magnetic and dielectric properties of the spinel ferrite system $Ni_{0.65}Zn_{0.35}Fe_{2-x}Mn_xO_4$, J. Appl. Phys. (1987), https://doi.org/10.1063/1.338623.
[47] M.H. Drofenik, S. Besenicar, Reexamination of the grain size/permeability relation in high permeability Mn-Zn ferrites, Am. Ceram. Soc. Bull. 65 (4) (1986) 656–659.
[48] M. Siddique, N.M. Butt, M. Shafi, T. Abbas, Misbah-ul-Islam, Cation distribution in Ni-substituted Mn-ferrites by Mössbauer technique, J. Radioanal. Nucl. Chem. (2003), https://doi.org/10.1023/b:jrnc.0000011746.68066.f5.
[49] S.S. Shinde, S.S. Meena, S.M. Yusuf, K.Y. Rajpure, Mössbauer, Raman, and magnetoresistance study of aluminum-based iron oxide thin films, J. Phys. Chem. C (2011), https://doi.org/10.1021/jp111922m.
[50] K. Sharma, S.S. Meena, S. Saxena, S.M. Yusuf, A. Srinivasan, G.P. Kothiyal, Structural and magnetic properties of glass-ceramics containing silver and iron oxide, Mater. Chem. Phys. (2012), https://doi.org/10.1016/j.matchemphys.2011.12.085.
[51] K. Sharma, S.S. Meena, C.L. Prajapat, S. Bhattacharya, Jagannath, M.R. Singh, S. M. Yusuf, G.P. Kothiyal, Preparation and study of magnetic properties of silico phosphate glass and glass-ceramics having iron and zinc oxide, J. Magn. Magn Mater. (2009), https://doi.org/10.1016/j.jmmm.2009.07.047.
[52] K. Sharma, A. Dixit, Sher Singh, Jagannath, S. Bhattacharya, C.L. Prajapat, P. K. Sharma, S.M. Yusuf, A.K. Tyagi, G.P. Kothiyal, Preparation and studies on surface modifications of calcium-silico-phosphate ferrimagnetic glass-ceramics in simulated body fluid, Mater. Sci. Eng. C (2009), https://doi.org/10.1016/j.msec.2009.05.009.
[53] S.G. Gawas, S.S. Meena, P. Bhatt, V.M.S. Verenkar, Nanoscale-driven structural changes and associated superparamagnetism in magnetically diluted Ni-Zn ferrites, Mater. Chem. Front. (2016), https://doi.org/10.1039/C7QM00437K.
[54] T. Tatarchuk, I. Mironyuk, V. Kotsyubynsky, A. Shyichuk, M. Myslin, V. Boychuk, Structure, morphology and adsorption properties of titania shell immobilized onto cobalt ferrite nanoparticle core, J. Mol. Liq. (2020), https://doi.org/10.1016/j.molliq.2019.111757.
[55] M. Rosenberg, M. Velicescu, Relaxation processes in cobalt substituted Ni-Zn ferrites, J. Phys. Soc. Jpn. (1970), https://doi.org/10.1143/JPSJ.28.264.
[56] R. Manjula, V.R.K. Murthy, J. Sobhsanadri, Electrical conductivity and thermoelectric power measurements of some lithium titanium ferrites, J. Appl. Phys. (1986), https://doi.org/10.1063/1.336954.
[57] L. Radhapiyari, S. Phanjoubam, H.N.K. Sarma, C. Prakash, Electrical and magnetic studies of the spinel system $Li_{0.5+t}$ Cr_xSb_t $Fe_{2.5-x-2t}O_4$, J. Phys. D (1999), https://doi.org/10.1088/0022-3727/32/17/303.
[58] J. Smit, H.P. J Wijn, in: Ferrites, Philips Technical Library, Eindhoven, 1959, p. 149.
[59] A.K. Singh, A. Verma, O.P. Thakur, Chandra Prakash, T.C. Goel, R.G. Mendiratta, DC resistivity of Mn-Ni-Zn ferrites, Jpn. J. Appl. Phys. (2002), https://doi.org/10.1143/JJAP.41.5142.
[60] R.G. Gupta, R.G. Mendiratta, Hyperfine field in $Zn^{2+}{}_{0.3}Mn^{2+}{}_{0.7}Mn^{3+}Fe^{3+}{}_2O_4$, J. Appl. Phys. (1977), https://doi.org/10.1063/1.324063.
[61] F.K. Lotegering, Semiconduction and cation valencies in manganese ferrites, J. Phys. Chem. Solid. (1964), https://doi.org/10.1016/0022-3697(64)90165-9.
[62] W.D. Kingery, H.K. Bowen, P.R. Uhlmann, Introduction to Ceramics, Wiley, New Work, 1975, p. 904.
[63] K. Iwauchi, Dielectric properties of fine particles of Fe_3O_4 and some ferrites, Jpn. J. Appl. Phys. (1971), https://doi.org/10.1143/JJAP.10.1520.

[64] E.J.W. Verwey, J.M. De Boer, Cation arrangement in a few oxides with crystal structures of the spinel type, Rec. Trav. Chim. Phys. Bas. (1936), https://doi.org/10.1002/recl.19360550608.
[65] A.K. Singh, T.C. Goel, R.G. Mendiratta, O.P. Thakur, Chandra Prakash, Dielectric properties of Mn-substituted Ni-Zn ferrites, J. Appl. Phys. (2002), https://doi.org/10.1063/1.1470256.
[66] J.M. Brownlow, Preferential volatilization of cations from ferrites during sintering, J. Appl. Phys. (1958), https://doi.org/10.1063/1.1723140.
[67] H. Zhong, H. Zhang, Effects of different sintering temperature and Mn content on magnetic properties of NiZn ferrites, J. Magn. Magn Mater. (2004), https://doi.org/10.1016/j.jmmm.2004.05.029.
[68] M.A. El Hiti, Dielectric behaviour of Mg-Zn ferrites, J. Magn. Magn Mater. (1999), https://doi.org/10.1016/S0304-8853(98)00356-4.
[69] L. Radhapiyari, S. Phanjoubam, H.N.K. Sarma, C. Prakash, Influence of Co^{2+} on the electrical and magnetic properties of Li-Sb ferrites, Mater. Lett. (2000), https://doi.org/10.1016/S0167-577X(00)00003-3.
[70] R.V. Mangalaraja, S. Ananthakumar, P. Manohar, F.D. Gnanam, Dielectric behavior of Ni1−xZnxFe2O4 prepared by flash combustion technique, Mater. Lett. (2003), https://doi.org/10.1016/S0167-577X(02)00947-3.
[71] C.G. Koops, On the dispersion of resistivity and dielectric constant of some semiconductors at audiofrequencies, Phys. Rev. (1951), https://doi.org/10.1103/PhysRev.83.121.
[72] A.K. Singh, T.C. Goel, R.G. Mendiratta, Effect of manganese impurity on the conductivity, dielectric behavior and magnetic properties of $Ni_{0.3}Mn_xZn_{0.7-x}Fe_2O_4$, Jpn. J. Appl. Phys. (2003), https://doi.org/10.1143/JJAP.42.2690.
[73] P. Mathur, A. Thakur, M. Singh, Impact of processing and polarization on dielectric behavior of $Ni_xMn_{0.4-x}Zn_{0.6}Fe_2O_4$ spinel ferrites, Int. J. Mod. Phys. B (2009), https://doi.org/10.1142/S0217979209052212.
[74] L.L. Hench, J.K. West, Principles of Electronic Ceramics, John-Wiley, New York, 1990, p. 205.
[75] J. Chand, G. Kumar P. Kumar, S.K. Sharma, M. Knobel, M. Singh, Effect of Gd3+ doping on magnetic, electric and dielectric properties of MgGdxFe2−xO4 ferrites processed by solid state reaction technique, J. Alloys Compd. (2011), https://doi.org/10.1016/j.jallcom.2011.07.055.
[76] A. Verma, R. Chatterjee, Effect of zinc concentration on the structural, electrical and magnetic properties of mixed Mn-Zn and Ni-Zn Ferrites synthesized by the citrate precursor technique, J. Magn. Magn Mater. (2006), https://doi.org/10.1016/j.jmmm.2006.03.033.
[77] S.H. Kang, H.I. Yoo, The effect of nonstoichiometry (δ) on the magnetic properties of (Mg0.22Mn0.07Fe0.71)3−δO4 ferrite, J. Appl. Phys. 88 (2000), https://doi.org/10.1063/1.1312844.
[78] P.S. Anil Kumar, J.J. Shotri, C.E. Deshpande, S.K. Date, Systematic study of magnetic parameters of Ni-Zn ferrite synthesized by soft chemical approaches, J. Appl. Phys. (1997), https://doi.org/10.1063/1.365464.
[79] J.H. Nam, W.G. Hur, J.H. Oh, The effect of Mn substitution on the properties of NiCuZn ferrites, J. Appl. Phys. (1997), https://doi.org/10.1063/1.365466.
[80] A. Globus, M. Guyot, Wall displacement and bulging in magnetization mechanisms of the hysteresis loop, Phys. Status Solidi B (1972), https://doi.org/10.1002/pssb.2220520211.
[81] S. Chikazumi, S. Charap, in: Physics of Magnetism, John Wiley & Sons, New York, 1964, p. 140.
[82] B.S. Chauhan, R. Kumar, K.M. Jadhav, M. Singh, Magnetic study of substituted Mg-Mn ferrites synthesized by citrate precursor method, J. Magn. Magn Mater. (2004), https://doi.org/10.1016/j.jmmm.2004.04.133.
[83] A.A. Sattar, A.H. Wafik, K.M. El-Shokrofy, M.M. El-Tabey, Magnetic properties of Cu-Zn ferrites doped with rare earth oxides, Phys. Status Solidi A (1999), https://doi.org/10.1002/(SICI)1521-396X(199902)171:2.
[84] A.K. Singh, T.C. Goel, R.G. Mendirattaa, Magnetic properties of Mn-substituted Ni-Zn ferrites, J. Appl. Phys. (2002), https://doi.org/10.1063/1.1504493.
[85] T. Nakamura, Y. Okaro, Electromagnetic properties of Mn-Zn ferrite sintered ceramics, J. Appl. Phys. (1996), https://doi.org/10.1063/1.361482.
[86] D. Polder, Ferrite materials, Proc. Inst. Electr. Eng. (1950), https://doi.org/10.1049/pi-2.1950.0076.
[87] C.M. Srivastava, G. Srinivasan, N.G. Nanadikar, Exchange constants in spinel ferrites, Phys. Rev. B: Condens. Mater. (1979), https://doi.org/10.1103/PhysRevB.19.499.

Indian Journal of Chemistry
Vol. 61, February 2022, pp. 154-158

Potassium phosphate catalyzed highly efficient synthesis of structurally diverse thioethers at ambient temperature

Satish D Mitragotri*[a], Makarand A Kulkarni[b], Uday V Desai[c] & Prakash P Wadagaonkar[d]

[a] Department of Chemistry, Walchand College of Arts and Science, Solapur 413 006, India

[b] Instrumentation center, P. A. H. Solapur University, Solapur 413 255, India

[c] Department of Chemistry, Shivaji University, Kolhapur 416 004, India

[d] Polymer Science and Engineering Division, National Chemical Laboratory, Pune 411 008, India

E-mail: sdmitragotri@gmail.com

Received 27 May 2020; accepted (revised) 27 October 2021

Commercially available potassium phosphate has been demonstrated to be a highly efficient catalyst for the synthesis of thioethers employing two different routes *viz*. alkylation of thiols with alkyl/aralkyl halides and by Michael addition of thiols to conjugated alkenes.

Keywords: Potassium phosphate, thiols, thioethers, thia-Michael reaction, alkyl halides

Thioethers have emerged as an important class of organic compounds with useful applications as key intermediates in organic synthesis as well as bio-organic, medicinal and heterocyclic chemistry[1-3]. Amongst various available approaches for the synthesis of thioethers, base catalyzed nucleophilic displacement of halide ion by thiolate anion[4-7], Michael addition of thiol to conjugated alkenes[8-10], are the routinely preferred pathways. Additionally, deoxygenation of sulfoxides[15,16], Indium (I) iodide promoted addition of thiolate anion to styrene[17], intermolecular s-alkylation of thiol with alcohol[18,19] and transition metal catalyzed coupling of aryl halide with thiol[20,21] are a few other approaches of interest. Many of these reported protocols although furnish the desired thioethers in acceptable yields, a few of them are plagued with the use of expensive catalyst, elevated temperature, long reaction times, essentiality of non-ecofriendly or high boiling solvent as well as the formation of side products such as disulfides, sulfonium salts, *etc*. Although plethora of catalyst are available for the synthesis of thioethers, to the best of our knowledge there are no reports on the use of a single catalyst which could be useful in the synthesis of these molecules following two routinely preferred approaches[4-14]. Our interest in the synthesis of thioethers stems from the call for structurally diverse thioethers useful in our ongoing studies on controlled and chemoselective oxidation of thioethers. Such thioethers either being very expensive or not being available commercially, it was surmised that the development of a mild, greener and practically simple protocol for the synthesis of thioethers would be in tune with our continued interest in the development of new synthetic methodologies[22-26].

Result and Discussion

Over the past few years, commercially available, non-toxic and relatively less expensive potassium phosphate has emerged as a useful base catalyst[27,28]. We have earlier explored its utility in Knoevenagel as well as Claisen-Schmidt condensation[29,30], Henry reaction[31], Michael addition reaction[32] and in the synthesis of tetrahydrobenzo [b] pyrans[33]. In continuation of these studies herein we report the usefulness of potassium phosphate as a highly efficient catalyst in synthesis of thioethers following two different routes (Figure 1). As regards the first route involving the alkylation of thiols, it was surmised that, potassium phosphate being basic enough to deprotonate a variety of thiols (*p*Ka = 7-11)[28], the resulting thiolate anion on reaction with alkyl halide would easily furnish corresponding thioether by S_N pathway. Based upon this presumption, a model reaction was carried out at ambient temperature between thiophenol and benzyl bromide using potassium phosphate as a catalyst and dimethyl formamide as a dipolar aprotic solvent. The

desired thioether was obtained in quick time and excellent yield (30 min, 93%). With an aim to turn this initial success into a greener protocol, the reaction conditions were then optimized with respect to the choice of solvent as well as the amount of catalyst loading by performing a series of reactions using the same substrate combination. The results summarized in Table I clearly demonstrate the essentiality of 25 mol % potassium phosphate as a catalyst and ethanol as relatively less expensive and non toxic reaction medium for an optimum yield (93%) of benzyl phenyl sulfide (Table I). Under the established reaction conditions for thiophenol in hand, generality of the protocol was then investigated by reacting a series of aryl, aralkyl, cycloalkyl and alkyl thiols with a range of primary, secondary, allylic as well as propargylic bromide. In general, the reactions were smooth and furnished corresponding thioethers in high yields as well as purity (Table II). It is worth mentioning that, potassium phosphate-purged air combination has previously been used in oxidation of thiols to disulfides[28] however; we did not observe the formation of any disulfide to a detectable extent (tlc). This is possibly because, in the absence of purged air, rate of nucleophilic displacement of halide ion by thiolate anion is much faster than that for its oxidation to yield corresponding disulfide. While examining the scope of the present protocol it was noticed that, the reaction of thiophenol with 1, 2 – dibromoethane and that of ethane 1, 2-dithiol with benzyl bromide furnished corresponding dithioethers. (Entries h, i, Table II) It was further gratifying to note that the protocol developed was also applicable in chemoselective S *vs* O or N alkylation with the choice of 2-mercaptoethanol (2n) and 2-amino thiophenol (2o) or 2-mercatobenzimidazole (2q) as representative bifunctional thiols (Table II). Our major aim behind the present study was not alone to develop a method for the synthesis of simple thioethers but was to develop a practically simple protocol for the synthesis of thioethers bearing a variety of functional groups such as OH, -CN, -$CONH_2$, -COOR, *etc*. In this context, although we were successful in synthesizing a few thioethers of such variety (Entry 1c, 1f, 1n, Table II), higher cost of starting bromo compounds such as, bromoacetonitrile, bromoacetamide, bromoester, *etc*. was the major limiting factor in using this new protocol. To circumvent this limitation, it was then planned to extend our earlier experience

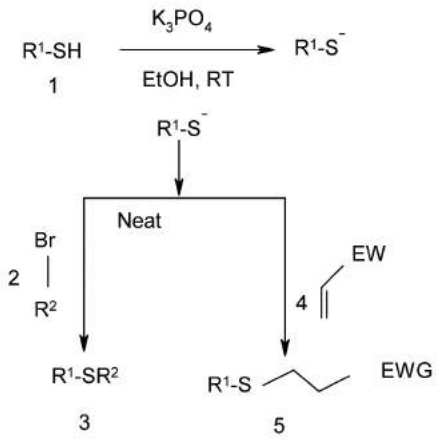

Figure 1 — Synthesis of thioethers following two different routes

Table I — Synthesis of benzyl phenyl sulphide under various conditions[a]

Entry	Catalyst (mol %)	Solvent	Yield (%)[b, c]
1	–	DMF/CH_3CN/EtOH	30[c]
2	5	DMF	40[c]
3	5	EtOH	35[c]
4	10	DMF	50[c]
5	10	EtOH	45[c]
6	20	DMF	80[c]
7	20	EtOH	76[c]
8	25	DMF	93[d]
9	25	EtOH	91[d]

[a] Reaction conditions: Thiophenol (2 mmol), benzyl bromide (2 mmol), catalyst, solvent, RT. [b] Isolated yield. [c] Yields after 6 h. [d] Yields after 3 h.

Table II — Potassium phosphate catalyzed synthesis of thioethers

Entry	R^1(1)	R^2(2)	Yield (%)[b]	Ref.
a	Ph	$PhCH_2Br$	91	7
b	Ph	4-F-$PhCH_2Cl$	84	–
c	Ph	Br-H_2CCO_2Et	86	11
d	Ph	H_2C=$CHCH_2Br$	93	6
e	Ph	$HCCCH_2Br$	75[d]	–
f	Ph	HOH_2CCH_2Br	87	52
g	Ph	$(CH_3)_2CHI$	90	4
h	Ph[e]	BrH_2CCH_2Br	89	52
i	HSH_2CCH_2SH	$PhCH_2Br$	93	52
j	n-C_4H_9	4-Cl-$PhCH_2Br$	79	7
k	4-Me Ph	$PhCH_2Br$	86	48
l	4-Cl Ph	4-NO_2-$PhCH_2Br$	93	7
m	Cyclohexane	$PhCH_2Br$	83	47
n	HSH_2CCH_2OH	4-F-$PhCH_2Cl$	84	–
o	2-Aminophenyl	$PhCH_2Br$	90	47
p	$PhCH_2$	$PhCH_2Br$	96	48
q	2-Mercaptobenzimidazole	$PhCH_2Br$	98	49

[a] Reaction conditions: Thiol (2 mmol), halide (2 mmol), potassium phosphate(25 mol %), ethanol (3 ml), RT. [b] Yield refers to pure isolated product. [c] 2 equ. [d] Solution of propargyl bromide in DCM was used. [e] Commercially available.

with Michael addition of thiols to enones[32], towards other Michael acceptors such as conjugated esters, amides, nitriles, *etc*. A survey of literature interestingly revealed that a variety of catalysts[34-40] have already been demonstrated to be useful in Michael addition of thiols to enones. However, only a few of them[38-40] have been used in reactions with the afore-mentioned Michael acceptors.

A representative reaction was then carried out between thiophenol, 1a and methyl acrylate, 4a, employing the reaction conditions established earlier for the preparation of benzyl phenyl sulfide. The desired thia-Michael addition product, 5aa, resulted very quickly (3-4 min) in almost quantitative yield. Further studies regarding the optimization of yield with respect to the catalyst loading revealed that, only 10 mol % potassium phosphate was sufficient to drive the reaction to completion under solvent-free condition with only a slight compromise in time (8–10 min *vs*. 3-4 min). So as to demonstrate the versatility of the protocol, representative alkyl, 1j, cycloalkyl, 1m and aralkyl thiol, 1p, were initially scrutinized with methyl acrylate and following success to these reactions, the protocol was extended towards addition of these thiols to other Michael acceptors (Table III). In all the cases studied, the resultant product in excellent yield (>95%) and purity (NMR) was isolated by simply stirring the reaction mixture with dichloromethane followed by filtration of concentrated organic extract through a short column of silica gel.

From a comparison view point, it is worthy to note that, synthesis of thioethers by SN pathway required slightly longer time (2-3 h) while the same following thia Michael pathways required very short reaction times. In context of the remarkable rate acceleration, on the basis of our earlier experience[32] we propose that, the primary role potassium phosphate in these C-S bond formation reactions is to deprotonate thiol to corresponding thiolate ion. In addition, due the presence of strong electron withdrawing counter anion *viz*. $[(PO_4)^{-3}]$, K^+ ion in potassium phosphate is sufficiently oxophilic and can form a strong coordinate bond with oxygen atom in enones as well as other Michael acceptors (Figure 2). Consequently, C-β in conjugated alkenes becomes enough electrophilic to accelerate the addition of thiolate anion (thia-Michael pathway).

Experimental Section

All chemicals were obtained from Lancaster or Aldrich Chemical Corporation and were used without purification. IR spectra were recorded on a Perkin-Elmer-793 instrument. ^{1}H and ^{13}C NMR spectra were recorded as $CDCl_3$ solutions on a Bruker Avance spectrometer at 300 and 75.4 MHz, respectively, using TMS as an internal standard. Chemical shifts are expressed in δ units. Elemental analysis was carried out using EURO EA analyzer.

Table III — Synthesis of thioethers by thia-Michael reaction

Entry	Thiol (1) R =	Alkene (4)	Product (5)	Yield (%)[Ref]
1	Ph *I*a	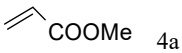 4a	5aa	94 [38]
2	n-Bu *I*j	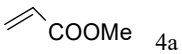 4a	5aj	98 [37]
3	Cyclohexyl *I*m	 4a	5am	94
4	$PhCH_2$ *I*p	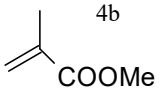 4b	5bp	96
5	Ph *I*a	 4c	5ca	95 [38]
6	n-Bu *I*j	 4c	5cj	97
7	Cyclohexyl *I*m	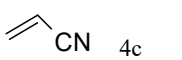 4c	5cm	93
8	Ph *I*a	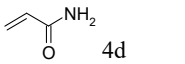 4d	5da	96 [38]
9	n-Bu *I*j	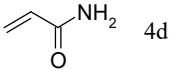 4d	5dj	94 [37]
10	Cyclohexyl *I*m	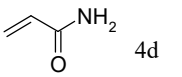 4d	5dm	92
11	$PhCH_2$ *I*p	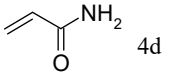 4d	5dp	92

Reaction conditions: Thiol (2 mmol), alpha beta unsaturated compound (2 mmol), potassium phosphate(25 mol %), RT, neat.

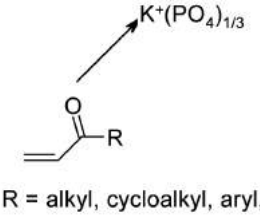

Figure 2 — Formation of coordinate bond between potassium ion and oxygen

Representative procedure

(a) Preparation of thioether by alkylation of thiol

To 0.55 g thiophenol (5 mmol) in 5 cm^3 ethanol was added 0. 26 g (25 mol %) of potassium

phosphate. After stirring the mixture for about 10 min, 0.60 g (5 mmol) allyl bromide was added. The stirring was continued and on completion of the reaction (tlc) water (20 cm^3) was added. The reaction mixture was extracted with 3×20 cm^3 of diethyl ether. The ether extract was washed with water (3×15 cm^3) and dried over anhydrous sodium sulfate. The removal of solvent followed by filtration of the resultant oil through a short column of silica gel afforded 0.730 g (93%) **2d** as an oil.

(b)Preparation of thioether by thia-Michael reaction

To a mixture of 0.55 g thiophenol (5 mmol) and 0.11g (10 mol %) potassium phosphate, 0.430 g (5 mmol) methyl acrylate was added. The reaction mixture was stirred till completion of the reaction. (tlc, 8-10 min). The resultant product was extracted with 3×15 cm^3 dichloromethane. The organic extract was concentrated under vacuum and the resultant residue upon filtration through a short column of silica-gel furnished 1.39 g (94%) **4a** as an oil.

Spectral data of the representative compounds

(Prop-2-ynylsulfanylmethyl) benzene, 3e (C_9H_8S): IR (Neat): 3010, 2221, 1447, 763, 699 cm^{-1}; ^1H NMR (300 MHz, $CDCl_3$): δ 2.32 (t, *J* = 2.4 Hz, 1H), 3.09 (d, *J* = 2.4 Hz, 2H), 3.89 (s, 2H), 7.24-7.36 (m, 5H); ^{13}C NMR (75 MHz, $CDCl_3$): δ 35.24 (SCH_2), 71.33 (CH), 79.86 (C), 127.21 (ArCH), 128.58 (ArCH), 129.04 (ArCH) , 137. 45 (ArC). Anal. Calcd for C_9H_8S: C 72.93, H 5.44. Found: C 72.19, H 5.12%.

2-[(4-Fluorobenzyl)sulfanyl] ethanol, 3n ($C_9H_{11}OFS$): IR (Neat): 3420, 2963, 1455, 804 cm^{-1}; ^1H NMR (300 MHz, $CDCl_3$): δ 2.43 (br s, OH, 1H), 2.60 (t, *J* = 6.0 Hz, 2H), 3.67 (t, *J* = 5.7 Hz, 2H), 3.69 (s, 2H), 6.99 (t, *J* = 8.7 Hz, 2H), 7.24-7.29 (m, 2H); ^{13}C NMR (75 MHz, $CDCl_3$): δ 34.22 (SCH_2), 35.05 (SCH_2), 60.34 (OCH_2), 115.29 (ArCH), 115.58 (ArCH), 130.32 (ArCH), 130.42 (ArCH), 133.76 (ArCH), 133.80 (ArC) , 161.91 (ArC, $^1J_{CF}$ = 22.4 Hz). Anal. Calcd for $C_9H_{11}OFS$: C 58.04, H 5.95. Found: C 57.85, H 5.47%.

Methyl 3-(cyclohexylsulfanyl) propanoate, 5am ($C_{10}H_{18}O_2S$): IR (Neat): 2930, 1741, 1436, 1244 cm^{-1}; ^1H NMR (300 MHz, $CDCl_3$): δ 1.10-1.40 (m, 5H), 1.60-162 (m, 1H), 1.71-1.77 (m, 2H), 1.91-1.98 (m, 2H), 2.58 (t,, J = 7.5 Hz, 2H), 2.59-2.69 (m, 1H), 2.79 (t, J = 7.5 Hz, 2H), 3.68 (s, 3H); ^{13}C NMR (75 MHz, $CDCl_3$): δ 24.96 (CH_2), 25.76 (CH_2), 26.04 (CH_2), 35.03 (SCH_2), 43.56 (CH_2), 51.74 (OCH_2), 172.49 (CO). Anal. Calcd for $C_{10}H_{18}O_2S$: C 59.37, H 8.97. Found: C 58.87, H 8.14%.

Methyl-3-(benzylsulfanyl)-2-methylpropanoate, 5bp ($C_{12}H_{16}O_2S$): IR (Neat): 3028, 1738, 1455, 701 cm^{-1} ^1H NMR (300 MHz, $CDCl_3$) : δ 1.21 (d, J = 6.9 Hz, 3H), 2.47 (dd, J = 12.6 & 6.3 Hz, 1H), 2.65 (sextet, J = 6.9Hz, 1H), 2.76 (dd, J = 12.6 & 7.2 Hz, 1H), 3.69 (s, 3H), 3.72 (s, 2H), 7.31-7.33 (brs, 5H); ^{13}C NMR (75 MHz, $CDCl_3$): δ 16.85 (CH_3), 34.55 (CH_2), 36.62 (SCH_2), 39.82 (CH_2), 51.79 (OCH_3), 127.06 (ArCH), 128.48 (ArCH), 128.51(ArCH), 138.13(ArC), 175.55 (CO)). Anal. Calcd for $C_{12}H_{16}O_2S$: C 64.25, H 7.19. Found: C 63.86, H 6.97%.

3-(Cyclohexylsulfanyl) propanenitrile, 5cm ($C_9H_{15}NS$): IR (Neat): 2930, 2250, 1449, 1265, 740 cm^{-1}, ^1H NMR (300 MHz, $CDCl_3$): δ 1.2-1.4 (m, 5H), 1.60-1.63 (m, 1H), 1.75-1.77 (m, 2H), 1.94-1.98 (m, 2H), 2.61 (t, J = 6.9 Hz, 2H), 2.67-2.75 (m, 1H), 2.79 (t, J = 6.9 Hz, 2H); ^{13}C NMR (75 MHz, $CDCl_3$): δ 19.26 (CH_2) , 25.58 (CH_2), 25.64 (CH_2), 25.92 (CH_2), 33.49 (SCH_2), 43.76 (CH_2), 118.45 (CN). Anal. Calcd for $C_9H_{15}NS$: C 63.85, H 8.93, N 8.27. Found: C 63.16, H 8.27, N 7.87%.

3-(Butylsulfanyl)propanamide, 5dj ($C_7H_{15}NOS$): Solid, M.P.106 ^0C; IR (KBr):ν = 3358, 3185, 1657, 1423, 682 cm^{-1}; ^1H NMR (300 MHz, $CDCl_3$): δ 0.90 (t, J = 7.2 Hz, 3H), 1.38 (sextet, J = 7.2 Hz, 2H), 1.57 (quintet, J = 7.5 Hz, 2H), 1.98 (brs, 2H), 2.49 (t, J = 7.8 Hz, 2H), 2.54 (t, J = 7.2 Hz, 2H), 2.80 (t, J = 7.2 Hz, 2H); ^{13}C NMR (75 MHz, $CDCl_3$): δ 13.66 (CH_3), 21.95 (CH_2), 27.44 (CH_2), 31.61 (CH_2), 32.03 (CH_2), 35.99 (SCH_2), 173.87 (CO). Anal. Calcd for $C_7H_{15}NOS$: C 52.14, H 9.38, N 8.69. Found: C 52.06, H 9.18, N 8.37%.

3-(Cyclohexylsulfanyl) propanamide, 5dm ($C_9H_{17}NOS$): Solid, M. P. 79 ^0C; IR (KBr): 3356, 3187, 1654, 1420, 1303, 682 cm^{-1}; ^1H NMR (300 MHz, $CDCl_3$): δ 1.21–1.31 (m, 5H), 1.5-1.6 (m, 1H), 1.73-1.74 (m, 2H), 1.92-2.0 (m, 2H), 2.47 (t, J = 7.5 Hz, 2H), 2.60-2.67 (m, 1H), 2.79 (t, J = 7.2Hz, 2H), 6.0 (brs, 2H); ^{13}C NMR (75 MHz, $CDCl_3$): δ 25.47 (CH_2), 25.73 (CH_2), 26.02 (CH_2), 33.57 (CH_2), 36.26 (SCH_2), 43.82 (CH_2), 174.21(CO). Anal. Calcd for $C_9H_{17}NOS$: C 57.71, H 9.15, N 7.48. Found: C 57.27, H 8.93, N 7.13%.

3-(Benzylsulfanyl) propanamide, 5dp ($C_{10}H_{13}NOS$): Solid, M. P. 101 ^0C; IR (KBr): ν: 3354, 3182, 1634, 1413, 702 cm^{-1}, ^1H NMR (300 MHz, $CDCl_3$): δ 2.41 (t, J = 7.2 Hz, 2H), 2.73 (t, J = 7.2 Hz, 2H), 3.75 (s, 2H), 5.72 (brs, 2H), 7.30-7.33 (m, 5H); ^{13}C NMR (75 MHz, $CDCl_3$): δ 26.95 (CH_2), 36.57 (SCH_2), 36.69 (CH_2), 127.15 (ArCH), 128.59 (ArCH),

128.84 (ArCH), 138.21(ArC), 173.59 (CO). Anal. Calcd for $C_{10}H_{13}NOS$: C 61.15, H 6.71, N 7.17. Found: C 61.03, H 6.49, N 6.87%.

Conclusions

In conclusion, we have demonstrated the usefulness of potassium phosphate as a highly efficient catalyst for the synthesis of a variety of thioethers following two different routes. The operational simplicity, substrate compatibility, chemoselectivity, very high regioselectivity, excellent yields and easy work up procedures are a few other noteworthy features of the developed protocols to have general applicability.

Acknowledgements

The authors (UVD, MAK) thank UGC, New Delhi for financial assistance and Junior Research Fellowship, respectively.

References

1 Cremlyn R J, *An Introduction to Organosulfur Chemistry* (Wiley, New York), 210 (1996).
2 Oae S, *Organic Sulfur Chemistry*, *Bio-chemical Aspects*, edited by Okuyama T (CRC Press, Boca Raton, FL) (1992).
3 McReynolds M D, Doughtery J M & Hanson P R, *Chem Rev*, 104 (2004) 2239. https://pubs.acs.org/doi/10.1021/cr020109k
4 Salvatore R N, Smith R A, Nischwitz A K & Gavin T, *Tetrahedron Lett*, 46 (2005) 8931. https://doi.org/10.1016/j.tetlet.2005.10.062
5 Shah S T A, Khan K M, Heinrich A M & Voelter W, *Tetrahedron Lett*, 43 (2002) 8281. https://doi.org/10.1016/S0040-4039(02)02028-2
6 Vijaikumar S & Pitchumani K, *J Mol Catal A Chem*, 217 (2004) 117. https://doi.org/10.1016/j.molcata.2004.03.002
7 Movassagh B & Beigi M S, *Monatsh Chem*, 140 (2009) 409. DOI: 10.1007/s00706-008-0043-0
8 Movassagh B & Shaygan P, *ARKIVOK*, VII (2006) 130. https://doi.org/10.3998/ark.5550190.0007.c15
9 Yadav J S, Reddy B V S & Baishya G, *J Org Chem*, 68 (2003) 7098. https://doi.org/10.1021/jo034335l
10 Ranu B C, Dey S S & Hajra A, *Tetrahedron*, 59 (2003) 2417. https://doi.org/10.1016/S0040-4020(03)00289-8
11 Wu J & Xia H G, *Green Chem*, 7 (2005) 708. https://doi.org/10.1039/B509288D
12 Yang M H, Yan G B & Zheng Y F, *Tetrahedron Lett*, 49 (2008) 6471. https://doi.org/10.1016/j.tetlet.2008.08.109
13 Fan R-H & Hou X-L, *J Org Chem*, 68 (2003) 726. https://doi.org/10.1021/jo025983s
14 Gao P, Xu P F & Zhai H, *Tetrahedron Lett*, 49 (2008) 6536. https://doi.org/10.1016/j.tetlet.2008.09.004
15 Karimi B & Zareyee D, *Synthesis*, 1875 (2003). DOI: 10.1055/s-2003-40981
16 Meshram H M, Ganesh Y S S, Ramesh Babu K, Eishwaraiah B & Yadav J S, *Indian J Chem*, 44B (2005) 193. http://nopr.niscair.res.in/handle/123456789/8930
17 Ranu B C & Mandal T, *Tetrahedron Lett*, 47 (2006) 6911. https://doi.org/10.1016/j.tetlet.2006.07.017
18 Zaragoza F, *Tetrahedron*, 57 (2001) 5451. https://doi.org/10.1016/S0040-4020(01)00447-1
19 Firouzabadi H, Iranpoor N & Maasoumeh J, *Tetrahedron Lett*, 47 (2006) 93. https://doi.org/10.1016/ j.tetlet.2005.10.137
20 Itoh T & Mase T, *Org Lett*, 6 (2004) 4587. https://doi.org/10.1021/ol047996t
21 Varala R, Ranu E, Alam M M & Adapa S R, *Chem Lett*, 33 (2004) 1614. https://doi.org/10.1246/cl.2004.1614
22 Thopate T S, Desai U V, Pore D M & Wadgaonkar P P, *Catal Commun*, 7 (2006) 508. https://doi.org/10.1016/j.catcom.2005.12.028
23 Mitragotri S D, Pore D M, Desai U V & Wadgaonkar P P, *Catal Commun*, 9 (2008) 1822. https://doi.org/10.1016/j.catcom.2008.02.011
24 Desai U V, Mitragotri S D, Thopate T S, Pore D M & Wadgaonkar P P, *Monatsh Chem*, 138 (2007) 759. https://doi.org/10.1007/s00706-007-0675-5
25 Pore D M, Desai U V, Thopate T S & Wadgaonkar P P, *Aust J Chem*, 60 (2007) 435. https://doi.org/10.1071/CH07097
26 Desai U V, Pore D M, Tamhankar B V, Jadhav S A & Wadgaonkar P P, *Tetrahedron Lett*, 47 (2006) 8559. https://doi.org/10.1016/j.tetlet.2006.09.138
27 Chen Z-G, Wang Y, Wei J-F, Zhao P-F & Shi X-Y, *J Org Chem*, 75 (2010) 2085. https://doi.org/10.1021/jo9026879
28 Joshi A V, Bhusare S, Baidossi M, Qafisheh N & Sasson Y, *Tetrahedron Lett*, 46 (2005) 3583. https://doi.org/10.1016/j.tetlet.2005.03.040
29 Desai U V, Pore D M, Solabannavar S B, Mane R B & Wadgaonkar P P, *Synth Commun*, 34 (2004) 25. https://doi.org/10.1081/SCC-120027234
30 Pore D M, Desai U V, Thopate T S & Wadgaonkar P P, *Russ J Org Chem*, 43 (2007) 1088. https://doi.org/10.1134/S107042800707024X
31 Desai U V, Pore D M, Mane R B, Solabannavar S B & Wadgaonkar P P, *Synth Commun*, 34 (2004) 19. https://doi.org/10.1081/SCC-120015763
32 Pore D M, Soudagar M S, Desai U V, Thopate T S & Wadagaonkar P P, *Tetrahedron Lett*, 47 (2006) 9325. https://doi.org/10.1016/j.tetlet.2006.10.114
33 Pore D M, Desai U V, Dongare B B & Undale K R, *Catal Lett*, 1 (2009) 104. https://doi.org/10.1007/s10562-009-0074-0.
34 Moghaddam F M, Bardajee G R & Veranlou R O C, *Synth Commun*, 35 (2005) 2427. DOI: 10.1080/00397910500189783
35 Sharma G, Kumar R & Chakraborti A K, *J Mol Catal A Chem*, 263 (2007) 143. https://doi.org/10.1016/j.molcata.2006.08.021
36 Ranu B C & Dey S S, *Tetrahedron*, 60 (2004) 4183. https://doi.org/10.1016/j.tet.2004.03.052
37 Moghaddam F M, Bardajee G R, Oftadeh R & Veranlou R O C, *Synth Commun*, 35 (2005) 2427. https://doi.org/10.1081/SCC-120006015
38 Khan A T, Ghosh S & Choudhury L H, *Eur J Org Chem*, 12 (2006) 2226. https://doi.org/10.1002/ejoc.200600006
39 Hussain S, Bhardwaj S K, Chaudhuri M K & Kalita H, *Eur J Org Chem*, 13 (2007) 374. https://doi.org/10.1002/ejoc.200600691
40 Chen X, She J, Shang Z, Wu J & Zhang P, *Synthesis*, 3931 (2008). DOI: 10.1055/s-0028-1083254

UGC CARE Listed
ISSN No.2394-5990

संशोधक

वर्ष : १० • मार्च २०२२ • पुरवणी विशेषांक ०५

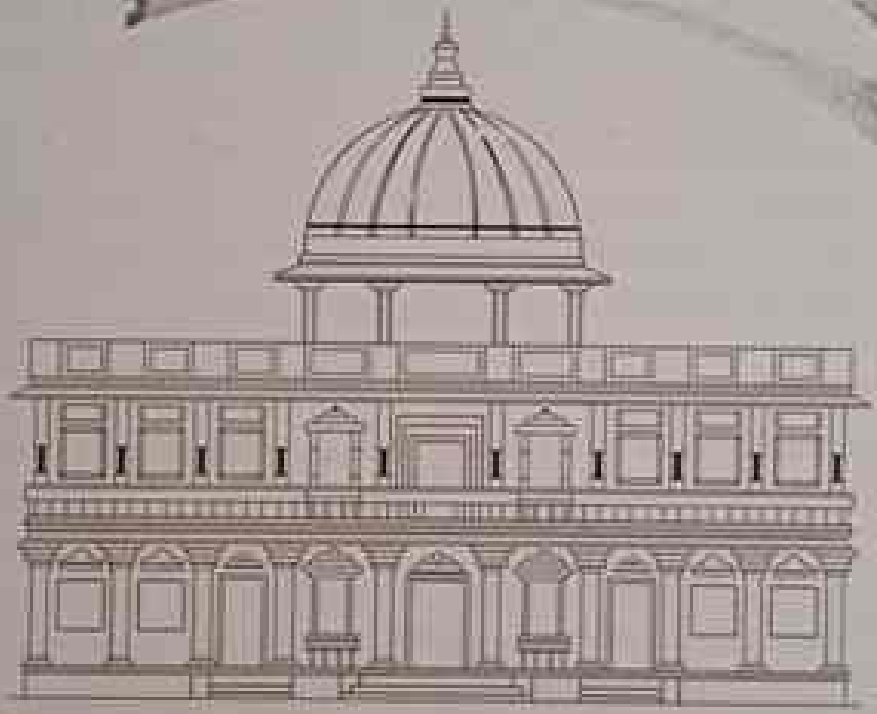

इतिहासाचार्य वि. का.राजवाडे संशोधन मंडळ, धुळे

ISSN No. 2393-1892

The Agroeconomic Thoughts Of Mahatma Jotirao Phule And Its Relevance

1) Prof. Dr. CHANDRAKANT S. CHAVAN

(M.A., B.Ed., SET., Ph.D.)

H.O.D. Dept. of History, Walchand College of Arts and Science, Solapur

Mob. No.: 9850336338 E-mail: chandrakant678@gmail.com

2) HARSHAL SHASHIKANT SHINGE

Research Scholar, PAH Solapur University, Solapur

Mob. No.: 8793347640 E-mail: harshal_shinge@yahoo.com

Abstract :

India's prevailing agricultural unrest reflected in recently organized large scale farmer protests 2020-21. The protests received negative reactions from the existing government, ruling party machinery and the mainstream media. Agriculture is becoming non remunerative day-by-day. Farmers are conducting suicide every year. The number of small and fragmented land holdings is increasing. Institutional flow of credit is not reaching the farmers. Money lenders menace continues. There is still a lack of scientific approach towards agriculture at farm as well as backward and forward linkages. Water crisis is a serious issue impeding the food security program. Markets are not farmer friendly. Policy makers and bureaucracy lack empathy towards the agrarian issues. Mahatma Phule raised these issues 140 years ago they still persistently continue to trouble India's agro-economy. In this context his thoughts remain more contemporary and relevant.

Key words :

1) Farm Bills 2) Rural distress 3) Agricultural unrest 4) Farmer suicide 5) Credit scarcity 6) Loan waiver 7) Money lenders Menace 8) fragmented land holdings 9) Land Bank 10) Pipeline Irrigation 11) Green Revolution.

Introduction :

In recent times India witnessed two significant events. First is the 'Azadi Ka Amrit Mahotsava' (Celebrating 75 years of Independence). Second was the farmers' protest against three Farm Bills, it was the longest and largest protest in post-independence history of India (Starting in Sept. 2020 & ending in Nov. 2021). The events related to the protest which have left long lasting impression were, 750 protesting farmers lost their lives, Lakhimpur Kheri violence lead to killing of four farmers, mainstream media propaganda against protest and its attempt to tarnish the image of the protestors by declaring them 'Khalistani's, 'Pro-Pakistani's, 'Anti indians'. Lastly, the state's use of brutal police force to curb down the protest. With this in the background, it is appropriate time to take a historical review of the prevailing agricultural unrest in India, from the perspective of Mahatma Phule's agro economic thoughts. Especially expressed in his famous book 'Shetkaryachha Asud' (Cultivator's whipcord) and its relevance in present times. As Agriculture sector is still the largest employer with its 50% share. Its contribution in gross value added is 18% as on 2020

The Non-Remunerative Agricultural Sector :

Since independence India has transformed itself from a food scarce and importing nation into a self-sufficient food grain producer and net exporter of agricultural products. Thanks to its robust agricultural growth since the Green Revolution program. India is one of the top producers of cereals, fruits and vegetables, milk, meat and fish. Despite these achievements, affordability to a vast majority including a large number of farmers too, remains a question mark. 1. Hunger and nutrition still remains a serious issue. Among the 107 countries India ranks 94th in the global hunger index 2020 2. One of the worst rankings in food security parameters.

About 140 years back Mahatma Phule stated, income of a farmer owning 8 oxen is lesser than that of a white sepoy.3 He further states that 25

lakhs shudra ati shudras (depressed class) became unemployed due to rural distress.4 In present times 22.50% of the farmers live below official poverty line.5 Even today due to lack of financial security many youngsters are giving up farming. There is continuity in the grim situation of farmers.

The Issue of Farmer Suicide :

Between 1995 and 2015 India recovered 2, 96, 438 farmer suicides.6 In 2019 the number was 10,281, means 28 farmers a day.7 India's richest state Maharashtra, home of India's 1st agro economist Mahatma Phule tops in farmer suicide cases for consecutively for the 12 years. The state alone has accounted for an alarming 60,750 farmer suicides since 1995 ; which can be cited as an example of disconnect between economic growth and farmers development.

Small and Fragmented Land Holding :

As per agricultural census 2015-16 about two-third of the land holdings in the country are less than one hector.8 There exists also disparity in share of different social groups in numbers of operational holdings. Scheduled Castes account for 11.84%, Scheduled Tribes, 8.65%, Institutional, 0.18%, other, 79.33%.10 which has resulted in ownership inequality impeding access to land for crops and livestock.

The Swaminathan Report 2006 (National Commission on Farmers 2004) has recommended distribution of ceiling surplus and wasteland, preventing the corporate sector from acquiring land for non-agricultural purposes. Ensure access of forests to tribal and pastorals. Mahatma Phule uses the term 'Bhauthisathe' (brotherhood's share) for fragmentation due to inheritance.11 According to Mahatma Phule due to fragmentation families are migrating in search of livelihood. They handover the land to the tenant. With increasing population the phenomenon will continue in future and will hinder application of modern machinery in farming.

To deal with the issue a legislation can be brought to restrict transfer of land through inheritance to only one sibling. The process can be voluntary at family level. On failure, government intervention in the form of confiscation of the land can be initiated. Such lands can become part of 'Land Bank' meant to distribute the land amongst meritorious landless labourers, tenants and the siblings deprived of land due to the law.

Credit Scarcity and Money lenders Menace :

According to NABARD about 52% of the agricultural households in the country were estimated to be indebted. At the all India level, about 60% of the outstanding loans were taken from institutional sources which included, Government (2.1%), Co-operative Societies (14.8%) and Banks (42.9%). The rest comes from Non-Institutional sources, of which Agricultural or professional money lenders account for highest & the rest being relatives & friends, doctors, lawyers and traders.12 Mahatma Phule suggested keeping an eye over money lenders business, because Lands kept as collateral with the money lender are seldom returned to the farmers. After cutting all paperwork charges the farmers are given left over amount as loan. There is commonality between the findings of NABARD & Mahatma Phule w.r.t. money lender menace which continues till today.

Loan Waiver a Short Term Solution :

Government intervention to lessen financial burden comes in the form of loan waiver. It benefits only 10-15% of all farmers as the rest do not have access to institutional loans.13 Only 11 states have announced such waivers. There is gap between the actual waived amount announced & actual outlay.14 Expanding the formal banking network and providing farm loans at low interest rate with in-built crop insurance can help reduce the incidence of indebtedness as well as do away with the policy of farm waivers.

Lack of Scientific Approach Towards Farming:

Punjab is already facing the issue of slower growth in the agriculture sector. Due to paddy-wheat monoculture, excessive use of chemical fertilizers & irrigation and resultant land degradation. 60% of agriculture in India is rain fed i.e. Dry land

ISSN No. 2394-7999

farming. Per unit area productivity in India is much lower than its global counterparts. 30% of Indian land is degraded or faces desertification & is responsible for 11% of total desertification. Cost of land degradation is estimated at 2.1% of India's 2014-15 G.D.P.15

Water Management :

India's population is projected to be 1.5 billion by 2030.16 water scarcity will make it difficult to achieve the goal of food security for all. Wheat and rice India's two major staple crops are already being affected by water related issues. About 74% of area under wheat and 65% of area under cultivation faces significant levels of water scarcity.17 140 years back Mahatma Phule suggested village level water mapping, water harvesting from mountain top to bottom. Awarding farmers for digging wells, dredging of river and lake silt and allowing its free distribution to farmers. The Maharashtra Government's Jalyukta Shivar Abhiyan contains all the above components. Punjab Government's 'Paani Bachao Paise Kamao' scheme too focused on water management.

All farms in the country should be provided with a pipeline irrigation system by dismantling the canal irrigation system, it will help reduce wastage and increase precision in water management. 100% subsidy can be provided to farmers for scaling up micro irrigation facilities. Managing cropping patterns according to agro climatic zones, tracking water consuming crops and developing data accordingly is necessary. Farmers can be awarded for achieving more productivity by consuming less water.

Scientific Animal Husbandry :

Mahatma Phule suggested breeding the best species of sheep and goats from all over the world to add income through wool and increase soil fertility. In dry land farming areas animal husbandry is promoted as allied activity Example 'Bandist Sheli Palan' (Enclosed Goat Breeding) scheme of the Maharashtra Government.

Poor Agricultural Marketing Infrastructure :

Mahatma Phule states that wild boars destroy crops in the field and middlemen in the mandis. After paying the market fees, transport cost, Money lenders debt for input costs, the farmer is left with nothing. Today frustrated farmers often throw their crops on the road instead of selling it at APMC markets where prices are reduced artificially. India is still struggling to integrate the Agrimarket and bring transparency in its dealings. A system where farmers, traders and consumers welfare is taken care of needs to be developed. A public private partnership in dealing with MSP, procurement of all that is grown, storage, distribution for direct consumption and food processing and marketing can help solve the issue to a large extent.

Negligence in Policy Making

India appointed the First National Commission of Agriculture in 1970, and 34 years after it, The National Commission for Farmers 2004 was appointed under the chairmanship of M.S. Swaminathan. It submitted a report in 2006. The farmer's protesting in 2020-21 are still demanding its implementation. Now the present government has appointed a committee in 2016 named Doubling farmers income committee. In its report of 2018 it has set a target of doubling the income of farmers by 2022 which is the present year. But on the field the business is as usual.

Poor track record of Extension Activities :

Mahatma Phule suggests the government conduct study tours for farmer's sons in developed country's agriculture schools to increase their knowledge. Despite a strong network of agricultural universities under ICAR, various crop specific research institutes, spread across the 15 agro climatic zones of India, extension activity remains very lethargic. There is a huge gap between research in the laboratory and its application in the fields. Example, Solapur district lies in rain shadow region, and has semi-arid steppe type climate with predominantly thorny vegetation (Koppen's climatic classification). With the construction of Ujani Dam in the 1970's things changed. Today Solapur district has the highest number of sugar factories in

Maharashtra. Thanks to increase in the area under sugarcane crop at the cost of Jowar, oilseeds and pulses, Ironically Solapur also houses one of most water intensive and polluting industries, namely Thermal power generation station, cement factories and chemical industry. This can be taken as a best example of ill-planned extension work and ill-development planning in India.

Secondary treatment to Agriculture over Corporate Sector :

Mahatma Phule suggested modernization of agriculture but in reality biased treatment exists. Out of total gross bank credit disbursed in 2017, the share of Agriculture was only 13-14%. While total credit to industry was 35%. Total credit to top 10 corporate borrowers as of March 2015 was 10-15%. The scale of corporate NPA's problem is of a higher magnitude and corporate defaults have cost the exchequer more than farm loan waivers. In the financial year 2017-18 to date 11 State governments have announced farm loan waivers, totaling 1, 84,800 cr. In contrast, the total debt of India's top 10 corporate borrowers alone was 7, 31,000 cr. (4 times) and of the top 12 NPA's 3, 45,000 cr. Data shows that the percentage of unpaved loans in agriculture has been far lower than that in the industry.18 Despite this fact wherever waiver is announced it is received negatively from media and business houses. Even the government takes such decisions very reluctantly.

Insensitive bureaucracy :

According to the Mahatma Phule Brahmin priestly class, money lenders and Brahmin Bureaucracy are the three enemies of farmers. Present bureaucracy seems to be working under caste prejudice and British hangovers. After the introduction of CSAT Exam in 2011 by UPSC more candidates from upper castes, urban background with English and technical education are entering into the country's highest bureaucratic structure.19. The government has started the practice of lateral entry. This is another setback to making India's higher bureaucracy inclusive. India needs an inclusive and unbiased bureaucracy to implement the vision of Mahatma Phule's overall development of the depressed classes, spread education for awareness and increasing rational thinking, establishing boarding schools for wards of farmers, spending of entire local funds for education & training of the farmer's ward, for government to inculcate good moral values amongst its citizens.

Conclusion :

None of Mahatma Phule's contemporaries dealt the subject with such an empathy, in-depth and scientific way.20 He was not a trained economist, but was deeply engaged and practicing agro economist. His thoughts on the subject are reflected in contemporary policies and scholarly works. In this regard Sharad Joshi rightfully calls him the "Pioneer Agro economist of India".21 Most importantly people's participation is vital for nation building. Caste and religion still play a divisive role in India. In this context Mahatma Phule's objective of establishing in India society based upon the principles of justice, liberty and equality becomes more significant and relevant in present time.

References :

1. Report of the committee on doubling farmer's income, Vol-XII, Feb, 2018, Department of Agriculture, Cooperation and farmer's welfare, Ministry of Agriculture and farmers welfare. https://www.farmer.gov.in/image default/DFI/%20Vol.12A.pdf.
2. Global Hunger Index 2020, http://www.globalhungerindex.org/india.html, 31/03/2022, 6 :00 pm
3. Kir Dhanjay, Malshe S.G., Phadke Y.D., 'Mahatma Phule Samagra Vangmay', Pg. 306-26, 2006 Maharashtra Rajya Sahitya Aani Sanskruti Mandal-Mumbai.
4. Ibid.
5. Ibid, Report of the committee on doubling farmers income.
6. P. Sainath, 2014 Article 'Have India's Farm Suicides really declined', BBC News archival https://www.bbc.co.uk/news/world-

asia-india-28205741.amp 30/3/2022, 5.36 pm.
7. Sengupta Ranjit Article, 'Everyday 28 people depending on farming die by suicide in India, https://www.downtoearth.org.in/news/agriculture/ever-day-28-people-dependent-onfarming-die-by-suicide-in-India 73194, 31/3/2022. 5.15 pm.
8. https://www.bbc.com/new/world-asia-india-28205741, 31/7/22, 5.76 pm.
9. Agri census, https://www.agrieconomics.nic.in>divisiontype.
10. Ibid.
11. Phule Mahatma 'Shetkaryancha Asud' Part 4 pg 306-36, from, 'Mahatma Phule Samagra Vangmay', 2006, Maharashtra Rajya Sahitya Aani Sanskruti Mandal, Mumbai.
12. https://www.nabard.org/news-article.aspx?id=25&Cid =552&NED=160 31/3/2020; 6:15 pm.
13. Sesadri Kumar, Article in The Wire, https://www.Thewire.in/economy/Farm-loan-waivers-and-corporate-defaulters-are-two-sides-of-the-same-coin=15 Jan 2018 31/03/20 5:30 pm.
14. Sahan Madan, Article, Nov 4, 2020, https://www.financial Express.com/opinion/the-trut-about-farm-loan-waivers/2120437/31/3/22, 8:31 pm.
15. Composite Water Management Index, NITI Aayog, In association with, Min. of Jalshakti & Min. of Rural Development', https://www.niti.gov.in/uploads/sample/water-index-report-2.pdf.
16. United Nations, 'World Urbanization Prospects 2018-Population Division', https://www.population.un.org/wup/Downkoad, 31-3-22, 7:30 pm.
17. Shashank Singh, Article, 'Hidden risks and untapped opportunities: water and the Indian Banking Sector, wwf-India, 2019, pg. 21, https://www.iwfactivironmentportal.org.in/files/pdf
18. Rohit Prasad, Gupta Gaurav Article Feb. 18 2019, https://www. businessstandard.com/article/finance/top12-corporate-npas-cost-exchequer twice-as-much-as-farm-loan-waivers-119021800080_1.html, 31/3/22, 6:30 pm
19. Aadil Raga Khan, Article Oct. 21, 2021, https://m.thewire.in/article/rights/ preference-for-english-upperccaste-candidates-how-upsc-biases-impact-civil services-exam/amp.
20. Kotapalli Nagnath's Essay 'Shetkaryancha Asud', in 'Mahatma Phule Sahitya Aani Chalval' pg. 371, 2006, Dr. Babasaheb Ambedkar, Mahatma Jotirao Phule Aani Rajarshi Shahu Charitra Sadhane Prakashan Samiti, Maharashtra Shasan, Mumbai.
21. Joshi Sharad's Article in 'Mahatma Phule: Shodhachya navya vata', pg. 165-94, 2006, Dr. Babasaheb Ambedkar, Mahatma Jotirao Phule Aani Rajarshi Shahu Charitra Sadhane Prakashan Samiti, Maharashtra Shasan, Mumbai.

Isolation and identification of potassium solubilizing bacteria and its effect on growth of *Vigna radiata*

[1]Vaishali A. Gargade, [2]Yogesh L. Bhandari, [3]Akash S. Sura, [4]Suraj S. Gund, [5]Rutuja S. Pawar

Department of Biotechnology,
Walchand College of Arts and Science,
Solapur, Maharashtra (India) – 413006

***Abstract*: Three macronutrient Nitrogen (N), Phosphorous (P) and Potassium (K) are essential for plant growth and development. Among them Potassium is having its role in transpiration, photosynthesis, respiration, transport of sugar. Potassium is required by all the plants for growth, metabolism and development. It is observed that, potassium is present in the soil in abundant amount in the form minerals (mica, feldspar) and rocks. Most of the potassium is in nonexchangeable form in nature and cannot be easily up taken by plants. The uptake of potassium by the plants can be increased by application of potassium solubilizing bacteria in the field. The potassium solubilizing bacteria converts insoluble mineral form of potash into soluble form by secretion of enzymes; acids etc. and make available for plants. Instead of using chemical fertilizers, use of potassium solubilizing bacteria is environmentally safe and eco-friendly method. The present study is based on the isolation, identification, characterization of potassium solubilizing bacteria from soil and its effect on the growth of plant (*Vigna radiata)*.**

***Keywords*: Mica, potassium solubilizing bacteria, *Vigna radiata*, pot study**

Introduction

Potassium (K) is the third most essential macronutrient among Nitrogen (N), phosphorous (P) and potassium (K) present in soil. Potassium is most abundantly absorbed cation which plays important role in the growth, metabolism and development of all crops (Archana, 2007). Potassium helps in nitrogen uptake, transpiration, protein synthesis, grain filling, increasing disease and insect resistance, sugar and starch transport, photosynthesis along with some physiological and biochemical processes. Without adequate potash, plants will grow slowly; have poorly developed roots, small seeds, weak stem and leaves etc. Potassium deficiency can be easily observed by the signs like chlorosis, yellow spots on leaves, falling of leaf prematurely etc. As potassium is a mobile nutrient its deficiency can be passed from older to the younger leaves. Soil contains abundant amount of potassium. Potassium constitutes about 2.5% of lithosphere but the actual soil concentration of this macronutrient varies widely ranging from 0.04 to 3.0% (Parmar and Sindhu, 2013). More than 98% potassium present in soil exists in the form of silicate minerals (microcline, feldspar, muscovite, mica etc. (Buchholz and Brown, 1993). The soil minerals contain 90 to 98% of soil potassium which is in unavailable form and only 2% is in available form to plants (Archana, 2007). For providing potassium, farmers knowingly or unknowingly applying chemical fertilizers like potassium chloride, potassium nitrate, potassium sulphate, monopotassium phosphate etc. The heavy application of chemical fertilizers can cause environmental pollution. All rest amount is bound with minerals and are unavailable for uptake by plants.

Soil microbes have reported to play a key role in the natural (K) cycle and therefore, Potassium solubilizing bacteria present in soil could provide an alternating technology to make potash available to the plants by converting insoluble minerals of potassium to soluble form which can be easily up taken by plants (Parmar and Sindhu,2013). Potassium solubilizing bacteria are able to solubilize rock potassium mineral powder such as mica, feldspar and orthoclases by weathering and solubilizing. They are readily weathered through organic acids and acidic polysaccharides secreted by microorganisms.Organic acids can directly enhance dissolution of potassium minerals (Sugumaran and Janarthanam, 2007). Though several laboratory techniques states that bacteria produces acids, alkalis, acidic polysaccharides etc. the actual mechanism of potassium released from the minerals still not known (Groudev, 1987). Growth and yield of plant can be enhanced by inoculating potassium solubilising bacteria which secrets enzymes, acids etc. and make available for uptake in plants. It will reduces use of chemical fertilizers and become eco-friendly method.

Materials and methods

Collection of soil sample for isolation of potassium solubilizing bacteria

The soil sample was collected from rhizosphere of sugarcane field, located in Solapur district. The latitude of Solapur, Maharashtra is 17.6599 and longitude is 75.90638.

Culture medium used for isolation of potassium solubilizing bacteria

The modified sterile Aleksandrove's media containing 1% glucose, 0.5% peptone, 0.05% $MgSO_4.7H_2O$, 0.01% $CaCO_3$, 0.2% $CaPO_4$, 0.3% mica, 0.0005% $FeCl_3$, 2% agar, pH 6.5 was used for isolation of potassium solubilizing bacteria from soil. (Sugumaran and Janartham, 2007)

Isolation of potassium solubilizing bacteria

One gram of soil was serially diluted from 10^{-1} to 10^{-5} by using sterile distilled water. 0.1ml of sample from each test tube was spread inoculated on the sterile Aleksandrove's media containing mica as a mineral source and incubated for one week at 37℃. The well isolated seven bacterial colonies were selected for screening of its potassium solubilizing activity.

Screening of potassium solubilizing bacteria

Screening of potassium solubilizing bacteria were carried out on the basis of zone activity by using Aleksandrove's media containing phenol red as a indicator as per Khandeparkar's selection ratio (Prajapati and Modi, 2012).
Ratio= Diameter of zone of clearance/diameter of growth
The seven isolated bacterial colonies were labelled as KSB1 to KSB7. Among them the colony labelled as KSB2 was showed maximum zone activity on Aleksandrove's medium. Hence KSB2 was subjected for its further study.

Morphological characteristics of KSB2

The potassium solubilizing bacteria were grown on Aleksandrove's media to study colony characteristics (Parmar and Sindhu, 2013).Gram staining was performed. Motility was studied by hanging drop technique.

Biochemical characteristics of KSB2

The biochemical characteristics of isolated potassium solubilizing bacteria (KSB 2) were studied. Indol, methyl red, Voges Proskaur, citrate utilization test, urease test, gelatin hydrolysis test, H_2S production test, nitrate reductase test, starch hydrolysis test,oxidase test, growth in KCN and phenylalanine deaminase test were performed.
The ability of bacteria to utilize sugars (glucose, dextrose, sucrose, fructose, maltose, mannitol, lactose, mannose) (Aneja, 2002; Deshmukh, 2007) was checked by performing sugar utilization test. The isolated bacterial culture was identified by using Vitek 2 software (www.biomerieux-diagnostics.com/vitekr-2compact-0).

Physiological characteristics of KSB2

For study of physiological characteristics of KSB2, cell density was adjusted to 10^6 to 10^8 CFU/ml on the basis when culture reaches 0.1 optical units at 600 nm with colorimeter (Schaad, 1992). Further optimization of pH, temperature, carbon and nitrogen sources for maximum growth of KSB2 was done. (Prasad, 2014)

Optimization of pH

50 ml of sterile modified Aleksandrove's broth was prepared in 7 different 250 ml capacity conical flask. pH of broth in each conical flask was adjusted to 4, 5, 6, 7, 8, 9, 10. Then 0.1 ml of KSB2 culture was inoculated into respective conical flask and incubated at 37º C for 4 days on rotary shaker at 120 rpm. The optical density was measured aseptically after each 24 hrs by using colorimeter at 600 nm. (Prasad, 2014)

Optimization of temperature

50ml of sterile modified Aleksandrove's broth was prepared in 5 different 250 ml capacity conical flask. Then 0.1 ml of KSB2 culture was inoculated into respective conical flask and incubated for 4 days at 10º C, 20º C, 30º C, 40º C and 50º C on incubator shaker at 120 rpm. The optical density was measured aseptically after each 24 hrs by using colorimeter at 600 nm. (Prasad, 2014).

Optimization of carbon source

Except the carbon source in Aleksandrove's broth, sterile 50 ml of modified Aleksandrove's broth was prepared with 0.5% respective carbon source viz. glucose, dextrose, sucrose, lactose, cellulose in 5 different 250 ml capacity conical flask. Then 0.1 ml of KSB2 culture was inoculated into respective conical flask and incubated at 37° C for 4 days on incubator shaker at 120 rpm. The optical density was measured aseptically after each 24 hrs by using colorimeter at 600 nm. (Prasad, 2014).

Optimization of nitrogen source

Except the nitrogen source in Aleksandrove's broth, sterile 50 ml of modified Aleksandrove's broth was prepared with 0.5% respective nitrogen source viz. peptone, Di-ammoniun hydrogen phosphate, sodium nitrate, urea and ammonium chloride in 5 different 250 ml capacity conical flask. Then 0.1 ml of KSB2 culture was inoculated into respective conical flask and incubated at 37° C for 4 days on incubator shaker at 120 rpm. The optical density was measured aseptically after each 24 hrs by using colorimeter at 600 nm. (Prasad, 2014).

Pot study

The pot experiment was carried to observe the effect of potassium solubilising bacteria (KSB2) on the growth of *Vigna radiata*. The soil was collected from non-fertilized field site in Solapur, Maharashtra, India. Available potassium was determined by flame photometer for control pot and test pots (Olsen *et al*, 1954).
Three earthen pots were filled with soil and twenty seeds of *Vigna radiata* were sowed into each pot. The germinated plants were maintained in each pot for further study. The isolated KSB2 was inoculated into all three pots. 50 ml of inoculum containing 10^6-10^8 CFU/ml cells were mixed into sterile water and added into each pot. The control pots were inoculated with water only. After 20 days of incubation, total number of leaves, root length, shoot length, total height, number of lateral roots, dry weight and wet weight of *Vigna radiata* were measured (Sugumaran and Janarthanam, 2007).

Determination of potassium content in soil

Soil analysis was carried out by using flame photometer to determine available potassium in control soil and inoculated soil with KSB2.The 5 gm of air dried each soil sample were mixed with 25 ml 0.5 M ammonium acetate solution separately and shaked for 30 minutes. Both the solutions were filtered through Whatmann No. 1 filter paper. The filtrate was subjected to determine potassium content in soil by using flamephotometer (Knudsen *et al*, 1982).

Results and Discussion

Isolation and screening of KSB

The well isolated seven bacterial colonies (labelled as KSB1, KSB2, KSB3, KSB4, KSB5, KSB6, KSB7) from modified Aleksandrove's media were checked for its capability to solubilize potassium mineral. It was determined on the basis of

Khandeparkar selection ratio. Out of seven KSB isolates, KSB2 showed maximum zone of clearance than 6 isolated KSB cultures. (Fig 1)

Fig. 1:KSB2 grown on modified Aleksandrove's media

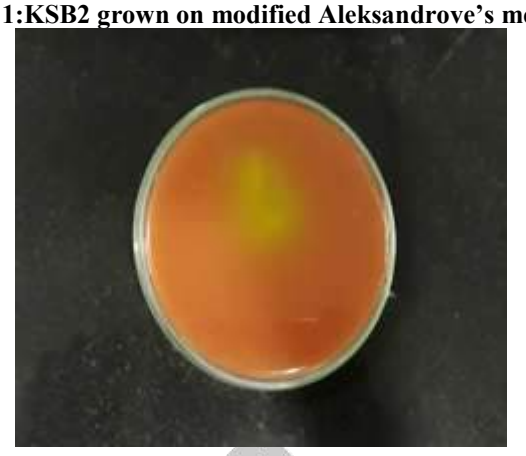

Morphological characteristics of KSB2

The colony of KSB2 was 2mm in size, circular, moist, opaque and white with entire margin. The bacteria were observed as Gram negative, rod shaped, motile (Table 1).

Table 1: Morphological characteristics of KSB2

Size	Shape	Margin	Elevation	Consistency	Opacity	Colour	Cell shape	Gram nature
2 mm	circular	entire	elevated	moist	opaque	white	rod	Gram negative

Biochemical characteristics of KSB2

The KSB2 isolate showed positive results for Voges-Proskaur test, citrate utilization, urease test, nitrate reductase, starch hydrolysis, growth in KCN. The negative results were observed for Indol test, methyl red test, gelatin hydrolysis, H_2S production, phenylalanine deaminase. The KSB2 isolate can utilize glucose, dextrose, sucrose, maltose, mannose, lactose sugar and produces acid and gas while KSB2 unable to utilize fructose (Table2). Results of biochemical characters of KSB2 were compared with Bergeys Manual of Systematic Bacteriology.(Don J. Brenner etal,2005) The isolated bacterial culture (KSB2) was identified by using Vitek2 software and identified as *Enterobacter cloacae* (www.biomerieux-diagnostics.com/vitekr-2compact-0).

Table 2: Biochemical characteristics of KSB2

Sr. No.	Biochemical test	Result
1	Indol	-
2	Methyl red	-
3	Voges-Proskaur	+
4	Citrate	+
5	Urease test	+
6	Gelatin hydrolysis	-
7	H_2S production	-
8	Nitrate reductase	+
9	Starch hydrolysis	+
10	Phenylalanine deaminase	-
11	Oxidase	-
12	Growth on KCN	+
13	Glucose	+
14	Dextrose	+
15	Sucrose	+
16	Fructose	-
17	Maltose	-
18	Mannose	+
19	Lactose	+

+ : positive − : negative

Optimization of temperature and incubation time

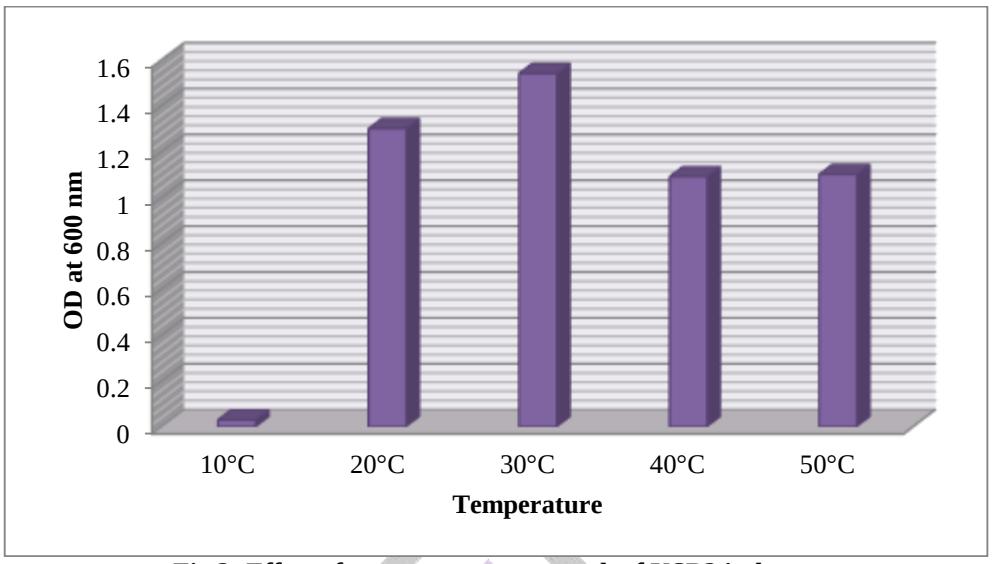

Fig 2: Effect of temperature on growth of KSB2 isolate

The maximum growth of KSB2 isolate was observed at 30 °C followed by 20 °C (Fig 2).

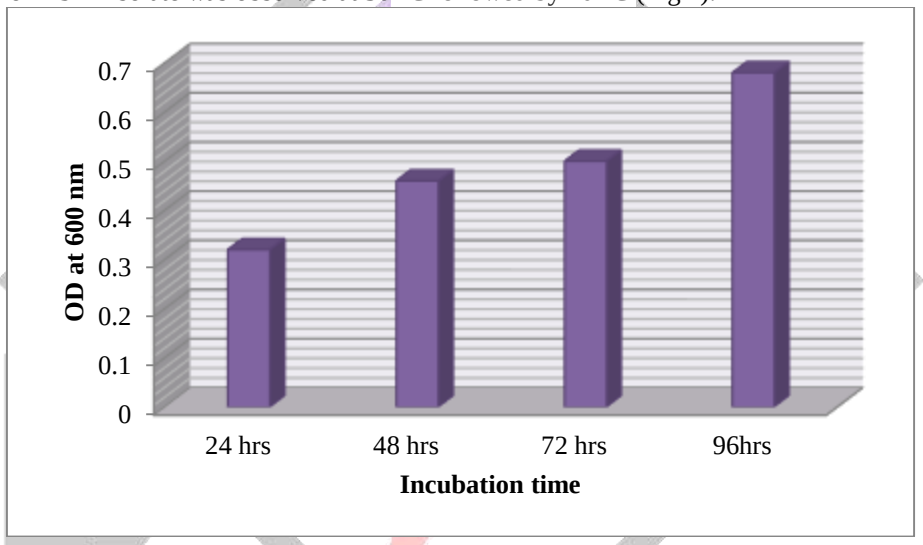

Fig 3: Effect of incubation time on growth of KSB2 isolate

The maximum growth of KSB2 isolate was observed after incubation of 96 hrs followed by 72 hrs (Fig 3).

Optimization of pH

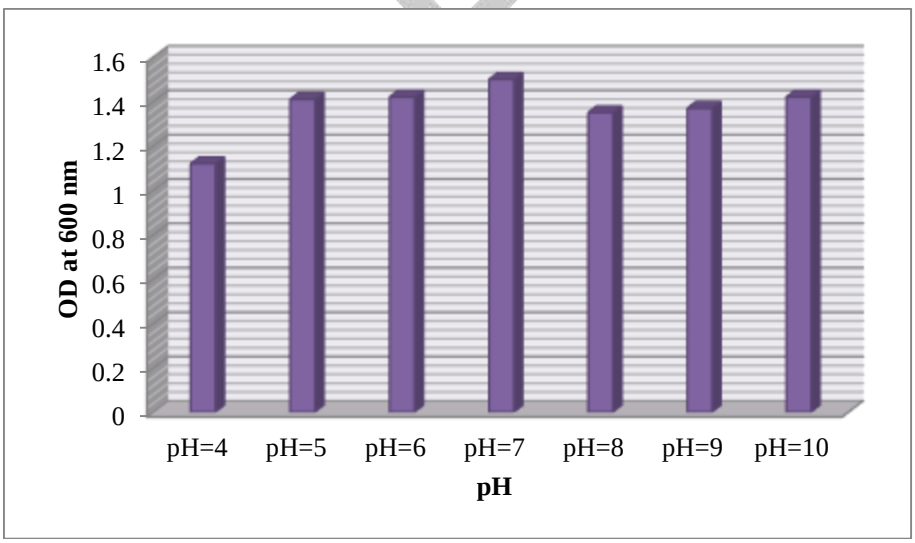

Fig 4: Effect of pH on growth of KSB2 isolate

The highest growth of KSB2 isolate was observed at pH 7 followed 5 and 6 (Fig 4).

Optimization of carbon source

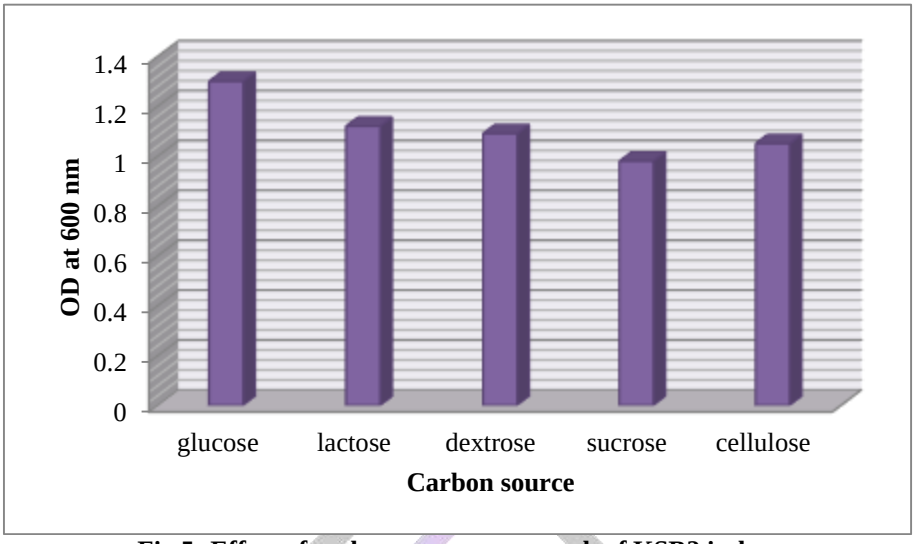

Fig 5: Effect of carbon source on growth of KSB2 isolate

Carbon is major source of energy and nutrition for the activities and growth of microorganisms. The KSB2 isolate having ability to utilize glucose followed by lactose and dextrose as a carbon source followed by cellulose and sucrose (Fig 5).

Optimization of nitrogen source

Ammonium chloride, Di-Ammonium hydrogen phosphate, sodium nitrate, peptone and urea were used for optimization of nitrogen source. The bacterial isolate (KSB2) showed maximum growth with peptone followed by Di-Ammonium hydrogen phosphate and sodium nitrate, moderate growth for ammonium chloride and low growth for urea (Fig 6).

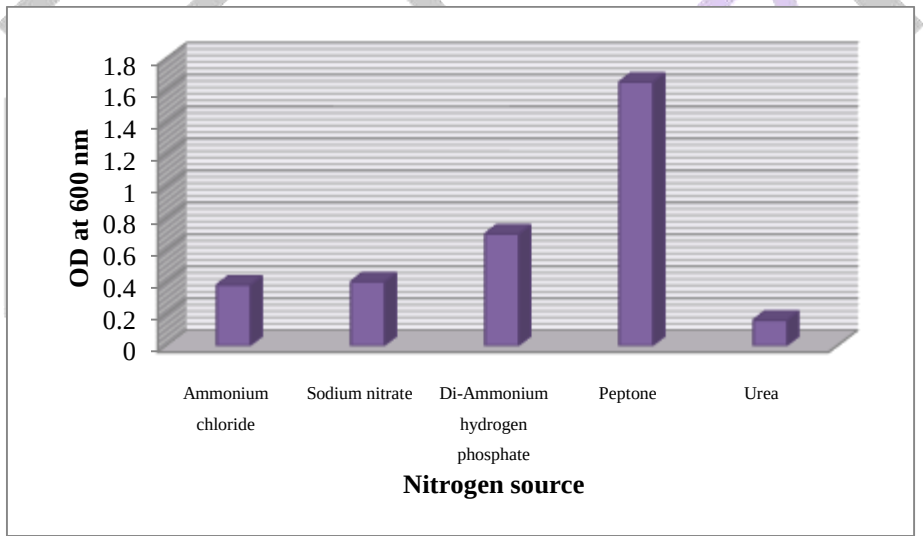

Fig 6: Effect of nitrogen source on KSB2 isolate

Pot experiment

The inoculation of KSB2 into soil sowed with plant *Vigna radiata* had significant influence on different growth characters. The total germinated seeds, average root length, average shoot length, average number of leaves, average lateral roots, average wet weight and dry weight of plants were considerably higher in plants treated with KSB2 and comparatively lower in uninoculated plants (Table 3).

Table 3: Effect of KSB2 isolate on germination and growth of *Vigna radiata*

Sr. No.	Particular	Control	Plant treated with KSB2
1	Total germinated seeds	12.00	16.00
2	Average root length (cm)	1.35	15.26
3	Average shoot length (cm)	11.09	18.84
4	Average of total number of leaves	16.00	25.00
5	Average of lateral roots	7.80	13.50
6	Average of wet weight (gm)	0.75	1.21
7	Average of dry weight (gm)	0.13	0.39

Determination of potassium content in soil

The control pot showed 38 ppm of potassium content in soil while KSB2 treated soil showed 56 ppm potassium content. It was determined by flame photometer. (Table 4)

Table 4: Determination of potassium content in soil

Soil sample	Potassium
Control (without KSB2)	38 ppm
KSB2 inoculated	56 ppm

Discussion

In present study KSB2 isolate grown on Aleksandrove's medium showed maximum zone of clearance around the colony. The KSB2 isolate was identified as *Enterobacter cloacae* on the basis of its morphological, cultural, physiological, biochemical characteristics and identified by using Vitek-2 software. The isolated KSB2 was grown at different temperature, pH, carbon and nitrogen sources for optimization of its growth parameters. It was found that KSB2 showed maximum growth at 30°C, pH 7, glucose as carbon source and peptone as nitrogen source.

As reported by various researchers, inoculation with potassium solubilizing bacteria has beneficial effects on growth of cotton and rape (Sheng, 2005), eggplant (Han and Lee, 2005), pepper and cucumber (Han and Lee, 2006; Sangeeth *et al.*, 2012), peanut (Youssef *et al.*, 2010), maize (Abou-el-Seoud and Abdel-Megeed, 2012; Leaungvutiviroj *et al.*,2010; Singh *et al.*, 2010), sorghum (Badr *et al.*, 2006), wheat (Sheng and He, 2006), Sudan grass (Basak and Biswas, 2012; Basak and Biswas, 2010), tea (Bagyalakshmi *et al.*, 2012), Okra (Prajapati *et al.*, 2013), potato (Abdel-Salam and Shams, 2012), and tomato (Lynn *et al.*, 2013). On the basis of previous findings it was concluded that KSB can used as bio-fertilizers for agriculture improvement which reduce the use of agrochemicals and support eco-friendly crop production (Archana *et al.*, 2013; Archana *et al.*, 2012; Prajapati *et al.*, 2013). Results of present study clearly indicated that the isolated *Enterobacter cloacae* have ability to solubilize potassium from its insoluble form and enhance the growth of *Vigna radiata*. Genetic modification can be possible to decrease pathogenicity of *Enterobacter cloacae* was reported by Andreote *et al.*, 2004. Therefore, it was concluded that *Enterobacter cloacae* isolate may be a potential candidate to be used as potassium solubilising bacteria by eco-friendly way.

- **References:**

Abdel-Salam M. A. and Shams A. S., 2012. Feldspar-K fertilization of potato (*Solanum tuberosum* L.) augmented by biofertilizer. *Journal of Agriculture and Environmental Sciences*. (12): 694-699.

Abou-el-Seoud I. and Abdel-Megeed A., 2012. Impact of rock materials and biofertilizations on P and K availability for maize (*Zea Maize*) under calcareous soil conditions. *Saudi Journal of Biological Sciences*. (19): 55-63.

Andreote F. D., Gullo M. J., de Souza Lima A. O., Júnior W. M., Azevedo J. L., Araújo W. L., 2004. Impact of genetically modified *Enterobacter cloacae* on indigenous endophytic community of citrus sinensis seedlings. *The Journal of Microbiology*. 42(3): 169-173.

Aneja K. R., 2002. Experiments in Microbiology, Plant pathology, Tissue culture and Mushroom production technology. Published by New Age International (P) Ltd., New Delhi, India.

Archana D. S., 2007. Studies on potassium solubilizing bacteria, Thesis submitted University of Agricultural Sciences, Dharwad, Karnataka, India.

Archana D. S., Nandish M. S., Savalagi V. P., Alagawadi A. R., 2012. Screening of potassium solubilizing bacteria (KSB) for plant growth promotional activity. *BIOINFOLET - A Quarterly Journal of Life Sciences*. (9): 627-630.

Archana D., Nandish M., Savalagi V., Alagawadi A., 2013. Characterization of potassium solubilizing bacteria (KSB) from rhizosphere soil. *BIOINFOLET - A Quarterly Journal of Life Sciences*. (10): 248-257.

Badr M. A., Shafei, A. M., Sharaf El-Deen, S.H. 2006. The dissolution of K and P-bearing minerals by silicate dissolving bacteria and their effect on sorghum growth. *Research Journal of Agricultural and Biological Science*. (2): 5-11.

Bagyalakshmi B., Ponmurugan P., Balamurugan A., 2012. Impact of different temperature, carbon and nitrogen sources on solubilization efficiency of native potassium solubilizing bacteria from tea (*Camellia sinensis*). *Journal of Biological Research*. (3): 36-42.

Basak B. B. and Biswas D. R., 2010. Co-inoculation of potassium solubilizing and nitrogen fixing bacteria on solubilization of waste mica and their effect on growth promotion and nutrient acquisition by a forage crop. *Biology and Fertility of Soils.* (46): 641-648.

Basak B. B. and Biswas D., 2012. Modification of waste mica for alternative source of potassium: evaluation of potassium release in soil from waste mica treated with potassium solubilizing bacteria (KSB). *Lap lambert Academic Publishing*.

Buchholz D. D. and Brown J. R., 1993. Potassium in missouri soils. University of Missouri Extension, Agricultural publication, pp. 22-26

Deshmukh A. M., 2007. Handbook of Media, Stain and Reagent in Microbiology. Published by Oxford Book Company.

Don J.Brenner,Noel R.Krieg, James T Staley 2005.Bergeys Manual of Systematic Bacteriology. Second edition, Vol. 2.The Proteobacteria Part B:The Gammaproteobacteria. Springer publication

Groudev S. N., 1987. Use of heterotrophic microorganisms in mineral biotechnology. *Acta Biotechnology*. (7): 299-306.

Han H. S. and Lee K. D., 2005. Phosphate and potassium solubilizing bacteria effect on mineral uptake, soil availability and growth of eggplant. *Research Journal of Agriculture and Biological Sciences*. (1): 176-180.

Han H. S. and Lee K. D., 2006. Effect of co-inoculation with phosphate and potassium solubilizing bacteria on mineral uptake and growth of pepper and cucumber. *Plant soil and environment*. 52 (3): 130-136.

Knudsen D., Peterson G. A., Pratt P. F., 1982. Lithium, sodium and potassium. In: A. L. Page, *et al* (Ed.). Methods of soil analysis Part 2. Chemical and microbiological properties. Agronomy Monograph 9. (2nd Edn). ASA and SSSA, Madison WI. pp. 225- 246.

Leaungvutiviroj C., Ruangphisarn P., Hansanimitkul P., Shinkawa H., Sasaki K., 2010. Development of a new biofertilizer with a high capacity for N_2 fixation, phosphate and potassium solubilization and auxin production. *Bioscience, Biotechnology and Biochemistry journal.* (74): 1098-1101.

Lynn T. M., Win H. S., Kyaw E. P., Latt Z. K., Yu S. S., 2013. Characterization of phosphate solubilizing and potassium decomposing strains and study on their effects on tomato cultivation. *International Journal of Innovation and Applied Studies*. (3): 959-966.

Olsen S. R., Cole C. V., Watanabe F. S., Dean L. A., 1954. "Estimation of available phosphorus in soils by extraction with sodium bicarbonate," United States Department of Agriculture, Circular No. 939.

Parmar P. and Sindhu S. S., 2013. Potassium solubilization by rhizosphere bacteria: Influence of nutritional and environmental condition. *Journal of Microbiology Research*, 3 (1): 25-31.

Prajapati K. B and Modi H. A., 2012. Isolation and characterization of potassium solubilizing bacteria from ceramic industry soil. *CIBTech Journal Microbiology*. 1(2-3): 8-14.

Prajapati K., Sharma M. C., Modi H. A., 2013. Growth promoting effect of potassium solubilizing microorganisms on okra (Abelmoscus Esculantus). *International Journal of Agricultural Science and Research*. (1): 181-188.

Prasad M. P., 2014. Optimization of fermentation of phosphate solubilising bacteria- a potential biofertilizer. *Merit Research Journal of Microbiology and Biological Sciences*. 2 (2): 31-35.

Sangeeth K. P., Bhai R. S., Srinivasan V., 2012. *Paenibacillus glucanolyticus*, a promising potassium solubilizing bacterium isolated from black pepper (*Piper nigrum* L.) rhizosphere. *Journal of Spices and Aromatic Crops*. 21 (2): 118–124.

Schaad N.W., 1992. Laboratory guide for identification of plant pathogenic bacteria, new publishing house, New Delhi, India: 81-94.

Sheng X. F and He L. Y., 2006. Solubilisation of potassium-bearing minerals by a wild-type strain of *Bacillus edaphicus* and its mutants and increased potassium uptake by wheat. *Canadian Journal of Microbiology*. (52): 66-72.

Sheng X., 2005. Growth promotion and increased potassium uptake of cotton and rape by a potassium releasing strain of *Bacillus edaphicus*. *Soil Biology & Biochemistry*. (37): 1918-1922.

Singh G., Biswas D. R., Marwaha T. S., 2010. Mobilization of potassium from waste mica by plant growth promoting rhizobacteria and its assimilation by maize (*Zea mays*) and wheat (*Triticum aestivum* L.): a hydroponics study under phytotron growth chamber. *Journal of Plant Nutrition*. (33): 1236-1251.

Sugumaran P. and Janarthanam B., 2007. Solubilization of potassium containing minerals by bacteria and their effect on plant growth. *World Journal of Agricultural Sciences.* 3(3): 350-355.

Vitek-2 software reference, (www.biomerieux-diagnostics.com/vitekr-2compact-0).

Youssef G. H., Seddik W. M. A., Osman M. A., 2010. Efficiency of natural minerals in presence of different nitrogen forms and potassium dissolving bacteria on peanut and sesame yields. *Journal of American Science*. (6): 647-660.